

Bidimensional Exploration of the warm-Temperature Ionised gas (BETIS)

II. Revisiting the ionisation mechanism of the extraplanar diffuse ionised gas

R. González-Díaz^{1,2,3} , F. F. Rosales-Ortega² , and L. Galbany^{1,3} 

¹ Institute of Space Sciences (ICE-CSIC), Campus UAB, Carrer de Can Magrans, s/n, E-08193 Barcelona, Spain.
e-mail: Raul.GonzalezD@autonoma.cat

² Instituto Nacional de Astrofísica, Óptica y Electrónica (INAOE-CONAHCyT), Luis E. Erro 1, 72840 Tonantzintla, Puebla, México.

³ Institut d'Estudis Espacials de Catalunya (IEEC), 08860 Castelldefels, Barcelona, Spain.

Received ... ; accepted ...

ABSTRACT

The extraplanar diffuse ionised gas (eDIG) is a key component for understanding the feedback processes that connect galactic discs and their halos. In this paper, we present the second study of the Bidimensional Exploration of the warm-Temperature Ionised Gas (BETIS) project, which aims to explore the possible ionisation mechanisms and characteristics of the eDIG. We use a sample of eight edge-on galaxies observed with the Multi-Unit Spectroscopic Explorer (MUSE) integral field spectrograph (IFS) and apply the methodology for obtaining binned emission line maps developed in the first paper of the BETIS project. We found that the vertical and radial profiles of the [N II]/H α , [S II]/H α , [O III]/H β , and [O I]/H α ratios depict a complex ionisation structure within galactic halos, influenced by the spatial distribution of H II regions across the galactic plane as observed from our line of sight, with Lyman continuum photon leakage from OB associations constituting the main ionisation source. Moreover, the electron temperature and S⁺/S ionisation ratio also exhibit dependency on the distribution of H II regions within the galactic discs. Our analysis excludes low-mass, hot, and evolved stars (HOLMES) as viable candidates for secondary ionisation sources to elucidate the unusual behaviour of the line ratios at greater distances from the galactic midplane. In contrast, we ascertain that shocks induced in the interstellar medium by star formation (SF) related feedback mechanisms represent a promising secondary ionisation source of the eDIG. We present a suite of models integrating ionisation mechanisms arising from fast shocks and photoionisation associated with star formation. When applied to the classical Baldwin-Phillips-Terlevich (BPT) diagrams, these models reveal that the ionisation budget of the eDIG ranges from 20% to 50% across our sample, with local variations of up to 20% within individual galaxy halos. This contribution correlates with the presence of filaments and other structural components observed within galaxy halos. The presence of shocks is additionally supported by the observation of high-density, high [O I]/H α ratios, characteristic of shock-compressed ionised gas, likely induced by feedback from regions of intense SF within the galactic disk. These results demonstrate consistency across all galaxies analysed in this sample.

Key words. galaxies: ISM – galaxies: star formation – H II regions – ISM: structure – ISM: general

1. Introduction

To understand the physical mechanisms involved in feedback processes and the baryon cycle, which are fundamental to galaxy evolution it is essential to study the different gas phases present in the interstellar medium (ISM, Ceverino & Klypin 2008, 2009; Hopkins et al. 2014; Klessen & Glover 2016; Gatto et al. 2017; Grisdale 2017; Barnes et al. 2023). One of these gas phases is known as warm ionised medium (WIM, in the context of the Milky Way) or diffuse ionised gas (DIG, for extragalactic sources; Hoyle & Ellis 1963; Hewish et al. 1968; Reynolds 1971; Reynolds et al. 1973; Guélin 1974; Reynolds 1985, 1989; Kenicutt et al. 1989; Ferguson et al. 1996). In the Milky Way, this gas was found to be warm ($0.6 - 1 \cdot 10^4$ K) and with low density ($\sim 10^{-1} \text{cm}^{-3}$), representing one of the most prominent components of the ISM, constituting the 20% of the ISM in volume and the 90% of the ionising hydrogen in mass (Greenawalt et al. 1997; Wang et al. 1997; Zurita et al. 2000; Otte et al. 2001; Finkbeiner 2003; Hoopes & Walterbos 2003; Haffner et al. 2009a). However, the DIG is typically defined by its optical emission characteristics rather than its thermodynamics (e.g. see

Haffner et al. 2009b or Dirks et al. 2023). In particular, the DIG component in extragalactic halos, also known as extraplanar diffuse ionised gas (eDIG), plays a crucial role in the physical processes driving the exchange of gas, metals, and energy between the galactic disk and halo, influencing the evolution of disk galaxies (Tenorio-Tagle & Bodenheimer 1988; Rand et al. 1990; Dettmar 1990; Miller & Veilleux 2003). Studies of the eDIG through imaging encompass explorations using different wavelengths (Sardaneta et al. 2024). In the optical range, the first detections of a diffuse component in the halo were made using H α images (Dettmar 1990; Rand et al. 1990; Pildis et al. 1994; Rand 1997, 2000; Tacchella et al. 2022). These studies found that in a wide sample of star-forming galaxies the eDIG H α emission in the halo correlates with the star formation rate (Rossa & Dettmar 2003a,b; Jo et al. 2018; Lu et al. 2023). Additionally, sub-arcsecond resolution H α imaging studies of individual galaxies (Howk & Savage 2000; Rossa et al. 2004, 2005) reveal that the eDIG exhibit complex morphological structures such as filaments, superbubbles or chimneys (also detected in X-rays and radio-emission; Tüllmann et al. 2000, 2006). Alternatively, long-slit spectroscopy studies (in combination with photo-

metric data) have enabled kinematic analyses and investigations into the potential ionisation mechanisms of the eDIG. The behaviour of the main ionisation species reveals that the $[\text{N II}]/\text{H}\alpha$, $[\text{S II}]/\text{H}\alpha$, $[\text{O III}]/\text{H}\beta$ and $[\text{O I}]/\text{H}\alpha$ ratios tends to increase as a function of the distance from the midplane (Rand et al. 1990; Dettmar 1998; Rand 1998, 2000; Collins & Rand 2001). Additionally, this higher degree of ionisation of the collisional lines usually implies higher electron temperatures in the eDIG compared to the H II regions (Haffner et al. 1999, 2009b; Boettcher et al. 2019). To explain these features and the increase in the emission of high ionisation species, several additional heating sources have been proposed (Haffner et al. 2009b and references therein). To infer the possible physical processes and the roles played by different morphological structures in the halo leading to the eDIG, the simultaneous spatial and spectral information provided by integral field spectrographs (IFS) has resulted in significant progress in this area. One of these studies, carried by the Sydney-AAO Multi-object Integral field spectrograph (SAMI; Croom et al. 2012; Bryant et al. 2015), used a sample of 40 low resolution edge-on galaxies ($0.8 \text{ kpc} < 2.8 \text{ kpc}$) to perform a systematical exploration of the eDIG (Ho et al. 2016) noticing that the disc-halo interaction can influence the eDIG emission through starburst-driven winds. On the other hand, studies with the Mapping Nearby Galaxies at Apache Point (MaNGA; Bundy et al. 2015) IFS using also low resolution large samples found an increment of the $[\text{N II}]/\text{H}\alpha$ indicating a temperature gradient in the halo, as well as a flattening in the $\text{H}\alpha$ surface brightness ($\Sigma_{\text{H}\alpha}$) comparable with the $[\text{O II}]$ emission at higher distances ($\sim 6 \text{ kpc}$).

The most recent studies with the Calar Alto Legacy Integral Field Area Survey (CALIFA; Sánchez et al. 2012, 2016) studied the eDIG kinematically using a sample of 25 galaxies with spatial resolution of 0.8 kpc on average (Levy et al. 2019), finding a "lag" in the rotation velocity of the ionised gas, i.e., a decrement of the radial velocity with the increasing of the distance from the midplane (also reported by other authors, e.g., Rand 2000; Miller & Veilleux 2003; Bizyaev et al. 2017). Nevertheless, they did not find correlations between the radial variation of the lag and the origin of the extraplanar gas. However, performing diagnoses of the main line ratios, they identified the primary ionisation sources of the eDIG the leaking of Lyman continuum (Lyc) photons from the OB stars of the H II regions, with a low contribution of an additional source in the form of hot low mass evolved stars (HOLMES; Flores-Fajardo et al. 2011; Rautio et al. 2022).

In the mentioned studies, despite the wide variety of large samples used, the spatial resolution of the data is typically insufficient to perform a comprehensive and in-depth bidimensional study of the eDIG. However, the most recent studies with IFS includes datasets of the Multi Unit Spectroscopic Explorer (MUSE, Bacon et al. 2010), whose datasets exhibits spatial resolutions lower than 200 pc , enabling a more complete exploration of the line emission, structure and kinematics of the ionised gas in the halo of edge-on galaxies. For example, Rautio et al. (2022) and Dirks et al. (2023) used a sample of nearby edge-on galaxies from Comerón et al. (2019, Com19 henceforth). The resolution and data quality of this dataset (detailed in section 2) enabled these authors to find that the $\text{H}\alpha$ emission in the halo correlates with the star formation of the galaxy, revealing the possible existence of a feedback mechanism between the plane and the halo that ionised the latter.

To advance the characterisation and exploration of the ionisation of extraplanar gas, it is crucial to study the impact of the various structures found in the halos of individual galaxies, such

as filaments, plumes or bubbles. Previous studies using IFS have presented large samples of low-resolution galaxies, with the exception of those conducted with the MUSE instrument, but focusing only on one galaxy or without inquiring in the connection between disc and halo that originates these structures and changes the ionisation conditions.

In this paper we present the second study of the Bidimensional Exploration of the warm-Temperature Ionised gas (BETIS) project, focused in the characterisation of the eDIG and the exploration of its possible ionisation mechanisms for a sample of edge-on galaxies. The paper is structured as follows. Section 2 presents and characterises the sample of edge-on galaxies, as well as describes the procedure followed for adaptive binning and the extraction of emission line features, based on the methodology developed in the first part of the series (González-Díaz et al. 2024, BETIS I henceforth). Section 3 shows a description of the ionisation structure and features found in the halo of IC1553 and the connection of the eDIG with the disc for all the sample. Section 4 presents a set of star formation and fast shocks hybrid models to explain the ionisation structure found the halo. In section 5 we show the results of applying the methodology and models of section 4 for the rest of the sample and finally, section 6 outlines the main findings in this paper.

The following notation is used throughout the paper: $[\text{N II}] \equiv [\text{N II}] \lambda 6584$; $[\text{S II}] \equiv [\text{S II}] \lambda 6717 + [\text{S II}] \lambda 6731$; $[\text{O III}] \equiv [\text{O III}] \lambda 5007$; and $[\text{O I}] \equiv [\text{O I}] \lambda 6300$. We adopt the standard Λ CDM cosmology with $H_0 = 70 \text{ km/s/Mpc}$, $\Omega_\Lambda = 0.7$, $\Omega_M = 0.3$.

2. The data

The characterisation of the eDIG and the exploration of its ionisation mechanisms, as for the case of the face-on galaxies, requires spatially resolved data and spectral information. This is particularly crucial for the eDIG, as the galactic halos may exhibit diverse mechanisms and structures that could contribute to the formation of the ionised extraplanar gas (Levy et al. 2019). These include phenomena such as plumes, fountains, filaments, gas accretion or gas outflows/inflows (Rand 1996; Rossa & Dettmar 2003a,b; Kaufmann et al. 2006; Marinacci et al. 2011; Combes 2014; Levy et al. 2019; Com19).

For this reason, as in BETIS I, we use MUSE IFS data to undertake this task. In particular, the sample of Com19 aligns well with the previous criteria. The sample, listed in table 1, consists on eight edge-on ($i > 75^\circ$) nearby galaxies ($z < 0.01$, $D < 46 \text{ Mpc}$) with high spatial resolution (full width at half maximum (FWHM) $< 200 \text{ pc}$) from the 096.B-0054(A) and 097.B-0041(A) very-large telescope (VLT) programmes. Table 1 shows the integrated star formation rate (SFR) in the disc spans between $0.024 \text{ M}_\odot/\text{yr} < \text{SFR} < 0.229 \text{ M}_\odot/\text{yr}$. It was obtained using the Kennicutt & Evans (2012) relation: $\log(\text{SFR}) = \log(L_{\text{H}\alpha}) - 41.27$, with $L_{\text{H}\alpha}$ as the $\text{H}\alpha$ luminosity, corrected for interstellar extinction assuming the Cardelli extinction law, assuming $R_V = 3.1$ (Cardelli et al. 1989) and a Balmer decrement $\text{H}\alpha/\text{H}\beta = 2.87$. The galaxies are then normal-disc galaxies with low star formation. This is consistent with the classification of these galaxies in the star formation main sequence, with specific SFR ranging between $-10.5 < \log(\text{sSFR}/\text{yr}) < -9.92$, corresponding barely to star-forming galaxies (using MUSE data and $3.6 \mu\text{m}$ stellar masses; Muñoz-Mateos et al. 2015; Zaragoza-Cardiel et al. 2020; Rautio et al. 2022).

This sample, observed with MUSE, was selected since this type of investigation requires more constraints compared to

Table 1: General characteristics of the eBETIS sample, in order of declination.

Galaxy	RA (J2000) (deg)	DEC (J2000) (deg)	Type	z	D (Mpc)	P.A. (°)	FWHM (pc)	Incl. (°)	log SB lim. (erg/s/kpc ²)	Bin size (pc)	L _{eDIG} (H α) (erg/s)	log SFR _{Disc} (M \odot /yr)
IC217	34.0435	-11.9267	Scd	0.00630	24.32	35.7	117.91	82.6	35.6	94.3	39.11	0.063
PGC28308	147.5582	-12.0576	Scd	0.00907	45.22	125.2	153.46	85.5	35.2	175.4	39.12	0.084
PGC30591	156.3603	-15.3492	Sd	0.00676	35.22	169.2	187.83	86.6	36.0	136.6	39.13	0.055
ESO544-27	33.2277	-19.3168	Sb	0.00818	32.81	153.3	159.07	90.0	35.0	127.2	38.92	0.024
IC1553	8.1671	-25.6075	Irr	0.00979	32.25	15.0	171.99	78.6	36.5	125.1	39.80	0.229
ESO443-21	194.9412	-29.6002	Scd	0.00941	40.31	160.8	195.45	79.0	36.6	156.4	39.71	0.184
ESO469-15	347.2317	-30.8579	Sb	0.00545	19.81	149.2	86.44	90.0	35.9	76.9	38.90	0.029
ESO157-49	69.9036	-53.0126	Sc	0.00559	24.82	30.4	96.26	79.3	35.3	96.3	39.46	0.060

Notes. The columns represents, from left to right: The designation of the galaxy, the RA and DEC in the J2000 epoch, the morphological Hubble type, the redshift, the distance in Mpc, the position angle (in deg), the PSF FWHM in pc, inclination with respect to the line of sight (in deg), the 2σ $\Sigma_{H\alpha}$ limit and the average physical size of the bins in pc. The RA, DEC, the morphological type, the redshift and distances are obtained from NED. The position angles and inclinations are obtained directly from Com19 and Hyperleda. The last columns represent the integrated H α luminosity within the eDIG and the integrated star formation rate (SFR) of the disc (see section 2).

the face-on case, since we are navigating within the galactic halo, where the signal-to-noise ratio of the observed emission line (S/N, Rosales-Ortega et al. 2012; BETIS I) is lower. Consequently, besides high resolution, we require data as deep as possible to observe low surface brightness lines such as [O I] and [O III], alongside data of sufficient quality to measure the [O I] line without interference from sky lines.

The MUSE instrument brings 1 arcmin² of field of view (FoV), with a spatial and spectral sampling of 0.2×0.2 arcsec and 1.25 Å respectively within a spectral range of 4650 – 9300 Å. Every datacube consists in four exposures (three for IC217) of 2624 seconds, and at least half of the galaxy is covered by one VLT pointing (from the centre to one of the edges of the galaxy, i.e., $0.5R_{25} < 1$ arcmin). The data was originally reduced using the ESO data-reduction phase 3 using the MUSE pipeline (Weilbacher et al. 2020), and subsequently Com19 performed a sky subtraction using the ZAP software (Soto et al. 2016, see Com19 for more details).

This dataset has previously been used to analyse the eDIG in prior studies. Rautio et al. (2022) employed five of these galaxies, in conjunction with H α and GALEX-FUV imaging, while Dirks et al. (2023) exclusively utilised IC1553 for a more comprehensive examination of the eDIG ionisation mechanisms within this galaxy. In our paper, we use all eight galaxies from this dataset¹ (eBETIS sample henceforth) to perform an exhaustive spectral and spatial exploration of the eDIG structure and ionisation for every galaxy in particular.

To conduct this exploration, we first extract the emission line features of the eBETIS sample in the form of binned emission line maps, following the same procedure described in BETIS I: we employ our own adaptive binning algorithm to the original datacubes, setting a S/N target of 10 based on [S II], since this line is one of its main features of the eDIG and DIG in general, as well as it typically exhibits low S/N in both planar DIG and eDIG. Subsequently, we perform a simple stellar population (SSP) synthesis to the binned datacube using STARLIGHT (Cid Fernandes et al. 2005) to the integrated spectra of each bin. This is followed by Gaussian fitting to every emission line of interest present in each resulting nebular spectrum (see BETIS I for more details). This procedure finally results in the binned emission line maps for the H α , H β , [O III] λ 5007, [N II] λ 6548, 83, [S II] λ 6717, 31 and [O I] λ 6300 lines. The average sensitivity of the sample is $35.7 \log(\text{erg/s/kpc}^2)$, obtained as the 2σ of the distribution of H α surface brightness ($\Sigma_{H\alpha}$) of the bins of ev-

¹ We downloaded the reduced datacubes directly from the ESO archive science portal.

ery H α map. The average physical size of the bins is below 175 pc. Since the average point-spread function (PSF) FWHM of the sample is below 200 pc, the binning does not significantly restrict the resolution in our galaxies.

Figure 1 shows the binned H α maps of the eBETIS sample. For aesthetic purposes and to highlight the contrast between the galactic plane and the complex structure of the extraplanar gas, the plane of the galaxies is shown in greyscale. To define the galactic plane, we construct an elliptical mask by conducting a 2D Gaussian fitting to the binned H α image using the PYTHON routine SCYPY.OPT.CURVE_FIT², and centring the ellipse in the coordinates of the centre of the galaxy, which also coincides with the centre of the rotation curve of the galaxy. The midplane is then set at $z = 0$, being z the distance from the midplane, that corresponds to the centre of the minor axis of the ellipse fitted. The integrated H α luminosity of the eDIG for all the galaxies is listed in Table 1. It was obtained integrating the H α flux outside the ellipses previously described, and we obtain an average value of $2.5 \cdot 10^{39}$ erg/s, that is consistent with values obtained by previous authors (Rand 2000; Miller & Veilleux 2003; Jo et al. 2018).

In our data, for the subsequent analyses, we only include bins with S/N of the observed emission line greater than 2 and relative error lower than 40% for all the lines of interest. The resulting binned maps exhibit an average physical bin size (listed in table 1) that remains below, or very similar to, the FWHM of the data, determined as the physical size of the seeing reported in the datacube header.

3. The complex morphology of the eDIG

The H α maps of Figure 1 reveal the complex structure of the extraplanar gas in normal disc galaxies. The most discernible morphological structures observed in the outer regions of the galaxy are the filaments. In galaxies such as ESO157-49 and IC1553, these filaments are especially visible, emerging from the galactic plane and extending more than 2 kpc from the midplane. Other structures can be observed, for instance, in ESO443-21, which features a thick knot-shaped filament around the galactic centre that reaches a distance of ~ 4.5 kpc from the midplane.

The presence of structures in the halo becomes more evident when examining the maps of the [N II]/H α , [S II]/H α , [O I]/H α , and [O III]/H β line ratios. These maps reveal new ionised features that were initially invisible when only exam-

² SCYPY.OPT.CURVE_FIT documentation.

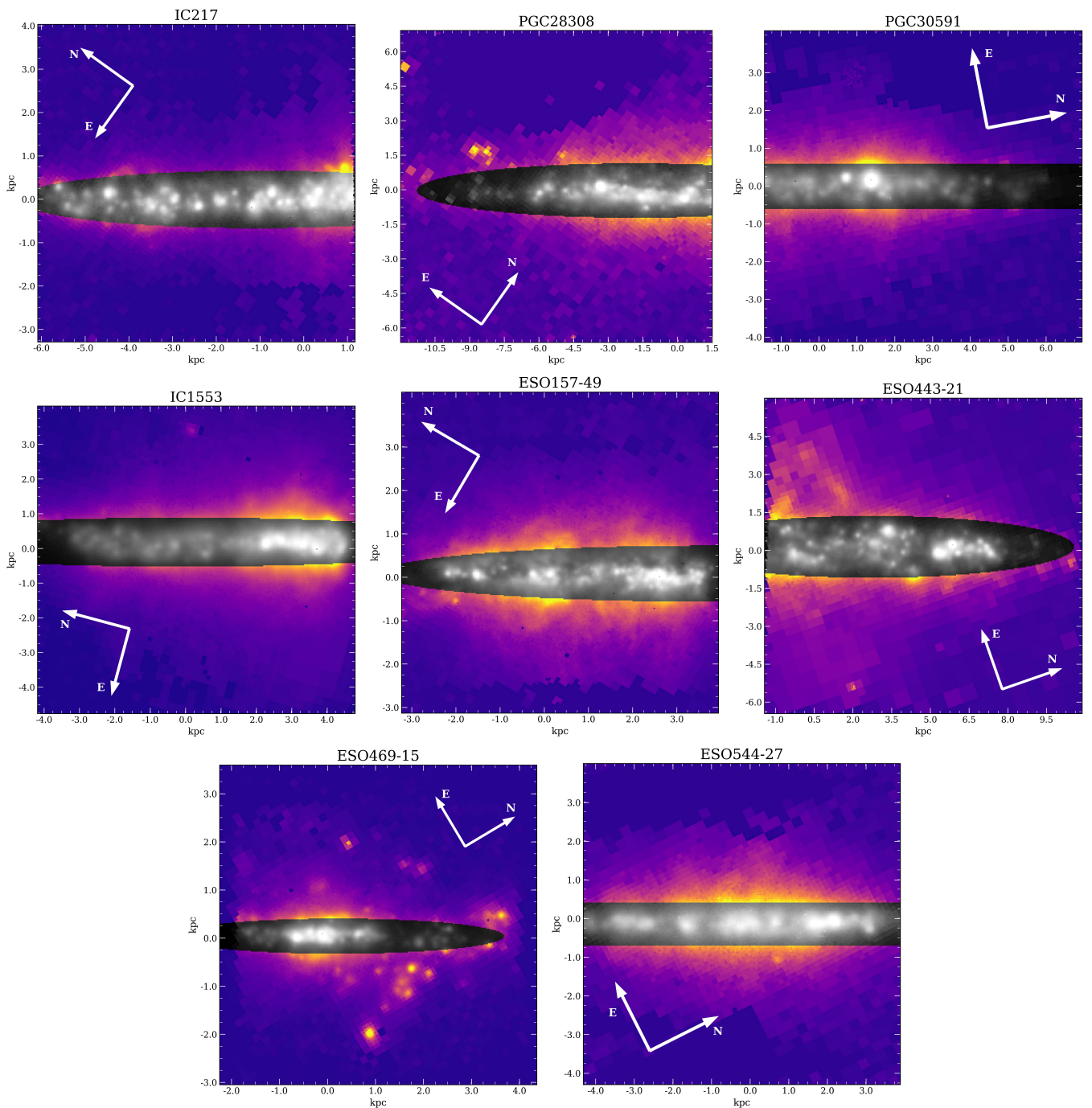


Fig. 1: eBETIS sample. The images correspond to the binned $H\alpha$ emission line maps obtained in Sec. 2. Each image is rotated PA- 90° with the white arrows indicating the direction of the celestial north and east in the original image. The ellipse fitting of galactic plane (see Sec. 2) is coloured in grey scale. The contrast between the galactic plane and the extraplanar gas reveals the complexity of the ionised extraplanar gas, which comprises diffuse gas, filaments, and various structures.

ining the H II images. For instance, Figure 2 shows the binned maps of the mentioned lines ratios of the IC1553 galaxy.

The images show the intricate and asymmetrical structure of the eDIG. Having differences of 0.4 dex in the $[S II]/H\alpha$ ratio along the major axis and over 0.8 dex in $[N II]/H\alpha$. Additionally, the line ratios increase with respect to the distance from the mid-plane, a phenomenon that is well-documented in the literature (Rand 1998; Levy et al. 2019). However, the 2D spectroscopic analysis of the eDIG allows to recognise that the variation of the

line ratios are dependent not only on height, but along the major axis distance (MAD) of the galaxy.

Between $1.5 \text{ kpc} \lesssim \text{MAD} \lesssim 4.5 \text{ kpc}$, the $[N II]/H\alpha$ ratio presents significantly lower values than the range between $-1 \text{ kpc} \lesssim \text{MAD} \lesssim 1 \text{ kpc}$, showing a conical-shaped structure that is slightly off-centred with respect to the galaxy. These features are also reported by other authors (Rautio et al. 2022; Dirks et al. 2023). However, with the adaptive binning method applied (BETIS I), we recover data with $S/N > 2$ at $z > 3$, sampling almost the entire MUSE FoV in this galaxy and also in the rest of

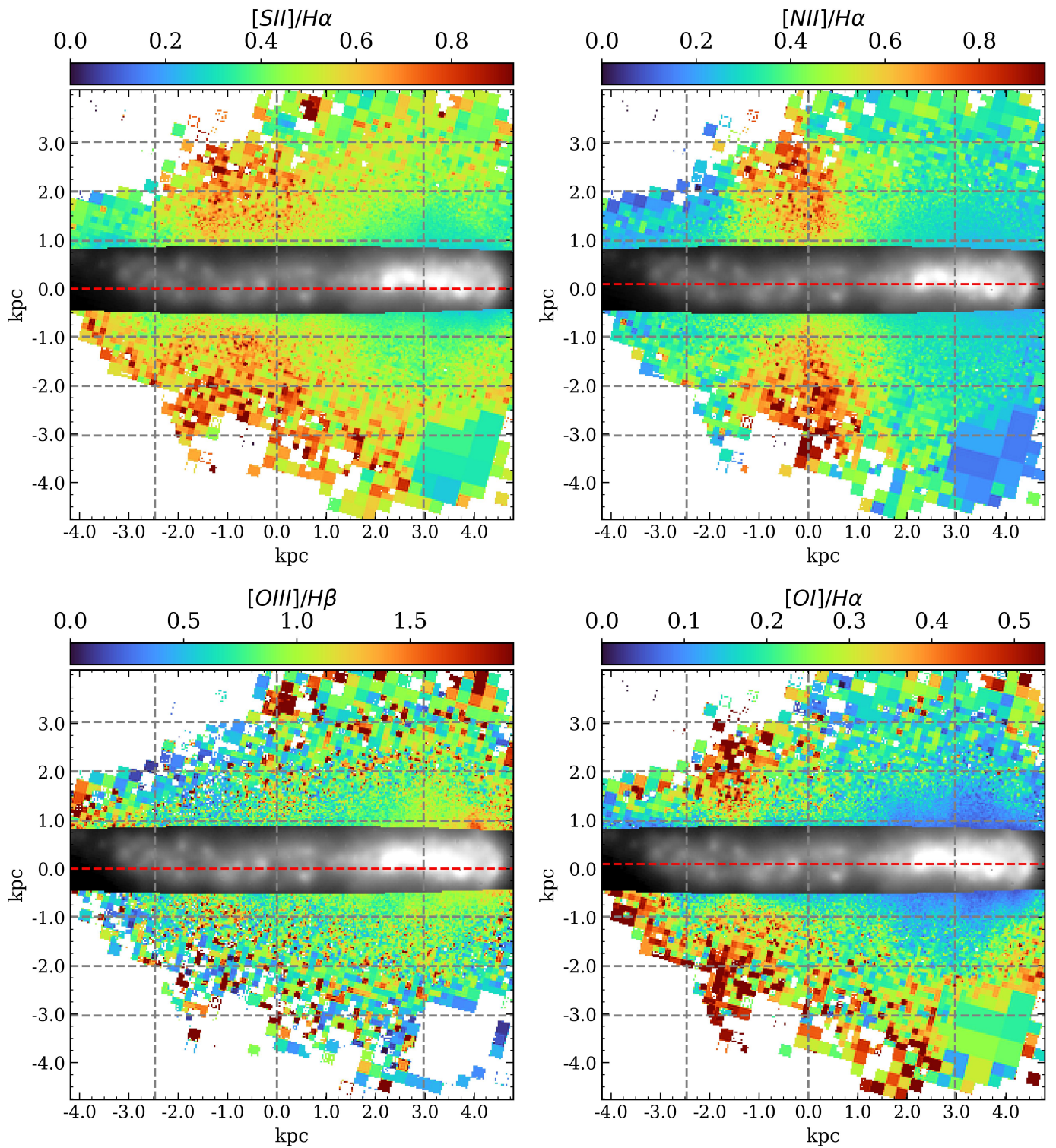


Fig. 2: IC1553 line ratio maps. Every map is masked, excluding those bins with $S/N < 2$ or relative error greater than 40% for the respective lines. We overlay the same $H\alpha$ map of the galactic plane masked in Figure 1. The dashed red line indicates the midplane, located at $z = 0$. The y-axis is re-scaled in function of the galaxy inclination. In this case, the galactic plane is defined as a rectangle with the minor side equal to the minor axis of the fitted ellipse and the major side extending the full length of the x-axis. The grey dashed lines indicates the heights with respect the midplane $z = \pm 1, \pm 2, \pm 3$ kpc and major axis distances $MAD = -2.5, 0, 3$ kpc.

the galaxies. Besides, this apparent conical structure is shifted at $MAD = -0.5$ kpc in the $[SII]/H\alpha$ ratio, and at $MAD = -1.5$ kpc at $[OI]/H\alpha$ ratio, being not present in the $[OIII]/H\beta$ ratio. This asymmetry in the halo coincides with the asymmetry observed

in the galactic plane, where most of the $H\alpha$ emission from the HII regions is concentrated between $1 \text{ kpc} \lesssim MAD \lesssim 3.5 \text{ kpc}$. At this radial range, the line ratios found in the eDIG resemble more closely the line ratios of the HII regions rather than the

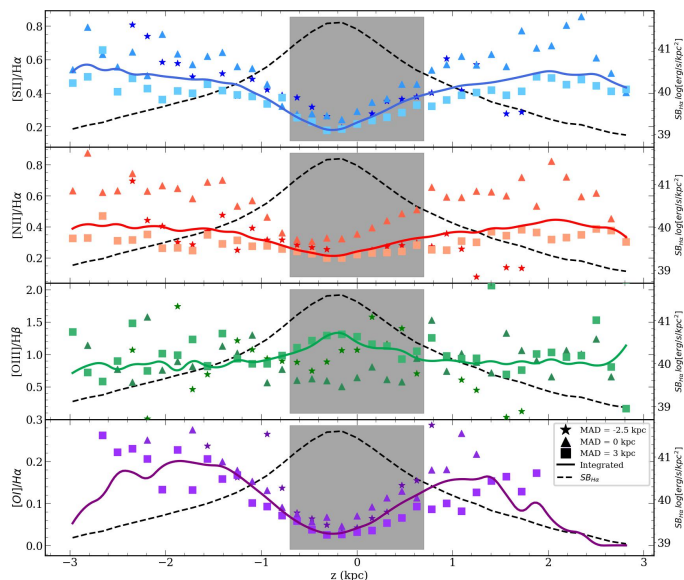


Fig. 3: Distribution of the line ratios with respect the distance from the midplane for the IC1553 galaxy. The stars, triangular and square markers represent the line ratio at that z for MAD = -2.5, 0 and 3 kpc respectively, analogous to a long-slit perpendicular to the galactic plane at a given MAD. The solid lines represents the integrated values along the major axis. The dashed black line represents the $\Sigma_{H\alpha}$ height distribution of the galaxy. The grey background between $z = -0.7$ kpc and 0.7 kpc represents the galactic plane.

typical DIG line ratios (below 0.3 and 0.4 in the $[N II]/H\alpha$ and $[S II]/H\alpha$, and below 0.1 in $[O I]/H\alpha$; [BETIS I](#)).

In the appendices from [A](#) to [H](#), we present the line ratio maps for the rest of the sample, where the complex bidimensional structure of the eDIG and its apparent connection between the line-of-sight H II regions of the galactic plane is evident for all galaxies.

Figure 3 shows the distribution of the eDIG characteristic line ratios with respect the distance from the midplane for IC1553. The stars, triangles, and squares represent the values of the line ratio at that height for MAD equal to -2.5 kpc, 0 kpc, and 3 kpc, respectively. Analogously, this corresponds to the line ratio height distribution in a long-slit located at those MADs and perpendicular to the galactic plane. The solid lines are constructed then integrating the fluxes along the major axis. The dashed lines represent the $\Sigma_{H\alpha}$ distribution, constructed similarly to the solid lines by integrating the $H\alpha$ flux along the major axis, and the grey background represents the location of the galactic plane. Since the H II regions distribution is not symmetrical with respect $z = 0$, the minimum of the $\Sigma_{H\alpha}$ and line distributions are shifted with respect $z = 0$.

The integrated distribution of the $[N II]/H\alpha$, $[S II]/H\alpha$ and $[O I]/H\alpha$ line ratios tends to increase in height, reaching a minimum inside the galactic plane. The $[N II]/H\alpha$ and $[S II]/H\alpha$ line ratios increase up to 0.4 and 0.6, respectively, from $z = 0$ to 2 kpc, and then remain constant. $[O I]$ also increases from $z = 0$ to 2 kpc, reaching up to 0.2, but then decrease dramatically. This line ratios seems anti-correlated with the $\Sigma_{H\alpha}$ vertical distribution. In contrast, for the $[O III]/H\beta$ ratio, at $z = 0$ it reaches its maximum of 1.3 and then decreases slowly to 0.7.

This trend is consistent with findings from previous studies in other edge-on galaxies ([Rand 1998, 2000](#); [Collins & Rand](#)

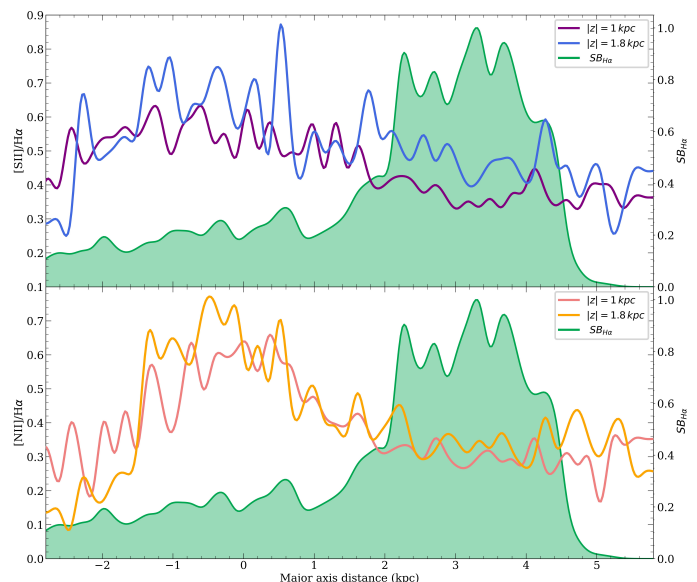


Fig. 4: Major axis distance (MAD) distribution of the $[N II]/H\alpha$ and $[S II]/H\alpha$ lines for IC1553 at $z = 1$ and 1.8 kpc. In green, the normalised $\Sigma_{H\alpha}$ MAD distribution, constructed integrating the $H\alpha$ flux within the ellipse fitted in section 2 throughout the major axis. Both line distributions show a correspondence with the $\Sigma_{H\alpha}$ distribution, decreasing and showing more difference between both heights as the $\Sigma_{H\alpha}$ increase. This tendency is consistent for all galaxies.

[2001](#); [Haffner et al. 2009b](#); [Ho et al. 2016](#); [Dirks et al. 2023](#)). However, in addition to this, when restricting the height distributions to specific MADs, the overall behaviour of the distributions remains consistent, but the line ratios exhibit notable differences. At MAD = 3 kpc (represented by squares in Figure 3, where the most prominent H II regions emission is observed in Figure 2), the $[N II]/H\alpha$, $[S II]/H\alpha$ and $[O I]/H\alpha$ line distributions follow the same trend as their respective integrated distributions, but consistently reach lower values. Similarly, at MAD = 0 (represented by triangles in Figure 3, where the H II regions emission observed in Figure 2 is lower), the line distributions also follow the same trend, but consistently reach higher values. This behaviour in the line ratio distributions is consistent in all the galaxies, as shown in the appendices from [A](#) to [H](#).

Figure 4 shows the MAD distribution of the $[N II]/H\alpha$ and $[S II]/H\alpha$ lines for $z = 1$ and 1.8 kpc, as well as the normalised $\Sigma_{H\alpha}$ MAD distribution of IC1553. Two effects are noticeable in this figure: Firstly, all the line ratio distributions tend to be lower between 2 kpc and 4.5 kpc, where the $\Sigma_{H\alpha}$ is higher, and increase while the $\Sigma_{H\alpha}$ decreases, particularly for the $[N II]/H\alpha$ ratio. Secondly, the effect of the increment of the line ratio with height, as seen in Figure 3, remains present along the major axis, with the difference being clearer in regions of high $\Sigma_{H\alpha}$, especially for the $[S II]/H\alpha$ ratio, where there is a constant difference of 0.1 between both distributions. These effects are not exclusive to IC1553, the MAD distributions present the same behaviour for all galaxies in the sample (see appendix). These figures evidences the high complexity that the eDIG presents, suggesting that the physical conditions in the eDIG are influenced by the distribution of the H II regions emission along the galactic plane.

4. Discussion

4.1. The linkage between the galactic plane and the eDIG

The correlation between the morphological distribution of star-forming regions in the disks of edge-on galaxies and the shapes and morphology of the halos presents the strongest evidence supporting the interpretation that energy sources from star formation (SF) within the galaxy disks drive the observed disk-halo interactions (Norman & Ikeuchi 1989; Dahlem 1997). Over the past decade, there has been a unanimous consensus in the literature that the primary ionisation mechanism for the WIM (DIG) and the eDIG is attributed to star formation in the discs of late-type galaxies (Ho et al. 2016; Boettcher et al. 2019; Levy et al. 2019; Werle et al. 2019; Belfiore et al. 2022; Della Bruna et al. 2022a,b; Rautio et al. 2022; Tacchella et al. 2022; Dirks et al. 2023; Lu et al. 2023; Sardaneta et al. 2024, etc.). Specifically, Lyman continuum (LyC) photons leaking from OB associations in the galactic discs escape into the ISM in the halos through transparent pathways, ionising layers of low-density gas that can be traced out to distances of up to 5 kpc or more from the midplane of the disks (Haffner et al. 2009b; Weber et al. 2019a).

The specifics of the underlying mechanisms governing the disc-halo connection are complex and widely debated. From an energetic perspective, several external sources have been proposed to account for the origin of the eDIG. These include gas accretion from the intergalactic medium (IGM, e.g. Binney 2005; Putman 2017) and the circumgalactic medium (CGM, e.g. Levy et al. 2019; Bizyaev et al. 2022), the latter also being suggested as a probable origin of the UV halo (e.g. Hodges-Kluck et al. 2016; Shinn & Seon 2015) or a hot halo (Marasco et al. 2012; Li et al. 2023). However, in a recent study, Sardaneta et al. (2024) argue, using a sample of nearby highly inclined ($i \geq 80^\circ$), isolated galaxies, that the eDIG phenomenon is uncorrelated with the galaxy environment. Consequently, the primary energy sources driving the disc-halo interactions should reside within the galaxy discs, as no other pervasive external energy sources are known that could account for the observational data (Dahlem 1997). Therefore, the halo gas expelled or heated by these energy sources must also originate from the discs.

Several heating mechanisms have been proposed to account for the energetics observed in the halos of galaxies: AGNs and high-level star formation, or a combination of both. In the case of AGNs, many spirals exhibit very characteristic outflow cones associated with a nuclear engine, which can be traced using X-rays, radio continuum emission, and optical emission-line maps (e.g. Wilson & Tsvetanov 1994; Colbert et al. 1996; López-Cobá et al. 2019). However, considering that only 10–15% of galaxies in the local universe ($z < 0.1$) exhibit AGN activity, and that disk-halo interactions are observed over extensive regions of the discs, AGNs cannot be the common cause for the observed disk-halo interactions. Indeed, no AGNs are found in the eBETIS sample (Sec. 2) or in recent eDIG studies of normal late-type galaxies (Ho et al. 2016; Levy et al. 2019; Lu et al. 2023).

On the other hand, high-level SF can occur in various locations within galaxy discs, either in circumnuclear starbursts or in giant H II regions dispersed across the discs. Several scenarios for the disk-halo interaction due to SF have been proposed: the superbubble breakout model (e.g. Mac Low & McCray 1988), the galactic fountain model (Shapiro & Field 1976), the champagne model (Tenorio-Tagle 1979), the chimney model (Norman & Ikeuchi 1989), and the galactic wind model (Veilleux et al. 2005, and reference therein). For the discussion purpose, we exclude phenomena related to nuclear activity in galaxies or incoming gas from the IGM/CGM, and we focus on those models

in which ionising radiation originating from SF must not only escape the H II regions but also traverse the dense clouds of neutral hydrogen near the midplane.

In the galactic fountain model, the outflow velocities are expected to be lower than the escape velocity of the gas ($v < v_{esc}$), indicating that all material will ultimately return to the disc, resulting in a dynamic circulation of matter as the primary mechanism of the disc-halo interaction. In the chimneys model, OB associations are born within giant molecular clouds, and the ionising ultraviolet flux and stellar winds from successive generations of OB stars provide significant momentum input, creating free cavities in the surrounding ISM. The sequential explosions of supernovae (SNe) result in the formation of a dense, cool wall of neutral gas and a central flow of hot gas, which constitutes a chimney. The total energy output from stellar winds is comparable to that of SNe, albeit released over a more extended period. For a simple instantaneous starburst model with a canonical IMF and a total mass of $10^6 M_\odot$, the total energy is approximately 10^{55} ergs (Leitherer et al. 1992). The hot gas ascends to the halo through the chimneys, reaching distances of several kpc. In this model, the chimneys create vertical channels that facilitate the rapid propagation of SN-driven shocks, with gas velocities reaching $v \geq v_{esc}$, thereby enabling the ejection of matter into intergalactic space. The gas rises to ≥ 3 kpc and returns to the disk after a dynamical time of $\sim 10^7$ years with an infall velocity of $< 10^2$ km s $^{-1}$, resulting in an ongoing exchange of mass, energy, and momentum. For canonical Galactic parameters, the chimney phase is associated with a mass flow rate of $0.3 - 3 M_\odot$ yr $^{-1}$ and a global power input of 10^{40-42} ergs s $^{-1}$ (Norman & Ikeuchi 1989).

This scenario aligns with the observed multiphase nature of the halo ISM (Rossa & Dettmar 2003a; Rich et al. 2010). The chimney model can be described as an intermediate state between a two-phase model (Field 1989)—relevant in galaxies with higher mean ambient density—and a three-phase model (McKee & Ostriker 1977), in which the third hot phase consists of chimneys with a filling factor of about 10% (Norman & Ikeuchi 1989). In both models, disk-halo interactions occur, but in the fountain mode, the energy input over the disk is distributed across extensive areas, whereas in the chimney mode, the energy injection into the ISM is more localised.

Independent of the various outflow scenarios, they provide absorption-free pathways for H-ionising photons into the halo, as well as channels for the vertical transport of hot processed material and cosmic rays into the halo, where a hot gas phase with temperatures of up to $\sim 10^7$ K has been observed. This X-ray emitting plasma offers a further compelling argument favouring SF-related processes as the heating sources of the halo, given that the cooling time for such gas is very short, requiring continuous heating. Indeed, several authors have identified stellar winds and SNe as the principal energy sources driving this process (Weaver et al. 1977; Gray et al. 2019; Sarkar et al. 2022).

However, real galaxies exhibit greater complexity than the models depicted. For instance, the Type II supernova rate and the average gas density at the disc can vary with galactocentric distance, resulting in different processes and phases occurring at various radii within the same galaxy. Additionally, these parameters can fluctuate over time, especially in galaxies experiencing bursts of star formation throughout their lifetimes. The total SFR, the distribution of H II regions, and the local level of star formation in different regions across a galactic disk are not constant over time. Galaxies may undergo cycles of star formation, implying they might temporarily be in states of high, intermediate, or quiescent phases of star formation (Rosa & Richter

1988). The natural extension of the disk ISM into the halo via star-formation-driven outflows also indicates that the halo ISM is dynamic rather than static. The multiphase ISM exists under the influence of both the galaxy's gravitational potential and the energy input from heating sources, leading to interactions between different phases and constituents of the ISM. Consequently, in the presence of ionising UV radiation from hot massive stars, stellar winds, and supernova shock waves, the ISM in galaxy halos is never in local thermodynamic equilibrium.

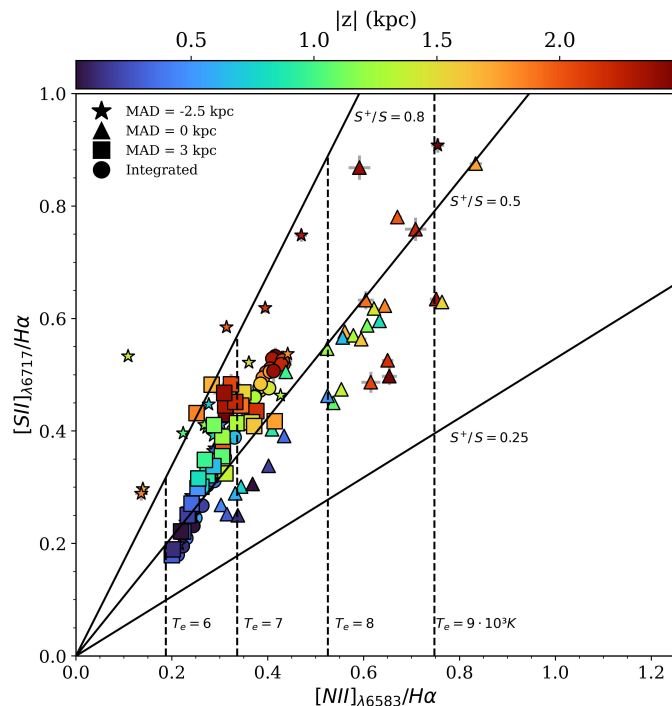


Fig. 5: $[N II]_{\lambda 6583}/H\alpha$ vs. $[S II]_{\lambda 6717}/H\alpha$ diagnostic diagram for IC1553. Colours represent height with respect the midplane, equally from above or below the plane. Vertical dashed lines are the theoretical ratios obtained from 1 at a constant T_e (6, 7, 8 and 9 in units of 10^3 K respectively). Solid lines represent the theoretical ratios from equations 1 and 2 for a fixed S^+/S (0.25, 0.5, 0.8 respectively). The circles indicate the line ratios obtained by integrating the fluxes along the major axis at a certain z . Stars, triangles and squares indicate the line ratio at a certain z for $MAD = -2.5, 0$ and 3 kpc respectively.

The morphology and properties of gaseous halos are influenced by the level of SF activity in the underlying disk (Rossa & Dettmar 2003a). Galaxies require a sufficient level of SF to sustain a widespread extraplanar eDIG layer (Dahlem et al. 1995). Here, it is essential to distinguish between pure starburst galaxies (typically with circumnuclear SF, e.g. M82) and normal galaxies with varying levels of widespread SF in their disks. For the latter, it is known that the most actively star-forming galaxies possess the most prominent halos (Dahlem 1997). In galaxies with intermediate SF levels, such as those in the eBETIS sample, disk-halo interactions occur only in regions with high SFR. Theoretical calculations indicate that only those regions surpassing a threshold of 10^{-2} ergs s^{-1} cm^{-2} are capable of initiating disk-halo interaction (Dahlem et al. 1995).

Indeed, the connection between the $\Sigma_{H\alpha}$ distribution and the ionisation structure of the eDIG in the eBETIS galaxies (see Sec. 3) demonstrates a clear correlation between the morphology of

halo emission and the distribution of SF regions and complexes in the underlying galaxy disks. Furthermore, the detection of extended eDIG in the halos of the eBETIS sample indicates that even low-mass galaxies with modest SFR (Tables 1 and 2) are capable of producing a pervasive layer of extraplanar diffuse ionised emission. This finding contradicts previous assumptions that halos are a rare phenomenon among normal spirals (Hummel et al. 1991), a bias likely caused by the insufficient sensitivity of earlier observations.

In the following, we discuss the observational evidence supporting this scenario as derived from the eBETIS sample.

4.2. The ionisation mechanism of the eDIG

In the scenario delineated above, the eDIG emission originates in situ within low-density gas environments, induced by ionising photons propagated from the galactic disk via transparent conduits formed by superbubbles or chimneys. However, the precise underlying physics explaining the large distance between the extraplanar gas and ionising stars in the midplane, as well as the fine-tuned details of the ionisation mechanism of the eDIG, remain a topic of ongoing debate.

Long-standing issues regarding the specifics of OB-star-driven ionisation remain prevalent in the literature. A notable characteristic of the DIG that proves difficult to explain through OB star photoionisation is its optical emission-line spectrum. Should the eDIG be ionised by radiation escaping from the midplane H II regions, the spectrum of the ionising radiation would be expected to resemble that of the OB star (or the SED dominated by such stars). Consequently, one would anticipate similar emission-line spectra in the eDIG as in the H II regions. Nonetheless, certain observed optical emission line ratios are not explicable by pure photoionisation from OB stars. The distinctive emission-line ratios observed in the eDIG, namely $[N II]_{\lambda 6584}/H\alpha$, $[S II]_{\lambda 6717}/H\alpha$, $[O III]_{\lambda 5007}/H\beta$ and $[O I]_{\lambda 6300}/H\alpha$, are elevated compared to those observed in H II regions (Rand 1997, 1998; Collins & Rand 2001; Haffner et al. 2009b; Seon 2009), as illustrated in Fig. 3 and elaborated upon in Sec. 3 for the eBETIS sample, indicating the relative significance of additional heating processes.

Some of the differences between the DIG and H II region emission-line spectra (i.e., enhanced $[N II]/H\alpha$ and $[S II]/H\alpha$) can be explained by differences in temperatures. In a model of photoionised gas, the temperature is determined by the equilibrium between heating and cooling mechanisms. Heating is facilitated through the thermalisation of the excess kinetic energy of electrons during the photoionisation-recombination process, whereas cooling predominantly arises from collisional excitation followed by radiative decay of metastable states of trace ions (Osterbrock & Ferland 2006).

Relative temperatures can be explored by analysing the emission line ratios of the forbidden lines with respect to the H-recombination emission. The line intensities of $[N II]$ and $[S II]$ relative to $H\alpha$ probe the ionisation fractions (X^+/X) and elemental abundances of ionised the gas, showing a strong dependence on the electron temperature (T_e). These parameters relate with the line intensity ratios as follows (Haffner et al. 1999; Osterbrock & Ferland 2006):

$$\frac{I([N II]_{\lambda 6583})}{I(H\alpha)} = 1.63 \cdot 10^5 \left(\frac{N^+}{N}\right) \left(\frac{N}{H}\right) \left(\frac{H^+}{H}\right)^{-1} T_4^{0.426} e^{-2.18/T_4}, \quad (1)$$

$$\frac{I([\text{S II}]_{\lambda 6717})}{I(H\alpha)} = 7.64 \cdot 10^5 \left(\frac{S^+}{S}\right) \left(\frac{S}{H}\right) \left(\frac{H^+}{H}\right)^{-1} T_4^{0.307} e^{-2.14/T_4}, \quad (2)$$

with T_4 being the electron temperature in units of 10^4 K.

We assume that usually the 100% of the hydrogen and the 80% of the nitrogen are ionised in the DIG, varying little within the DIG and basically tracing the T_e (Sembach et al. 2000; Otte et al. 2002; Haffner et al. 2009b). We also assume solar abundances: $N/H = 6.8 \cdot 10^{-5}$ and $S/H = 1.3 \cdot 10^{-5}$ (Asplund et al. 2021).

Haffner et al. (1999) and Madsen et al. (2006) used these relationships to build diagnostic diagrams to estimate both T_e and S^+/S from observations of $[\text{N II}]/H\alpha$ and $[\text{S II}]/H\alpha$. Given that H and N have similar first ionisation potentials (13.56 eV and 14.5 eV, respectively) and a weak charge-exchange reaction, and assuming that N is not doubly ionised, then $N^+/N^0 \sim H^+/H^0$ vary little within the DIG, so that variations in $[\text{N II}]/H\alpha$ essentially traces variations in T_e (Sembach et al. 2000; Otte et al. 2002; Haffner et al. 2009b). Figure 5 shows the distribution of $[\text{N II}]_{\lambda 6583}/H\alpha$ vs. $[\text{S II}]_{\lambda 6717}/H\alpha$ line ratios in function of $|z|$ for IC1553. Circles are the integrated along the major axis for a certain z . Stars, triangles and squares are bins at $MAD = -2.5, 0$ and 3 kpc respectively. We use the equations 1 and 2 to show the predicted ratios for a constant T_e (6, 7, 8 and 9 in units of 10^3 K) and S^+/S (0.25, 0.5 and 0.8).

The general behaviour indicates a linear, constant increment of T_e with increasing distance from the galactic plane. This trend is consistent with previous studies of the WIM in the Galaxy (Haffner et al. 2009b; Madsen et al. 2006) and with long-slit observations perpendicular to other edge-on galaxies (Collins & Rand 2001; Otte et al. 2001; Hoopes & Walterbos 2003; Boettcher et al. 2019). However, the spatial coverage of the eBETIS galaxies permits the study of the dependence of the eDIG line ratios on temperature at different MADs. Figure 5 illustrates significant variations in T_e and S^+/S with respect to the line of sight. For instance, at the galaxy minor-axis ($MAD = 0$), the temperature increases from 7 to 9×10^3 K and the S^+/S ratio rises from 0.3 to 0.5, whereas at $MAD = -2.5$ kpc, the S^+/S ratio attains high values of approximately 0.8 at all vertical distances. At $MAD = 3$ kpc, the temperature of the eDIG is confined to a narrow range between $6 - 7.5 \times 10^3$ K, with $S^+/S \approx 0.5 - 0.8$. To comprehend the variations in S^+/S , we could examine the energetics of the eDIG trace ions. The ionisation energies of N and S are 14.5 eV and 10.4 eV, respectively. If N is mostly ionised, then S should also be mostly ionised. However, the energy required to double-ionised S is 23.3 eV ($S^+ \rightarrow S^{++}$), while for N is 29.6 eV ($N^+ \rightarrow N^{++}$). Therefore, S^+/S may vary while N^+/N remains constant if the ionising energy does not reach 29.6 eV. Consequently, we anticipate greater variation in S^+/S under eDIG conditions.

The variations in the temperature and ionisation structure of the eDIG as a function of spatial position within a single galaxy, as illustrated in Fig. 5, provide more compelling evidence of the intricate dynamical heating structure of the ISM in the halo of late-type galaxies. A similar trend is observed across the entire eBETIS sample, as depicted in the associated figures in the appendices, indicating that the eDIG tends towards a lower ionisation state (higher $S^+/S \sim 0.5 - 0.8$) compared to classical H II regions, which would be situated in the lower-left corner of these diagrams (e.g. $[\text{N II}]/H\alpha \approx 0.25$, $[\text{S II}]/H\alpha \approx 0.1$, Madsen et al. 2006). The anomalous $[\text{N II}]/H\alpha$ and $[\text{S II}]/H\alpha$ eDIG line ratios can be attributed to an increase in the T_e temperature in the halo, resulting from photoionisation with a low ionisation parameter q , i.e., the ratio of ionising photon density to

electron density, which measures the diluteness of the radiation field (Domgorgen & Mathis 1994). Nonetheless, while the elevated $[\text{N II}]/H\alpha$ and $[\text{S II}]/H\alpha$ line ratios can be explained by low q photoionisation, other eDIG line ratios, such as $[\text{O III}]/H\beta$ and $[\text{O I}]/H\alpha$, remain unexplained (Haffner et al. 2009b).

What remains puzzling in this scenario is the increase in T_e with respect to the midplane distance $|z|$, as supplementary heating sources may be necessary to account for this phenomenon. The literature has extensively debated the origin and characteristics of an additional source of ionisation to explain the observational features of the (e)DIG. The observed temperature behaviour of the eDIG, as depicted in Fig. 5, could be attributed to the spectrum of the ionising radiation being reprocessed as it traverses the ISM, an effect known as radiation hardening: a preferential absorption of photons near the ionisation thresholds within the sources' environment, resulting in (on average) more energetic photons escaping from the H II regions. This results in higher temperatures in the (e)DIG than in H II regions, which, in turn, leads to stronger emission of collisionally excited optical lines (Hoopes & Walterbos 2003; Wood & Mathis 2004; Wood et al. 2005; Haffner et al. 2009b). This model explains the WIM in our Galaxy but fails to explain an increasing $[\text{O III}]/H\beta$ ratio at large distances from the galactic plane (Weber et al. 2019a). Therefore, the rise in the $[\text{O III}]$ ratio with H-recombination lines with $|z|$ needs an additional source of heating and/or ionisation.

Several alternative heating mechanisms that may raise the electron temperature of the eDIG have been proposed, including differential absorption and/or scattering of radiation due to dust (Sokolowski 1993; Ferrara et al. 1996), dissipation of turbulence (Minter & Spangler 1997), magnetic reconnection (Reynolds et al. 1999; Hoffmann et al. 2012), photoelectric heating from small grains (Reynolds et al. 2001), cosmic rays heating (Wiener et al. 2013; Boettcher et al. 2019), etc. However, models still struggle to fully reproduce the (e)DIG emission-line spectrum.

A potential heating source that has gained prominence in the literature in recent years is the photoionisation by a hard spectrum produced by the high-temperature end of the white-dwarf distribution and the central stars of planetary nebulae. These low mass, hot, and evolved (post-AGB) stars, known as HOLMES, has been proposed as an ionisation mechanism for the DIG in general (e.g., Sokolowski & Bland-Hawthorn 1991; Lacerda et al. 2018; Belfiore et al. 2022; Lugo-Aranda et al. 2024) and for the eDIG in particular (e.g., Flores-Fajardo et al. 2011; Weber et al. 2019a; Rautio et al. 2022). HOLMES are abundant and smoothly distributed in the thick disc and lower halos of the galaxies, with scale heights greater than those of the OB stars. They are a significant source of ultraviolet emission, capable of reproducing the increment in the line ratios found in the (e)DIG, and specifically for the high ionisation species such as $[\text{O III}]$ (Flores-Fajardo et al. 2011). Indeed, Belfiore et al. (2022) and Lugo-Aranda et al. (2024) argue on the existence of two different types of diffuse emission based on the $EW_{H\alpha}$ bimodal distributions centered at ~ 1 and ~ 10 Å, which according to the classification by Lacerda et al. (2018), corresponds to the so-called hDIG ionisation (component dominated by HOLMES), and the ionisation of SF complexes (component dominated by unresolved H II region, or photons leaked from them), respectively.

The increase in the $[\text{S II}]/H\alpha$ and $[\text{N II}]/H\alpha$ ratios with distance from the midplane is commonly used to support HOLMES as an ionisation source in the eDIG (Flores-Fajardo et al. 2011; Rautio et al. 2022), as well as the radial behaviour of these lines in low-inclination spiral galaxies (Belfiore et al. 2022). Nevertheless, the behaviour of the line ratios shown in Fig. 3 (and re-

lated figures in the appendices) reveals that the ionisation of the eDIG is highly dependent on the distribution of H II regions in the disc (Sec. 3). The $[\text{N II}]/\text{H}\alpha$, $[\text{S II}]/\text{H}\alpha$, and $[\text{O III}]/\text{H}\beta$ ratios attain their highest values at the greatest distances from the mid-plane and in regions with lower $\Sigma_{\text{H}\alpha}$. This observation is incompatible with a smooth distribution of HOLMES throughout the thick disc and lower halo. Under the HOLMES scenario, higher $[\text{O III}]/\text{H}\beta$ ratios would be expected in the vicinities of the thick disc, along with a smooth distribution of characteristic high ionisation line ratios within the halos. Furthermore, the few high $[\text{O III}]/\text{H}\beta$ ratio bins near the galactic planes of the galaxies are clearly associated with SF regions within the discs, as indicated by the emission-line maps of eBETIS (see Fig. 2 and related figures in the appendices). Then, the behaviour of the $[\text{N II}]/\text{H}\alpha$, $[\text{S II}]/\text{H}\alpha$, and $[\text{O III}]/\text{H}\beta$ ratios alone is not sufficient evidence to conclusively support HOLMES as an ionisation source.

In addition, as explained in BETIS I, the conventional proxy employed to distinguish between star-forming regions, HOLMES, and mixed regimes—the $\text{H}\alpha$ equivalent width ($\text{EW}_{\text{H}\alpha}$)—may be unreliable. The $\text{EW}_{\text{H}\alpha}$ is a parameter that scales with the SFR per unit mass, namely the specific SFR (sSFR), and serves as a proxy for the stellar birthrate parameter b –Scalo, which is the ratio of the present to past-average SFR (Kennicutt et al. 1994; Kennicutt 1998). Observationally, the $\text{EW}_{\text{H}\alpha}$ is defined as the $\text{H}\alpha$ emission-line luminosity normalised to the adjacent continuum flux, effectively quantifying the SFR per unit luminosity (Kennicutt 1998). Given the relationship between $\text{EW}_{\text{H}\alpha}$ and surface mass density—a projection of the local mass-metallicity-EW relation (M - Z - $\text{EW}(\text{H}\alpha)$) (Rosales-Ortega et al. 2012)—low $\text{EW}_{\text{H}\alpha}$ values ~ 1 correspond to very high surface mass densities $\Sigma_{\text{Lum}} > 10^3 \text{ M}_{\odot} \text{ pc}^{-2}$, characteristic of early-type galaxies and the bulges of late-type galaxies. This corresponds precisely to the locus of the hDIG distribution at $\text{EW}_{\text{H}\alpha} \sim 1 \text{ \AA}$ (see Fig. 2 in Lacerda et al. 2018 and Fig. 9 in Lugo-Aranda et al. 2024).

In the low S/N regimes characteristic of the DIG, the low values of $\text{EW}_{\text{H}\alpha}$ employed to distinguish HOLMES from other regimes ($\text{EW}_{\text{H}\alpha} \sim 3 \text{ \AA}$) are highly contingent upon the stellar populations and the techniques utilised for SSP synthesis modelling (BETIS I). Moreover, as noted by (Tacchella et al. 2022), $\text{EW}_{\text{H}\alpha}$ is an inadequate tracer for discerning whether an $\text{H}\alpha$ photon has originated in dense gas (H II region) or diffuse gas (DIG region). Crucial considerations must be acknowledged, as the EW – a non-additive, ratio quantity – is calculated over binned sections along the line-of-sight of the halos of galaxies, which exhibit significantly different depths and properties.

4.3. Hybrid SF and shocks ionisation mechanism of the eDIG

The detection of high ionisation states in the galactic halo of the MW and several other galaxies, either in emission (e.g. O^{5+} ; Sembach & Savage 1992; Sembach et al. 2000) or absorption (e.g. O VI, N V, C IV; Jenkins & Meloy 1974; Pettini & West 1982; Hodges-Kluck & Bregman 2014; Hodges-Kluck et al. 2016), implies that interfaces between hot (10^6 K) and cooler ($\leq 10^4 \text{ K}$) gas are prevalent throughout the ISM at significant z distances from the galaxies’ midplanes. The gas at intermediate temperatures of $\sim 10^5 \text{ K}$ at these interfaces generates extreme ultraviolet (EUV) ionising radiation. The radiation of these hot-cool gas interfaces in the halo may constitute a significant source of ionising radiation for distant clouds and regions where LyC ionising radiation from OB stars in the midplane is either shielded or absent.

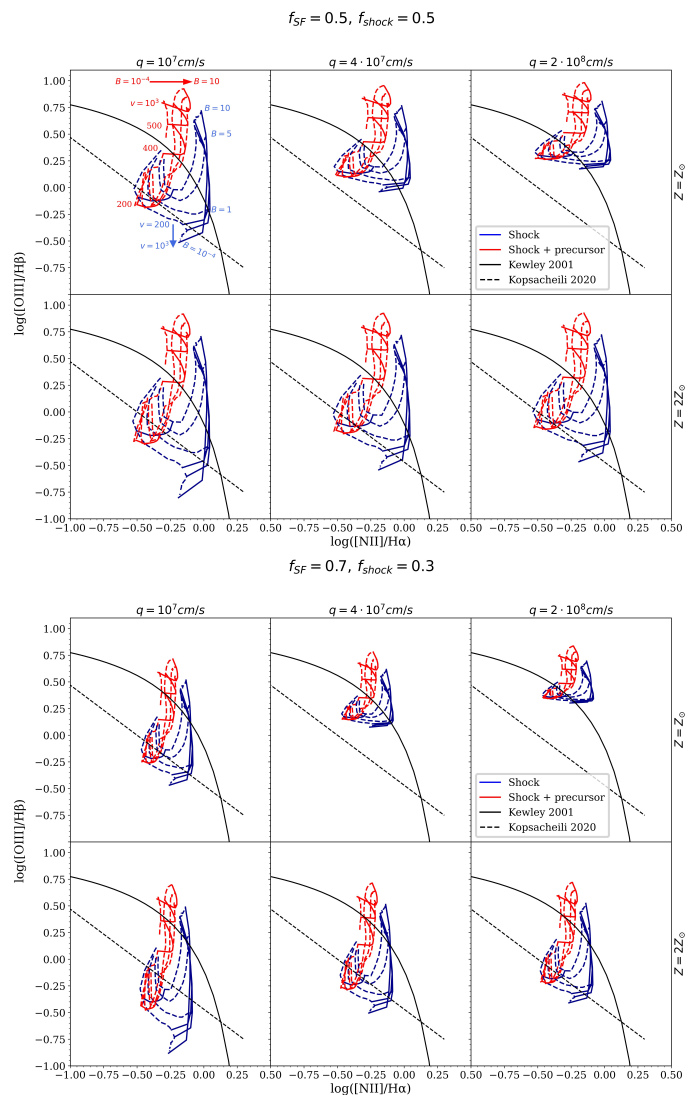


Fig. 6: Showcase of the star formation + fast shocks hybrid models for the $[\text{N II}]$ BPT. The upper panels correspond to the hybrid models with a contribution of fast shocks of 50% and 50% star formation. The lower panels correspond to 30% shocks and 70% star formation. The fast shocks models from Allen et al. (2008) used correspond to shock velocities from 200 to 1000 km/s and magnetic fields from 10^{-4} to 10 in units of $\mu\text{G}\cdot\text{cm}^{3/2}$, assuming shocks + a precursor (red curves) and only shocks (blue lines). The red arrow indicates the direction of increasing magnetic field in the shocks + precursor models, and blue arrow indicates the direction of increasing shock velocity in the shock only models. The dashed oblique line in the $[\text{N II}]/\text{H}\alpha$ diagnosis represent the separation of shock excited (e.g. supernova remnants) from photoionised regions (e.g. H II regions) from Kopsacheili et al. (2020). The classic demarcation between H II regions photoionisation and AGNs from Kewley et al. (2001) is also plotted in all diagnoses. Every panel represent the hybrid models for a fixed metallicity and ionisation parameter: first and second row correspond to $Z = Z_{\odot}$ and $Z = 2Z_{\odot}$, first, second and third column correspond to $q = 10^7$, $4 \cdot 10^7$ and $2 \cdot 10^8 \text{ cm/s}$ respectively.

Different types of interfaces have been proposed, each exhibiting distinct characteristics contingent on the physical processes and dynamical state of the boundary region between the hot and cooler gas. These include evaporative layers (e.g. Cowie

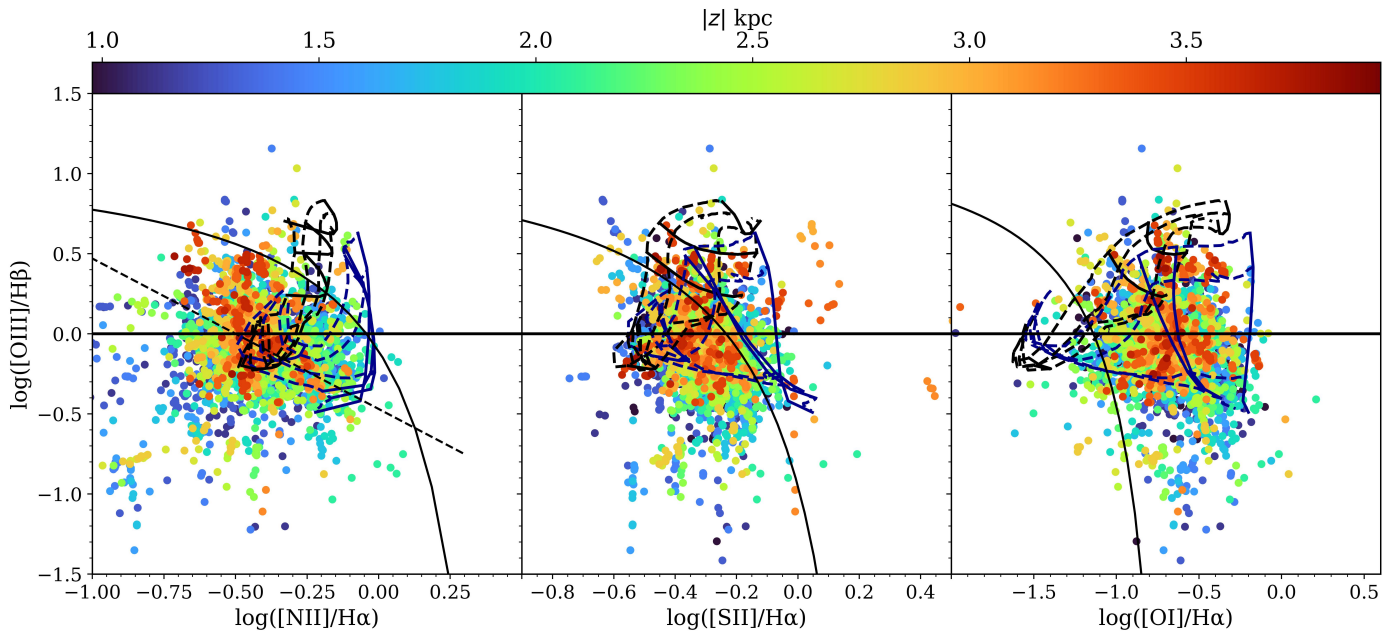


Fig. 7: BPT for all eDIG bins of IC1553, with the colours coding the vertical distance (both above and below) from the midplane. The plotted hybrid models correspond to a 40% of the flux due to fast shocks with pre-ionisation (curves lines) and with front shock only (blue curves), and with the 60% of the flux due to star formation with $Z = Z_{\odot}$ and $q = 10^7$ cm/s. Solid curves correspond to the shocks winds from 200 to 1000 km/s, and dashed curves represents magnetic field intensities from 0.0001 to $10 \mu\text{G}\cdot\text{cm}^{3/2}$. The Kopsacheili et al. (2020) and Kewley et al. (2001) lines are also plotted, as in Figure 6.

& McKee 1977), cooling-condensation fronts (Shapiro & Benjamin 1991), and turbulent mixing layers (TML, e.g. Begelman & Fabian 1990; Slavin et al. 1993; Rand 1998; Collins & Rand 2001; Binette et al. 2009). Slavin et al. (1993) proposed that self-photoionisation through EUV line emission of collisionally excited gas in mixing layers (with a temperature $\sim 10^{5.0-5.5}$ K) between hot ($\sim 10^6$ K) and cold (~ 100 K) gas can reproduce many optical/UV/EUV emission line ratios as observed in the DIG of several galaxies. However, theoretical models for TML are intricate and may lead to over-ionisation of the hot gas and under-ionisation of the cool gas, contingent on the specific details of the models (Haffner et al. 2009b).

Shocks induced in the ISM by feedback mechanisms, such as supersonic winds originating from high-level SF regions, have been proposed as a significant source of heating for the eDIG³ (Chevalier & Clegg 1985; Rand 1998; Collins & Rand 2001; Bland-Hawthorn et al. 2007). In this scenario, galactic winds are driven by the stellar winds and subsequent SNe of massive stars. These stellar winds create kpc-sized cavities in the ambient ISM on timescales of several million years (e.g. Mayya et al. 2023). Subsequently, these cavities are overrun by SN remnants (SNRs) from the most massive progenitor stars. Both processes occur at velocities exceeding the local sound speed, v_s , in the ISM, thereby generating strong shocks.

In an analogous way to TML, fast shocks induce comparable ionised conditions, characterised by an ionisation equilibrium between the hot and cold gas phases and slow mixing within the turbulent layer (Slavin et al. 1993; Rossa & Dettmar 2003b; Boettcher et al. 2019; Dirks et al. 2023). Given that shock heating is significant only if the kinetic energy is effi-

ciently thermalised, both photoionisation and shocks can be regarded as "thermal" heating sources of the ISM. Crucially, the observed rising trend in the [O III]/H β emission line ratio with height can be expected as a mixing sequence between the predominant shock ionisation in the halo and photoionisation in the disk. Shocks, therefore, emerge as the most promising secondary ionisation mechanism for the eDIG.

In star-forming galaxies, large-scale winds driven by bursts of star formation in the galactic plane create extended wind-driven filaments present in the halo (Sato et al. 2009; Ho et al. 2016). The ionisation of these wind-blown filamentary structures is primarily dominated by fast shocks. This is because the final stages of the wind evolution, driven by star formation, are marked by a flare-up that overshadows the main ionising source, such as the star formation activity of the H II regions observed in the midplane (Sharp & Bland-Hawthorn 2010). For the same reason, the contribution of fast shocks to the ionisation of the eDIG is also expected to be less significant near the galactic plane (Sharp & Bland-Hawthorn 2010; Ho et al. 2016).

The role of fast shocks as a potential alternative ionisation mechanism for the eDIG, as well as the impact of these filaments in the halo, has been studied by several authors (Rand 1998; Collins & Rand 2001; Levy et al. 2019; Dirks et al. 2023). For instance, Martin (1997) studied the excitation of the DIG in 14 star-forming dwarf galaxies and concluded that photoionisation due to star formation is the dominant mechanism. Shocks were only considered as a secondary ionisation source for gas with very low surface brightness. In this scenario, shocks could contribute up to 30-50% of the total ionisation budget.

As stated in the previous sections, the eBETIS sample presents diverse ionised structures in the halo, including filaments that extend more than 2 kpc from the midplane. Thus, we explore the combination of photoionisation from H II regions and ionisation due to fast shocks as simultaneous contributors to

³ Note that tidal interactions and AGN jets can also produce shock ionisation in the halos of galaxies, with similar effects as discussed in the text (e.g., Dopita & Sutherland 1995; Simpson et al. 2007; Rich et al. 2011; Ho et al. 2016; Molina et al. 2018).

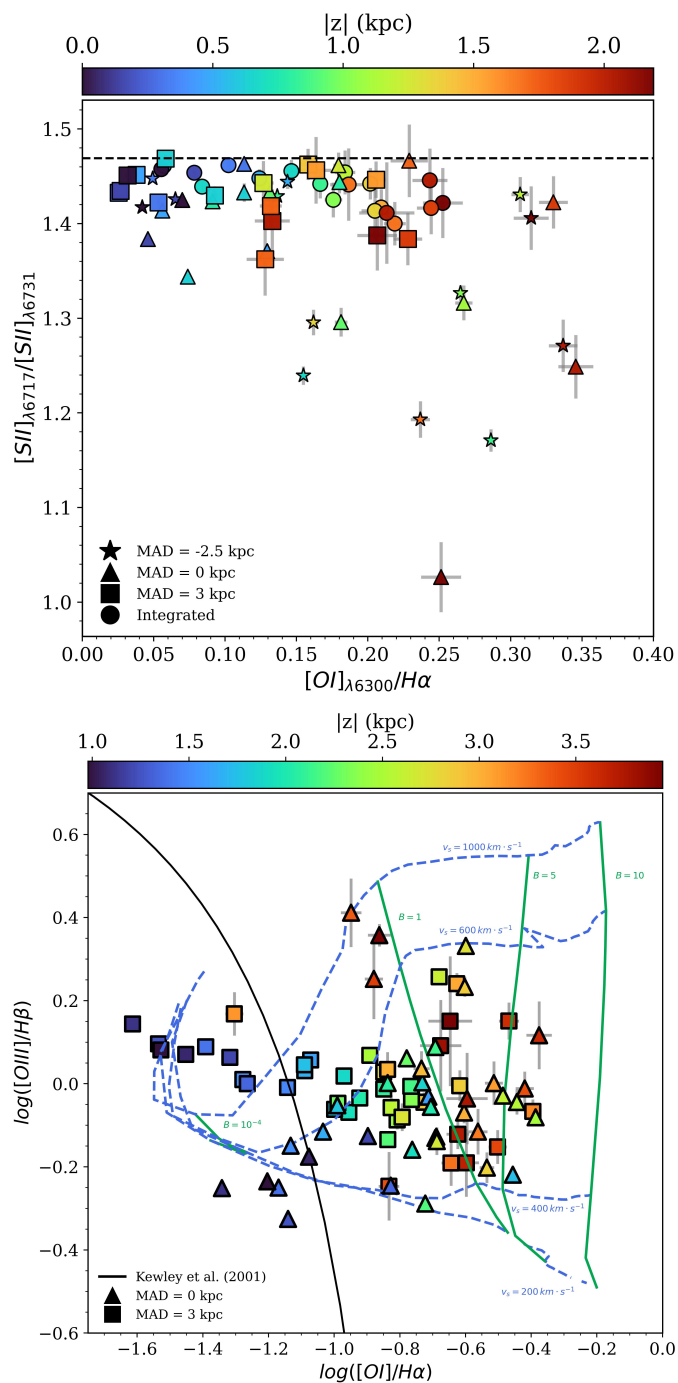


Fig. 8: Top: Electron density sensitive $[S II]_{\lambda 6717}/[S II]_{\lambda 6731}$ line ratio vs. shocks-proxy $[O I]_{\lambda 6300}/H\alpha$ line ratio for IC1553. Dashed horizontal line represents the theoretical low-density limit for the $[S II]$ doublet, corresponding to 1.469 (Osterbrock & Ferland 2006). Colours and symbols are similar to Figure 5. Bottom: $[O III]/H\beta$ vs. $[O I]/H\alpha$ diagnostic diagram for the bins of IC1553 at the minor-axis, centred in the biconical structure seen in the $[N II]/H\alpha$ map (triangles) and in the region between $2.5 < MAD < 4.5$ kpc (squares), coincident with the high-level SF region visible in the disk of the galaxy. Curves represent the hybrid model for 40% shocks (without precursor) and 60% star formation with $Z = Z_{\odot}$ and $q = 10^7$ cm/s. .

the ionisation mechanism of the eDIG. This is achieved by con-

structing a set of hybrid models that incorporate both star formation and fast shock mechanisms.

We firstly consider the photoionisation models for low-metallicity star-forming galaxies of Levesque et al. (2010). The grids of this models predict the line ratios involved in the typical BPT diagram (Baldwin et al. 1981) for a pure photoionisation regime due to the star formation with ionisation parameters (q) ranging from 10^7 to $2 \cdot 10^8$ cm/s and metallicities (Z) from 0.001 to 0.04. Each model grid is computed for electron densities n_e of $10, 10^2, 10^3$ and 10^4 cm $^{-3}$, assuming either continuous star formation or an instantaneous burst of star formation at 0 Myr.

On the other hand, we consider the fast shocks models of Allen et al. (2008). This models predict the flux of the ionising radiation produced by a shock. The flux is dependent on the shock velocity ($f \propto v_s^3$). Therefore, if the shock velocity surpasses the velocity of the photoionisation front (in the case of a low ionisation parameter), the ionising photons are absorbed by the surrounding gas, altering its ionisation state. In another scenario, if $v_s \approx 170$ km/s, the ionisation front velocity now exceed the velocity of the shock, pre-ionising the surrounding gas and changing the optical emission lines observed (McKee & Hollenbach 1980). The fast shocks models of Allen et al. (2008) consider this two scenarios, with preshock densities ranging from 0.01 to 1000 cm $^{-3}$, shock velocities from 100 to 1000 km/s and magnetic field ($B/n^{1/2}$) from 10^{-4} to $100 \mu\text{G}\cdot\text{cm}^{3/2}$.

Our hybrid models are constructed as follows: we consider both shock models, with and without assuming pre-ionisation. Then, for each shock model, we assume that the predicted flux corresponding to shock wind velocity of 200, 400, 500 and 1000 km/s and magnetic field of $10^{-4}, 1.0, 5.0$ and $10 \mu\text{G}\cdot\text{cm}^{3/2}$ contributes only a fraction $f_{shock} \in [0, 1]$ of the total observed ionising flux. The remaining fraction $1 - f_{shock}$ corresponds to the flux predicted by a grid model with a certain ionisation parameter and metallicity from Levesque et al. (2010).

Figure 6 shows an example of hybrid models for the $[N II]/H\alpha$ BPT, with $Z = Z_{\odot}$ and $2Z_{\odot}$, $q = 10^7, 4 \cdot 10^7$ and $2 \cdot 10^8$ cm/s, and $f_{shock} = 0.5$ and 0.3 . It shows that decreasing f_{shock} shifts the models towards the OB-stars regime, as defined by the Kewley et al. (2001) curve, indicating that photoionisation by star formation becomes more significant in the hybrid models. Additionally, increasing the ionisation parameter in the models tends to flatten them vertically, resulting in higher predicted values for the high excitation $[O III]/H\beta$ ratio. Besides, increasing the metallicity tends to expand the models, predicting a wider range of both $[O III]/H\beta$ and $[N II]/H\alpha$ ratios.

For instance, Figure 7 shows the BPT diagram for all the eDIG bins for IC1553⁴. The models plotted represent the predicted fluxes for a combination of fast shocks with pre-ionisation (black curve lines) and with front shock only (blue curve lines) weighted with $f_{shock} = 0.4$, plus a photoionisation model correspondent to $Z = Z_{\odot}$ and $q = 10^7$ cm/s.

⁴ Note that these results do not concur with the diagnosis of Rautio et al. (2022) for this galaxy, whose BPT diagrams are predominantly populated within the star formation regime. However, they align more closely with the subsequent study by Dirks et al. (2023). The locus in all three panels of the BPT diagram corresponds with the findings of this latter study, being proximate to the Kewley et al. (2001) line for $[S II]/H\alpha$, and achieving values up to 0 (in log scale) for $[O I]/H\alpha$. Nevertheless, in comparison to both studies, we observe a greater number of data points in the high excitation regimes for $[S II]/H\alpha$ and $[O I]/H\alpha$, corresponding to bins at larger distances. We attribute this to our enhanced adaptive binning method, which enables sampling data with $S/N > 2$ at greater distances, and to our exclusion of bins situated within the galactic plane, as discussed in section 3.

at 0 Myr and $n_e = 100 \text{ cm}^{-3}$. Thus, the fluxes predicted for this particular hybrid models has the form: $F_{\text{hyb}} = 0.4F_{\text{shock}} + 0.6F_{\text{SF}}(n_e, q, Z)$. Solid curves correspond to the shocks winds from 200 to 1000 km/s, and dashed curves represents magnetic field intensities from 0.0001 to $10 \mu\text{G}\cdot\text{cm}^{3/2}$. The parameters were selected to best fit the points in the BPT diagram, particularly the [S II]/H α and [O I]/H α diagnostics, as they are more sensitive to changes in ionisation regimes. The points in the [S II]/H α and [O I]/H α diagnostics tend to deviate more from photoionisation models than the [N II]/H α diagnostic if an additional source of ionisation, such as AGN or fast shocks, is present (Dirks et al. 2023). The f_{shock} for fitting each BPT was determined by performing several trials with different f_{shock} , selecting the one that best fits the data points in the [S II]/H α and [O I]/H α diagnostics.

The presence of shocks in the eDIG is further indicated by the asymmetric increase of [O I]/H α with respect to height, as illustrated in Fig. 3 for IC1553 (and in the corresponding figures in the appendices for the entire eBETIS sample). Given that neutral O and H are coupled via charge-exchange reactions, the observed increase in [O I]/H α suggests a multiphase medium, characteristic of shock-compressed regions (Collins & Rand 2001; Boettcher et al. 2019).

The top-panel of Figure 8 shows the observed [S II] $_{\lambda 6717}$ /[S II] $_{\lambda 6731}$ doublet ratio versus the [O I] $_{\lambda 6300}$ /H α line ratio for various binned sections in the halo of IC1553 at different galactocentric distances. The [S II] doublet is employed to infer the electron gas density; this ratio diminishes as the electron gas density increases, with a low-density limit of approximately 1.5, corresponding to an electron density of $n_e \leq 10 \text{ cm}^{-3}$ (Osterbrock & Ferland 2006). Most of the eDIG regions near the midplane of IC1553 exhibit [S II] line ratios close to this low-density limit, accompanied by low [O I]/H α values, indicative of H II region emission. However, for bins corresponding to a higher altitude $|z|$ from the midplane, the [S II] $_{\lambda 6717}$ /[S II] $_{\lambda 6731}$ ratio decreases to values between 1.0 and 1.3, implying high electron densities in the range of $n_e \sim 200 - 800 \text{ cm}^{-3}$.

The most striking feature of this figure is that the regions with low [S II] doublet ratios coincide with regions exhibiting high [O I]/H α values (> 0.25), indicative of shock-compressed ionised gas. Therefore, the low doublet [S II] ratios, their implied high gas density, and the fact that these regions exhibit higher [O I]/H α values are consistent with a scenario wherein gas emission originates from shocks, likely induced by feedback from high-level SF regions within the galactic disk. In this scenario, fast shocks can account for the increase in the [O I]/H α ratio with distance from the midplane, with the highest [O I]/H α ratios corresponding to the shocked interface at the greatest distances from the midplane (this is also seen in the equivalent figures for the rest of the galaxies in the appendices). This picture can be further validated by comparing the high-density, high [O I]/H α bins values of IC1553 to the hybrid SF-shocks models in the [O III]/H β vs. [O I]/H α diagnostic diagram shown in the bottom panel of Figure 8. The triangles correspond to integrated bins of IC1553 at the minor-axis (MAD = 0 kpc, centred in the biconical structure seen in the [N II]/H α map) and the squares to bins at $2.5 < \text{MAD} < 4.5$ kpc, centred at the high-level SF region visible in the disk of the galaxy in H α . The curves represent a hybrid model with a 60% star-formation and 40% shock contribution (without precursor), with $Z = Z_{\odot}$ and $q = 10^7 \text{ cm/s}$. The parameter space of this specific hybrid model aligns precisely with the locus of the eDIG bins, corresponding to fast shocks between 400 and 600 km s^{-1} and magnetic field

values in the range $B = 10^{-4} - 5$, regardless of the MAD distance and the diverse ionisation conditions observed in the halo in those regions.

These results align with recent numerical simulations of the DIG: Weber et al. (2019b) calculated the ionisation structure within the DIG, providing quantitative predictions for diagnostic optical emission lines using advanced 3D non-LTE radiative transfer simulations. These simulations assume ionisation by a matter-bounded stellar population SED, based on a plausible parameter space for the ionising sources (T_{eff}, Z), while considering varying escape fractions f_{esc} and clumpiness of the DIG. The findings support the scenario where the DIG is primarily ionised by (filtered) radiation from hot stars within the galactic plane. Consequently, photoionisation heating results in higher temperatures in the DIG compared to H II regions, leading to stronger emissions of collisionally excited optical lines such as [N II], [O I], [O III], or [S II]. However, these models do not account for the increasing [O III]/H β ratio at greater distances from the galactic plane, indicating the need for an additional ionising source. In our proposed SF-shock hybrid model, SF photoionisation is identified as the principal ionisation mechanism for the eDIG, while incorporating shock heating and collisional excitation as supplementary heating processes responsible for the observed increases in the [O III]/H β and [O I]/H α ratios.

In summary, the ionisation of the eDIG is evidently not a phenomenon that can be elucidated by a single mechanism; rather, a multitude of mechanisms is necessary to fully comprehend the nature of the ionisation of extraplanar gas. Additionally, the ionisation mechanisms vary in significance across different galaxies. The prevailing consensus is that photoionisation predominantly governs the excitation of the eDIG, with shocks being considered a secondary source of ionisation. The spatial variation of line ratios, along with their absolute values, suggests the presence of shock excitation. Consequently, a model incorporating star-forming ionisation with shock ionisation as an additional heating source offers the most satisfactory explanation for the relatively high [O I]/H α and [O III]/H β ratios observed in the lowest surface brightness regions as a function of distance from the midplane in edge-on star-forming galaxies.

5. Results

5.1. The radial variation of shocks contribution and the biconical structure of IC1553

The integration of emission-line ratio maps with hybrid SF+shock models for the eDIG facilitates a comprehensive analysis of the ionisation conditions within targeted regions of specific galaxies. In the case of IC1553, illustrated in the upper-right panel of Figure 2, there exists a distinct axisymmetric region with elevated [N II]/H α ratios between $-0.5 \text{ kpc} < \text{MAD} < 0.5 \text{ kpc}$, centred on the galaxy's minor axis (MAD = 0). This enhanced region forms an apparent biconical structure that appears to emanate from the disk, extending to significant heights above and below the midplane $|z| \sim 3.5 \text{ kpc}$ in both the upper and lower halo of IC1553. This phenomenon is also visible in the [S II]/[N II] map, as depicted in Figure 9.

This structure was also identified by previous authors (Rautio et al. 2022; Dirks et al. 2023), who suggested that its origin could be attributed to a large off-centred galactic outflow or superbubble. (Rautio et al. 2022) described this feature as a biconical region of OB-shock ionisation caused by significant bidirectional outflows associated with superbubbles that have breached the disk. However, since there are no corresponding H α emission

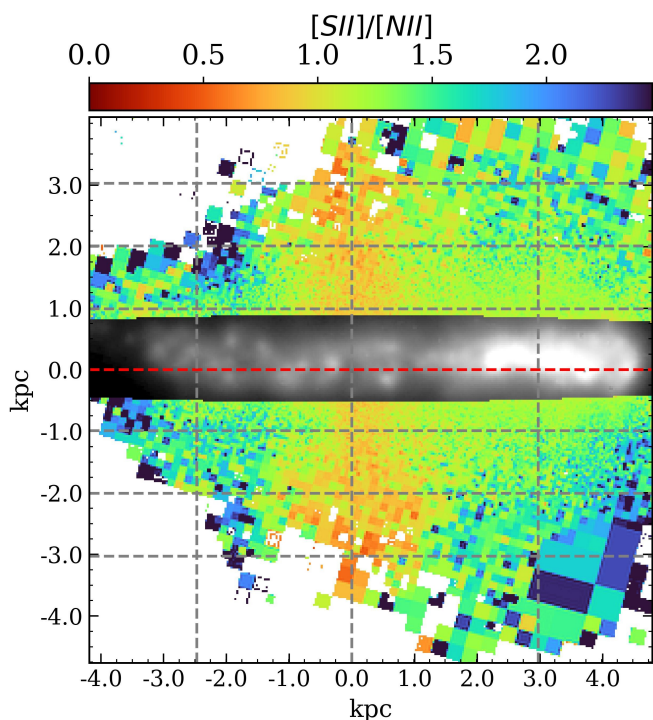


Fig. 9: $[\text{S II}]_{\lambda 6717}/[\text{N II}]_{\lambda 6584}$ emission line map for IC1553. Vertical and horizontal lines represented as in Figure 2.

enhancements in either the disk or the halo at the same spatial position as the biconical structure, they argue that the absence of a visible starburst responsible for the outflow is due to the starburst having quenched 20 Myr ago, or more. Dirks et al. (2023) support the biconical outflow scenario through indirect evidence based on $\text{H}\alpha$ FWHM, which is sensitive to the velocity of gas flows in the presence of shocks. Nevertheless, the enhancement in $\text{H}\alpha$ FWHM identified by Dirks et al. (2023) (see their figure 10) does not morphologically coincide with the $[\text{N II}]/\text{H}\alpha$ or $[\text{S II}]/[\text{N II}]$ structure observed in IC1553.

To elucidate the origin of this structure, we can examine the morphological information provided by the emission-line maps of IC1553, as presented in Figures 1 and 2. Firstly, as previously discussed, the distribution of H II regions in the galactic plane directly influences the morphology and ionisation conditions of the eDIG. The $\text{H}\alpha$ map of IC1553 shows no evidence of a structure, outflow, or filaments extending from the galactic disk centred on or near the minor axis of the galaxy. Indeed, the strongest emission is observed at the boundaries of the high-level SF regions in the southern part of the galaxy, extending radially within a MAD range of 1.5 to 4.5 kpc, and vertically up to ≥ 3 kpc.

Secondly, while the structure in the $[\text{N II}]/\text{H}\alpha$ emission-line map appears to symmetrically originate from the disk at the galaxy’s minor axis ($\text{MAD} \approx 0$ kpc), the $[\text{S II}]/\text{H}\alpha$ map reveals a less defined biconical structure with a discernible offset at $\text{MAD} \sim -1.2$ kpc. This same structure is observed in the $[\text{S II}]/[\text{N II}]$ map, but with an opposite offset at $\text{MAD} \sim 0.2$ kpc. Additionally, the upper part of the $[\text{O I}]/\text{H}\alpha$ map hints at this structure, displaying an offset at $\text{MAD} \sim -1.4$ kpc relative to $[\text{N II}]/\text{H}\alpha$. Most strikingly, the $[\text{O III}]/\text{H}\beta$ line-ratio map reveals no such structure on either side of the midplane. The high $[\text{O III}]/\text{H}\beta$ emission relative to H is a key observational feature of galactic outflows, regardless of whether its origin is due to SF (e.g. Tenorio-Tagle & Bodenheimer 1988; Norman & Ikeuchi

1989) or AGNs (e.g. López-Cobá et al. 2020; González-Díaz et al. 2024). The $[\text{O III}]/\text{H}\beta$ map of IC1553 exhibits the typical increase of the ratio with distance from the midplane in a homogeneous manner, independent of radial distance, but without any characteristic signature of an outflow at $\text{MAD} \sim 0$. Therefore, based on the information provided by the 2D distribution of the eDIG, there is no morphological congruence among the different emission-line maps to definitively confirm the existence of an outflow in IC1553.

The $[\text{S II}]/[\text{N II}]$ map can also elucidate the origin of this structure. Given the similar ionisation potentials of $[\text{S II}]$ and $[\text{N II}]$ (10.4 eV and 14.5 eV, respectively), $[\text{S II}]/[\text{N II}]$ is largely independent of electron temperature. Consequently, variations in $[\text{S II}]/[\text{N II}]$ imply changes in local ionisation conditions or metallicity (since nitrogen is a secondary nucleosynthetic product while sulphur is a primary product) but primarily reflect variations in S^+/S (Haffner et al. 2009b). In a photoionisation model, $[\text{S II}]/[\text{N II}]$ is expected to increase with distance from the ionising source, aligning qualitatively with a smooth transition from predominantly doubly ionised to singly ionised states ($\text{S}^{++} \rightarrow \text{S}^+$), as expected in dilute photoionisation models (e.g. low ionisation parameters, q , Domgorgen & Mathis 1994). The consistency of $[\text{S II}]/[\text{N II}]$ suggests an additional heating source (Reynolds & Cox 1992; Rand 1998; Reynolds et al. 1999; Collins & Rand 2001), which in our model would be provided by shocks. Indeed, in the Allen et al. (2008) models, shocks naturally produce a lower $[\text{N II}]$ flux relative to $[\text{S II}]$ compared to photoionisation. In IC1553, we observe a symmetrical increase in the $[\text{S II}]/[\text{N II}]$ ratio across all galactocentric distances, from values of approximately 1.2 near the galactic disk, up to values ≥ 2 , except in the region associated with the biconical structure at a MAD of approximately 0.2 where $[\text{S II}]/[\text{N II}]$ remains nearly constant at around 0.9 but decreases with height to values around 0.5. An increase in the $[\text{S II}]/[\text{N II}]$ ratio with height has also been observed at two slit positions perpendicular to the edge-on galaxy NGC 5775 (Boettcher et al. 2019). The overall scenario depicted by the $[\text{S II}]/[\text{N II}]$ ratio map suggests that sulphur and nitrogen are ionised by a photoionisation field that diminishes with height, yet with localised deficits or enhancements of either $[\text{S II}]$ or $[\text{N II}]$, indicating local changes in ionisation conditions within the complex eDIG halo, likely due to shocks.

To further explain the structures observed in IC1553, we can apply hybrid SF-shock models as previously described. Figure 10 depicts the same BPT diagram as in Figure 7, but limited to the bins of the biconical structure identified in the $[\text{N II}]/\text{H}\alpha$ map. Specifically, it shows bins between -0.5 kpc $<$ MAD $<$ 0.5 kpc (top) and bins between 2.5 kpc $<$ MAD $<$ 3.5 kpc (bottom), corresponding radially to the regions above and below the bright SF regions near the southern edge of the disk. In these latter regions, outside the biconical structure, the hybrid models that best fit the data indicate 80% of the ionisation is due to star formation and 20% to shocks. For regions within the biconical structures, at $\text{MAD} \sim 0$ kpc, the contribution from star formation decreases, with shocks becoming relatively more significant (increasing from 20% to 40%). Hence, while the contribution of shocks within the biconical structure is augmented, the increase is modest; SF remains the predominant source of ionisation, and the emission-line ratios do not exhibit the high $[\text{O III}]/\text{H}\beta$ values characteristic of a galactic outflow.

The absence of distinct filamentary, outflow-like structures in both the $\text{H}\alpha$ flux and the $[\text{O III}]/\text{H}\beta$ emission-line ratio maps, the observed offsets, and the conflicting morphology between the $[\text{N II}]/\text{H}\alpha$, $[\text{O I}]/\text{H}\alpha$, and $[\text{S II}]/[\text{N II}]$ ratios, combined with the lack of direct spatial correlation between the biconical struc-

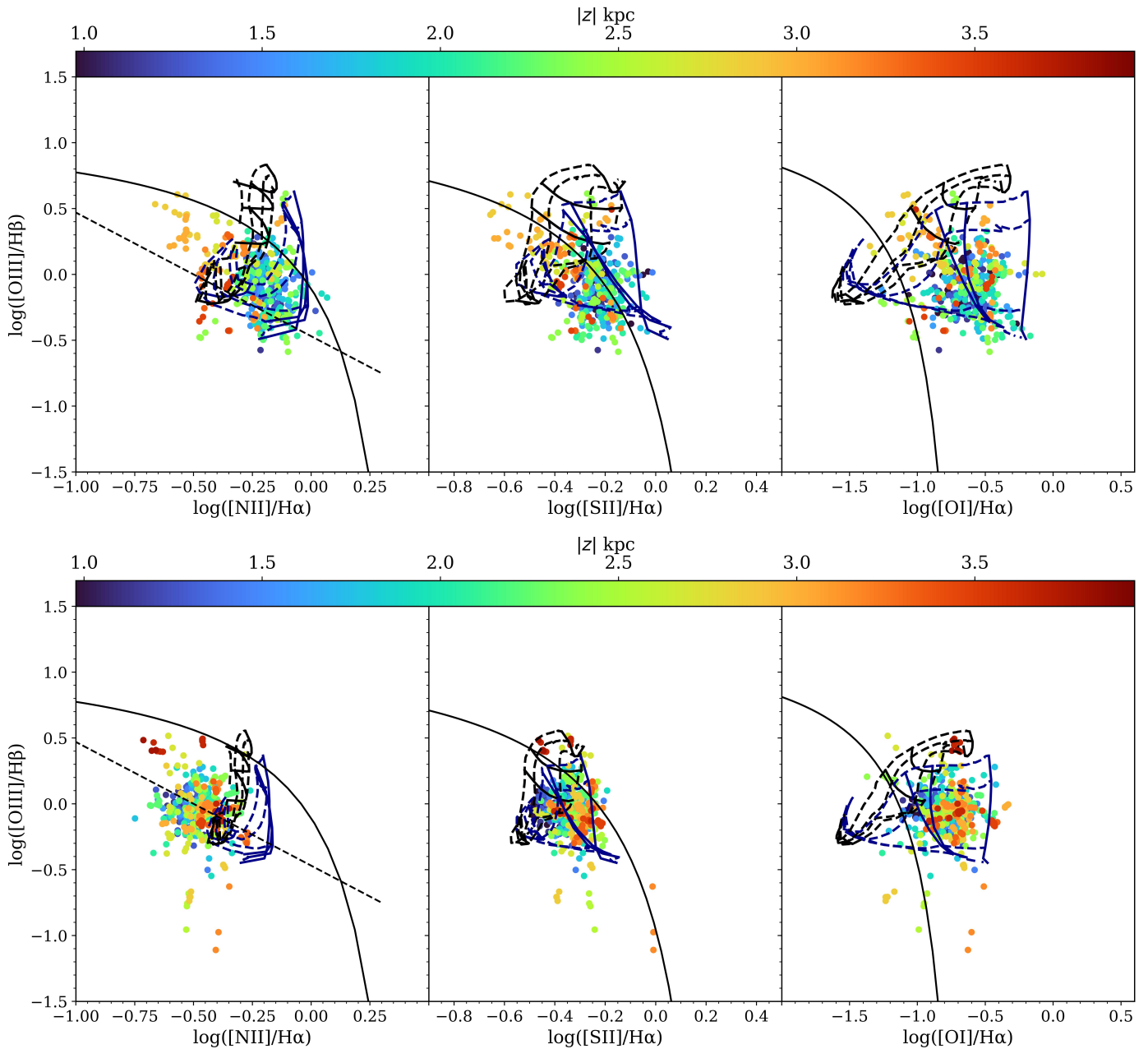


Fig. 10: IC1553 BPT with hybrid models, similar to Figure 7. Top: eDIG bins corresponding to the biconical structure seen in the $[\text{N II}]/\text{H}\alpha$ map, between $-0.5 \text{ kpc} < \text{MAD} < 0.5 \text{ kpc}$. The hybrid models that best fit the data correspond to 40% shocks and 60% SF with $Z = Z_{\odot}$ and $q = 10^7 \text{ cm/s}$. Bottom: eDIG bins corresponding to the high-SF feature on southern edge of the disk, between $2.5 \text{ kpc} < \text{MAD} < 3.5 \text{ kpc}$. The hybrid models that best fit the data correspond to 20% shocks and 80% SF with $Z = Z_{\odot}$ and $q = 10^7 \text{ cm/s}$.

ture and any potential ionisation sources within the disk, and the evidence indicating that the primary ionisation within the structure is attributed to SF photoionisation, suggest an alternative interpretation for the biconical structure observed in the $[\text{N II}]/\text{H}\alpha$ ratio map. As discussed throughout this paper, the nature and morphology of the eDIG are directly influenced by the local level of SF within the disk, which drives the feedback mechanisms responsible for ionising the gas in the surrounding vicinity.

From the $\text{H}\alpha$ flux map of IC1553, the high-level star-forming (SF) regions at a MAD between 2 and 4 kpc appear to be very near the edge of the galaxy's disk. Consequently, the halo

line-of-sight line ratios in the vicinity of these regions resemble those of H II regions (e.g., $[\text{N II}]/\text{H}\alpha \leq 0.4$). This effect is more pronounced in the $[\text{O III}]/\text{H}\beta$ and $[\text{O I}]/\text{H}\alpha$ maps, where high $[\text{O III}]/\text{H}\beta$ values (≥ 1.5) and low $[\text{O I}]/\text{H}\alpha$ values (≤ 0.1) are observed immediately above and below the bright H II regions on the plane at $2 < \text{MAD} < 4 \text{ kpc}$. A common observational challenge in edge-on galaxies is the invisibility of individual SF regions in the optical spectrum due to the high optical depth for both blue continuum and $\text{H}\alpha$ line emission. This likely occurs at $\text{MAD} \geq -2 \text{ kpc}$, where no bright H II regions are visible on the galaxy disk in the $\text{H}\alpha$ flux map. Nevertheless, the $[\text{N II}]/\text{H}\alpha$, $[\text{S II}]/\text{H}\alpha$, $[\text{O I}]/\text{H}\alpha$, and $[\text{O III}]/\text{H}\beta$ line ratios above and below

Table 2: Summary of characteristics of the eDIG.

galaxy	DIG morphology	MAD, z (kpc)
IC217	Disc: Homogeneous distribution of bright H II regions Halo: Thin eDIG layer, low S/N	6, 2
PGC28308	Disc: Homogeneous distribution of bright H II regions Halo: Extended and homogeneous eDIG	8, 2
PGC30591	Disc: Few bright H II regions Halo: Inhomogeneous extended eDIG	4, 2
ESO544-27	Disc: Homogeneous distribution of bright H II regions Halo: Homogeneous eDIG and extended filaments	4, 2
IC1553	Disc: Inhomogeneous distribution of H II regions with respect the line of sight, hidden H II regions Halo: Highly asymmetrical eDIG structure with a bicone and extended filaments	4, 3.5
ESO443-21	Disc: Homogeneous distribution of bright H II regions Halo: Extended eDIG with a large filamentary knot	8, 5
ESO469-15	Disc: Bright emission around the centre Halo: Several extraplanar H II regions, mixed eDIG regimes	3, 2
ESO157-49	Disc: Homogeneous distribution of bright H II regions Halo: Tilted and mixed eDIG regimes with extended filaments	4, 2.5

Notes. The second column represents the DIG morphology observed in the disc and halo from the $H\alpha$ images. The third column shows the horizontal and vertical distances covered by the eDIG.

the galaxy plane in this galactocentric range resemble those near the bright H II regions at $MAD > 2$ kpc. At the minor axis ($MAD = 0$ kpc), the galaxy disk is expected to show a lower average star formation rate (SFR) along the line-of-sight due to the presence of the galaxy's bulge, compared to the rest of the galaxy disk. Consequently, the line emission strength near the galaxy's centre would be dominated by the strong emission from the bright visible H II regions to the south of the galaxy ($2 < MAD < 4$ kpc) and by obscured H II regions on the galaxy disks at projected distances $-1 < MAD < -4$ kpc.

In this scenario, the biconical structure observed in $[N II]/H\alpha$ could be an optical artefact, arising from high typical $[N II]/H\alpha$ eDIG background values (≥ 0.5) due to the overall feedback processes in the galaxy disk (SF+shocks), and low $[N II]/H\alpha$ values (≤ 0.4) from the bright and obscured H II regions near the minor axis of the galaxy. This results in H II region-like emission in the vicinity of the galactic plane. This scenario is more evident in the $[S II]/H\alpha$ and $[O I]/H\alpha$ maps, where the background emission clearly permeates the halo with typical eDIG values, and the strong emission from the adjacent H II regions is seen in projection, exhibiting typical H II region values. This interpretation accounts for the offset of the biconical structure between the $[N II]/H\alpha$ and $[S II]/H\alpha$ maps, as S and N present similar but distinct ionisation potentials, shedding light on the structure of the $[S II]/[N II]$ line-ratio map. It also explains the absence of filaments or outflow features in both the $H\alpha$ flux and $[O III]/H\beta$ line-ratio maps.

In the case of the biconical structure of IC1553, it becomes evident that results obtained from the global analysis of a galaxy should not be generalised. Limiting the analysis to specific regions reveals that the ionisation mechanisms present in the eDIG can vary. This finding aligns with our observations in **BETIS I**: a group of galaxies exhibiting diverse physical processes can lead to misleading conclusions about the ionisation mechanisms of the DIG. Furthermore, even within a single galaxy, when the resolution is sufficiently high, a global (BPT) analysis of the eDIG can still be misleading, as it encompasses regions of the galaxy that display distinct physical processes and ionisation conditions.

5.2. General results for the eBETIS sample

In this section, we summarise the results of the previous analysis for all the galaxies in the sample. The rest of emission line maps, plots and further details of each galaxy can be found in the appendices from A to H.

In general, the linkage between the star formation activity in the disk and the ionisation of the eDIG is evident in all galaxies. The entire sample shows the same tendencies, with the $\Sigma_{H\alpha}$ distribution in the plane and the line ratios distribution being anti-correlated. Additionally, the increase in T_e with distance from the midplane and the increase in S^+/S at those MADs corresponding to lower $\Sigma_{H\alpha}$ in the midplane are also general behaviours in the sample. However, each galaxy can present differences in the ionisation structure of the eDIG due to the presence of morphological structures in the halo or asymmetries in the disc. This can cause the contribution of fast shocks to the ionisation budget of the eDIG to vary in different zones of the halo.

- PGC28308: The bidimensional structure of the eDIG is shown as a shift between the $[N II]/H\alpha$ and $[S II]/H\alpha$ MAD distributions at $z = 1.5$ and 2.5 kpc. In general, the ionisation regimes in the halo are mixed, with contributions of approximately 50% from fast shocks and 50% from the star formation.
- PGC30591: The bidimensional structure of the eDIG is more pronounced in comparison with PGC28308, with a clearer shift between the MAD distributions at $z = 0.7$ and 1.5 kpc. Fast shocks contribute a 40% to the ionisation budget. Furthermore, since the ionisation regimes are not that mixed in comparison with other galaxies, the dependence of these regimes on height is more evident in the BPT diagrams. Bins further from the plane tend to be closer to the fast shock regime in the BPT, coinciding with the increment of T_e in height.
- ESO544-27: This galaxy presents a homogeneous distribution of H II regions with respect to the line of sight, and the $\Sigma_{H\alpha}$ distribution does not show strong asymmetries along the major axis. This homogeneity is reflected in the eDIG as well. The increase in T_e with distance from the midplane

is linear and uniform, with a constant $S^+/S \sim 0.5$. Additionally, the contribution of fast shocks to the ionisation budget is 50%.

- ESO443-21: This galaxy presents a broad knot-shape filamentous structure at a distance of 1.5 kpc, extending up to a height of 4.5 kpc within the range of $-1 \text{ kpc} < \text{MAD} < 2.5 \text{ kpc}$. The presence of this knot adds an additional 10% to the star formation contribution for the ionisation budget of the eDIG, resulting in a 20% contribution of fast shocks to the ionisation of the eDIG for $z > 0$ and 30% for $z < 0$.
- ESO469-15: The presence of extraplanar H II regions in its halo affects the overall ionisation structure of the eDIG. The line ratios reach lower values compared to the rest of the galaxies, as well as the T_e , ranging between $6\text{-}8 \cdot 10^3 \text{ K}$. The contribution of fast shocks is only 30% throughout the eDIG.
- ESO157-49: The galaxy shows an asymmetry in the eDIG between $z > 0$ and $z < 0$, being the emission significantly uniform at $z > 0$ and presenting a tilted and shifted ionisation structures at $z < 0$, probably due to the influence of its nearby neighbours. In general, the contribution of fast shocks in the ionisation of the eDIG is 50%, however, it drops to 30% between $2 \text{ kpc} < \text{MAD} < 3 \text{ kpc}$, where the $\Sigma_{H\alpha}$ is higher. In this latter case, it is clear that bins further from the plane tend to be closer to the fast shock regime in the BPT, coinciding with the increment of T_e in height.
- IC217: The low data sampling due to poor data quality does not allow for a more in-depth analysis of this galaxy. It exhibits the general characteristics of the rest of the sample described above, with an overall contribution of fast shocks of 50%.

The general characteristics of the eDIG found in the eBETIS sample are summarised in table 2.

6. Summary and conclusions

In this work, we present the second part of the Bidimensional Exploration of the warm-Temperature Ionised gaS (BETIS) project, focusing on the spatially resolved and spectral study of the extraplanar diffuse ionised gas (eDIG) in a selection of eight edge-on ($i > 75^\circ$) nearby galaxies. We used the galaxies from the Com19 dataset as our sample and applied the methodology described in BETIS I for adaptively binning the observed datacubes and extracting the binned emission line maps from them.

The $H\alpha$ emission line maps reveal a complex ionisation structure in the galactic halos composed by diverse structures as filaments or knots that can reach more than 3 kpc from the midplane. The real complexity of the ionisation structure of the eDIG is shown when examining the $[\text{N II}]/H\alpha$, $[\text{S II}]/H\alpha$, $[\text{O III}]/H\beta$ and $[\text{O I}]/H\alpha$ maps, revealing the presence of new structures as an apparent biconical structure in IC1553 or a broad ionised knot of ESO443-21. The behaviour of these line ratios reveals that the ionisation structure of the eDIG is shown to be influenced by the distribution of H II regions in the galactic plane as seen from the line of sight. In all galaxies, the line ratios increase both vertically and radially, showing an anti-correlation with the $\Sigma_{H\alpha}$ distribution of the galactic disc. These ratios reach higher values at distances further from the H II regions, both in terms of height (z) and major axis distance (MAD).

This correlation between the morphological distribution of star-forming regions in the disks and the morphology of the halos presents the strongest evidence supporting the interpretation that energy sources from star formation within the galaxy disks drive the observed disk-halo interaction, being the Ly α photons

leaking from OB associations the main ionisation source of the eDIG.

However, OB-star-driven ionisation can not explain some features found in the eDIG, such as the enhanced $[\text{N II}]/H\alpha$ and $[\text{S II}]/H\alpha$ and the presence of high ionisation species such as $[\text{O III}]$ at higher distances from the midplane. From the $[\text{N II}]/H\alpha$ and $[\text{S II}]/H\alpha$ ratios we explored the radial and vertical variations of T_e and S^+/S . The general behaviour indicates a linear, constant increment of T_e with increasing distance from the galactic plane for all the galaxies. Besides, there is significant variations in T_e and S^+/S at different MADs, also linked to the H II regions distribution with respect the line of sight. The variations in temperature and ionisation structure of the eDIG as a function of spatial position within a single galaxy provide compelling evidence of the intricate dynamical heating structure of the ISM in the halo. These variations show that the eDIG tends towards a lower ionisation state (higher S^+/S) compared to classical H II regions. The anomalous $[\text{N II}]/H\alpha$ and $[\text{S II}]/H\alpha$ line ratios in the eDIG can be attributed to an increase in the T_e temperature in the halo, resulting from photoionisation with a lower ionisation parameter.

To account for the $[\text{O III}]/H\beta$ and $[\text{O I}]/H\alpha$ ratios, various ionisation mechanisms have been considered. One such mechanism, recently highlighted in the literature, involves photoionisation by a hard spectrum emanating from the high-temperature end of the white dwarf distribution and the central stars of planetary nebulae; the low-mass, hot, and evolved (post-AGB) stars known as HOLMES. Nevertheless, the correlation between the ionisation structure of the eDIG and the H II regions distribution observed in this study does not support a homogeneous distribution of HOLMES across the thick disc and lower halo. This inconsistency, combined with the unreliability of $\text{EW}_{H\alpha}$ as a proxy commonly used in the literature to differentiate star-forming regions from HOLMES, effectively negates HOLMES as a plausible ionisation mechanism for the eDIG. Consequently, the behaviour of the $[\text{N II}]/H\alpha$, $[\text{S II}]/H\alpha$, and $[\text{O III}]/H\beta$ ratios alone is not sufficient evidence to conclusively support HOLMES as an ionisation source. These behaviours should be carefully used in the analysis of the ionisation mechanisms of the (e)DIG.

We propose that shocks induced in the ISM by feedback mechanisms serve as a secondary ionisation source for the eDIG. Given that shock heating becomes substantial only when the kinetic energy is efficiently thermalised, both photoionisation and shocks may be regarded as "thermal" heating sources for the ISM. The observed enhancement in the $[\text{O III}]/H\beta$ ratio with increasing height can be interpreted as a mixing sequence between the predominant shock ionisation in the halo and the photoionisation in the disk.

To ascertain the impact of shocks on the ionisation budget of the eDIG, we constructed a suite of hybrid models that integrate both star formation and fast shock regimes. We conducted a BPT analysis by computing the hybrid models for each galaxy individually, given that each galaxy may exhibit unique characteristics necessitating a tailored ionisation diagnosis for the eDIG (BETIS I). Our results indicate that fast shocks significantly contribute to the ionisation budget of the eDIG, with contributions ranging from 20% to 50% across the sample.

The presence of shocks is further corroborated when examining the density-sensitive $[\text{S II}]$ doublet ratio as a function of the $[\text{O I}]/H\alpha$ ratio. For all galaxies, most of the eDIG regions near the midplane exhibit $[\text{S II}]$ line ratios close to the low-density limit, accompanied by low $[\text{O I}]/H\alpha$ values, which are indicative of H II region emission. However, regions with low $[\text{S II}]$ doublet ratios –typically at high midplane distances– coin-

side with regions exhibiting high $[O\text{I}]/H\alpha$ values, indicative of shock-compressed ionised gas. Therefore, the low $[S\text{II}]$ doublet ratios, along with their implied high gas densities and the fact that these regions exhibit higher $[O\text{I}]/H\alpha$ values, support a scenario in which wherein gas emission originates from shocks, likely induced by feedback from high-level star-forming regions within the galactic disk. In this scenario, fast shocks can account for the increase in the $[O\text{I}]/H\alpha$ ratio with distance from the midplane, with the highest $[O\text{I}]/H\alpha$ ratios corresponding to the shocked interface at the greatest distances from the midplane.

The contribution of fast shocks can vary significantly across different regions of the halo, with variations reaching up to 20% within the same galaxy. This variability arises from the distinct properties, physical processes, and structures inherent to each galaxy that affect the ionisation of the extraplanar gas. These structures include filaments, knots, extraplanar H II regions, and nearby neighbouring galaxies. Nonetheless, the distribution of H II regions within the disc consistently exerts a substantial influence on the ionisation of the halo gas.

A prime example of this phenomenon is IC1553. In the $[N\text{II}]/H\alpha$ emission line map, it reveals a biconical central structure within the halo, previously interpreted as indicative of outflows or superbubbles. Nonetheless, at the bicone's location ($MAD = 0$), the galaxy's disk is expected to exhibit a lower specific star formation rate (sSFR) along the line-of-sight due to the presence of the galaxy's bulge. This contrasts with the intense emission from the bright adjacent star-forming regions at the edge of the disk, observed in projection, which exhibit typical H II region (low) emission values. This scenario is more pronounced in the $[S\text{II}]/H\alpha$ and $[O\text{I}]/H\alpha$ maps, where the background emission conspicuously permeates the halo with typical extended eDIG values. These observations, coupled with the absence of any structure in $H\alpha$, $[O\text{III}]/H\beta$, the consistent $[S\text{II}]/[N\text{II}]$ ratio, and the lack of spatial correlation with potential ionisation sources within the disk, indicate that this bicone is an optical artefact resulting from the projection effect relative to the line-of-sight of the high-level SF regions in the galaxy's disk, in relation to a pervasive background eDIG emission in the halo.

From this perspective, it can be inferred that the extended eDIG emission comprises multiple overlapping components contingent upon the line of sight: eDIG emanating from low-density gas, typified by elevated $[N\text{II}]$, $[S\text{II}]$ line ratios, and gas ionised through star formation (SF) activity proximate to the midplane of edge-on galaxies, with typical H II line emission values. The overlaying patterns vary according to the morphology and extent of SF regions within the galactic plane, resulting in a complex morphology of the eDIG concerning line emissions.

To advance the Bidimensional Exploration of the warm-Temperature Ionised gas (BETIS) project, in forthcoming papers in this series we will examine the kinematic reflection of the eDIG connection with the galactic plane. Specifically, we will analyse radial variations in rotational velocity gradients (referred to as "lag"), which are correlated with the SFR and associated with morphological structures within the halo. Additionally, we will investigate the energy deposition into the ISM through SF-related feedback mechanisms, the primary source of the eDIG ionisation. Moreover, we will explore how the (e)DIG influences the determination of various parameters, including chemical abundances and SFR.

Acknowledgements. Based on the observations at ESO with program IDs: 096.B-0054(A) and 097.B-0041(A). R.G.D. acknowledges the CONAHCYT scholarship No. 1088965 and INAOE for the PhD program. The authors also

acknowledges Manuel Zamora and Raúl Naranjo for allowing us the usage of the Mextli cluster at INAOE. R.G.D. and L.G. acknowledge financial support from AGAUR, CSIC, MCIN and AEI 10.13039/501100011033 under projects PID2020-115253GA-I00, PIE 20215AT016, CEX2020-001058-M, and 2021-SGR-01270.

References

- Allen M. G., Groves B. A., Dopita M. A., Sutherland R. S., Kewley L. J., 2008, *ApJS*, **178**, 20
- Asplund M., Amarsi A. M., Grevesse N., 2021, *A&A*, **653**, A141
- Bacon R., et al., 2010, in McLean I. S., Ramsay S. K., Takami H., eds, Society of Photo-Optical Instrumentation Engineers (SPIE) Conference Series Vol. 7735, Ground-based and Airborne Instrumentation for Astronomy III. p. 773508 ([arXiv:2211.16795](https://arxiv.org/abs/2211.16795)), doi:10.1117/12.856027
- Baldwin J. A., Phillips M. M., Terlevich R., 1981, *PASP*, **93**, 5
- Baluja K. L., Burke P. G., Kingston A. E., 1980, *Journal of Physics B Atomic Molecular Physics*, **13**, L543
- Barnes A. T., et al., 2023, *ApJ*, **944**, L22
- Begelman M. C., Fabian A. C., 1990, *MNRAS*, **244**, 26P
- Belfiore F., et al., 2022, *A&A*, **659**, A26
- Binette L., Flores-Fajardo N., Raga A. C., Drissen L., Morisset C., 2009, *ApJ*, **695**, 552
- Binney J., 2005, in Braun R., ed., Astronomical Society of the Pacific Conference Series Vol. 331, Extra-Planar Gas. p. 131 ([arXiv:astro-ph/0409639](https://arxiv.org/abs/astro-ph/0409639)), doi:10.48550/arXiv.astro-ph/0409639
- Bizyaev D., et al., 2017, *ApJ*, **839**, 87
- Bizyaev D., Chen Y.-M., Shi Y., Roy N., Riffel R., Riffel R. A., Fernández-Trincado J. G., 2022, *MNRAS*, **516**, 3092
- Bland-Hawthorn J., Sutherland R., Agertz O., Moore B., 2007, *ApJ*, **670**, L109
- Boettcher E., Gallagher J. S. I., Zweibel E. G., 2019, *ApJ*, **885**, 160
- Bryant J. J., et al., 2015, *MNRAS*, **447**, 2857
- Bundy K., et al., 2015, *ApJ*, **798**, 7
- Cardelli J. A., Clayton G. C., Mathis J. S., 1989, *ApJ*, **345**, 245
- Ceverino D., Klypin A., 2008, in Bureau M., Athanassoula E., Barbu B., eds, Vol. 245, Formation and Evolution of Galaxy Bulges. pp 33–34 ([arXiv:0710.1666](https://arxiv.org/abs/0710.1666)), doi:10.1017/S1743921308017213
- Ceverino D., Klypin A., 2009, *ApJ*, **695**, 292
- Chevalier R. A., Clegg A. W., 1985, *Nature*, **317**, 44
- Cid Fernandes R., Mateus A., Sodré L., Stasińska G., Gomes J. M., 2005, *MNRAS*, **358**, 363
- Colbert E. J. M., Baum S. A., Gallimore J. F., O'Dea C. P., Christensen J. A., 1996, *ApJ*, **467**, 551
- Collins J. A., Rand R. J., 2001, *ApJ*, **551**, 57
- Combes F., 2014, in Seigar M. S., Treuhardt P., eds, Astronomical Society of the Pacific Conference Series Vol. 480, Structure and Dynamics of Disk Galaxies. p. 211 ([arXiv:1309.1603](https://arxiv.org/abs/1309.1603)), doi:10.48550/arXiv.1309.1603
- Comerón S., Salo H., Knapen J. H., Peletier R. F., 2019, *A&A*, **623**, A89
- Cowie L. L., McKee C. F., 1977, *ApJ*, **211**, 135
- Croom S. M., et al., 2012, *MNRAS*, **421**, 872
- Dahlem M., 1997, *PASP*, **109**, 1298
- Dahlem M., Lisenfeld U., Golla G., 1995, *ApJ*, **444**, 119
- Della Bruna L., et al., 2022a, *A&A*, **660**, A77
- Della Bruna L., et al., 2022b, *A&A*, **666**, A29
- Dettmar R. J., 1990, *A&A*, **232**, L15
- Dettmar R. J., 1998, in Breitschwerdt D., Freyberg M. J., Truemper J., eds, Vol. 506, IAU Colloq. 166: The Local Bubble and Beyond. pp 527–538
- Dirks L., Dettmar R. J., Bomans D. J., Kamphuis P., Schilling U., 2023, *A&A*, **678**, A84
- Domgorgen H., Mathis J. S., 1994, *ApJ*, **428**, 647
- Dopita M. A., Sutherland R. S., 1995, *ApJ*, **455**, 468
- Ferguson A. M. N., Wyse R. F. G., Gallagher J. S. I., Hunter D. A., 1996, *AJ*, **111**, 2265
- Ferrara A., Bianchi S., Dettmar R.-J., Giovanardi C., 1996, *ApJ*, **467**, L69
- Field G. B., 1989, *Highlights of Astronomy*, **8**, 567
- Finkbeiner D. P., 2003, *ApJS*, **146**, 407
- Flores-Fajardo N., Morisset C., Stasińska G., Binette L., 2011, *MNRAS*, **415**, 2182
- Gatto A., et al., 2017, *MNRAS*, **466**, 1903
- González-Díaz R., et al., 2024, *A&A*, **687**, A20
- Gray W. J., Oey M. S., Silich S., Scannapieco E., 2019, *ApJ*, **887**, 161
- Greenawalt B., Waltherbos R. A. M., Braun R., 1997, *ApJ*, **483**, 666
- Grisdale K. M., 2017, PhD thesis, University of Surrey, UK
- Guélin M., 1974, in Kerr F. J., Simonson S. C., eds, Vol. 60, Galactic Radio Astronomy. p. 51
- Haffner L. M., Reynolds R. J., Tuft S. L., 1999, *ApJ*, **523**, 223
- Haffner L. M., et al., 2009a, *Rev. Mod. Phys.*, **81**, 969
- Haffner L. M., et al., 2009b, *Reviews of Modern Physics*, **81**, 969

- Hewish A., Bell S. J., Pilkington J. D. H., Scott P. F., Collins R. A., 1968, *Nature*, **217**, 709
- Ho I. T., et al., 2016, *MNRAS*, **457**, 1257
- Hodges-Kluck E., Bregman J. N., 2014, *ApJ*, **789**, 131
- Hodges-Kluck E., Cafmeyer J., Bregman J. N., 2016, *ApJ*, **833**, 58
- Hoffmann T. L., Lieb S., Pauldrach A. W. A., Lesch H., Hultzsch P. J. N., Birk G. T., 2012, *A&A*, **544**, A57
- Hoopes C. G., Walterbos R. A. M., 2003, *ApJ*, **586**, 902
- Hopkins P. F., Kereš D., Oñorbe J., Faucher-Giguère C.-A., Quataert E., Murray N., Bullock J. S., 2014, *MNRAS*, **445**, 581
- Howk J. C., Savage B. D., 2000, *AJ*, **119**, 644
- Hoyle F., Ellis G. R. A., 1963, *Australian Journal of Physics*, **16**, 1
- Hummel E., Beck R., Dahlem M., 1991, *A&A*, **248**, 23
- Jenkins E. B., Meloy D. A., 1974, *ApJ*, **193**, L121
- Jo Y.-S., Seon K.-i., Shinn J.-H., Yang Y., Lee D., Min K.-W., 2018, *ApJ*, **862**, 25
- Kashibadze O. G., 2008, *Astrophysics*, **51**, 336
- Kaufmann T., Mayer L., Wadsley J., Stadel J., Moore B., 2006, *MNRAS*, **370**, 1612
- Kennicutt Robert C. J., 1998, *ARA&A*, **36**, 189
- Kennicutt R. C., Evans N. J., 2012, *ARA&A*, **50**, 531
- Kennicutt Robert C. J., Edgar B. K., Hodge P. W., 1989, *ApJ*, **337**, 761
- Kennicutt Robert C. J., Tamblyn P., Congdon C. E., 1994, *ApJ*, **435**, 22
- Kewley L. J., Dopita M. A., Sutherland R. S., Heisler C. A., Trevena J., 2001, *ApJ*, **556**, 121
- Klessen R. S., Glover S. C. O., 2016, in Revaz Y., Jablonka P., Teyssier R., Mayer L., eds, *Saas-Fee Advanced Course Vol. 43, Saas-Fee Advanced Course*. p. 85 ([arXiv:1412.5182](https://arxiv.org/abs/1412.5182)), doi:10.1007/978-3-662-47890-5_2
- Kopsacheili M., Zezas A., Leonidaki I., 2020, *MNRAS*, **491**, 889
- Kourkchi E., Tully R. B., 2017, *ApJ*, **843**, 16
- Lacerda E. A. D., et al., 2018, *MNRAS*, **474**, 3727
- Leitherer C., Robert C., Drissen L., 1992, *ApJ*, **401**, 596
- Levesque E. M., Kewley L. J., Larson K. L., 2010, *AJ*, **139**, 712
- Levy R. C., et al., 2019, *ApJ*, **882**, 84
- Li A., Fraternali F., Marasco A., Trager S. C., Pezzulli G., Mancera Piña P. E., Verheijen M. A. W., 2023, *MNRAS*, **520**, 147
- López-Cobá C., Sánchez S. F., Bland-Hawthorn J., Moiseev A. V., Cruz-González I., García-Benito R., Barrera-Ballesteros J. K., Galbany L., 2019, *MNRAS*, **482**, 4032
- López-Cobá C., et al., 2020, *AJ*, **159**, 167
- Lu L.-Y., et al., 2023, *MNRAS*, **519**, 6098
- Lugo-Aranda A. Z., Sánchez S. F., Barrera-Ballesteros J. K., López-Cobá C., Espinosa-Ponce C., Galbany L., Anderson J. P., 2024, *MNRAS*, **531**, 1000
- Mac Low M.-M., McCray R., 1988, *ApJ*, **324**, 776
- Madsen G. J., Reynolds R. J., 2005, *ApJ*, **630**, 925
- Madsen G. J., Reynolds R. J., Haffner L. M., 2006, *ApJ*, **652**, 401
- Marasco A., Fraternali F., Binney J. J., 2012, *MNRAS*, **419**, 1107
- Marinacci F., Fraternali F., Nipoti C., Binney J., Ciotti L., Londrillo P., 2011, *MNRAS*, **415**, 1534
- Martin C. L., 1997, *ApJ*, **491**, 561
- Mayya Y. D., et al., 2023, *MNRAS*, **521**, 5492
- McKee C. F., Hollenbach D. J., 1980, *ARA&A*, **18**, 219
- McKee C. F., Ostriker J. P., 1977, *ApJ*, **218**, 148
- Miller S. T., Veilleux S., 2003, *ApJS*, **148**, 383
- Minter A. H., Spangler S. R., 1997, *ApJ*, **485**, 182
- Mitronova S. N., Karachentsev I. D., Karachentseva V. E., Jarrett T. H., Kudrya Y. N., 2004, *Bulletin of the Special Astrophysics Observatory*, **57**, 5
- Molina M., Eracleous M., Barth A. J., Maoz D., Runnoe J. C., Ho L. C., Shields J. C., Walsh J. L., 2018, *ApJ*, **864**, 90
- Muñoz-Mateos J. C., et al., 2015, *ApJS*, **219**, 3
- Norman C. A., Ikeuchi S., 1989, *ApJ*, **345**, 372
- Osterbrock D. E., Ferland G. J., 2006, *Astrophysics of gaseous nebulae and active galactic nuclei*. University Science Books
- Otte B., Reynolds R. J., Gallagher J. S. I., Ferguson A. M. N., 2001, *ApJ*, **560**, 207
- Otte B., Gallagher J. S. I., Reynolds R. J., 2002, *ApJ*, **572**, 823
- Pettini M., West K. A., 1982, *ApJ*, **260**, 561
- Pildis R. A., Bregman J. N., Schombert J. M., 1994, *ApJ*, **427**, 160
- Putman M. E., 2017, in Fox A., Davé R., eds, *Astrophysics and Space Science Library Vol. 430, Gas Accretion onto Galaxies*. p. 1 ([arXiv:1612.00461](https://arxiv.org/abs/1612.00461)), doi:10.1007/978-3-319-52512-9_1
- Rand R. J., 1996, *ApJ*, **462**, 712
- Rand R. J., 1997, *ApJ*, **474**, 129
- Rand R. J., 1998, *ApJ*, **501**, 137
- Rand R. J., 2000, *ApJ*, **537**, L13
- Rand R. J., Kulkarni S. R., Hester J. J., 1990, *ApJ*, **352**, L1
- Rautio R. P. V., Watkins A. E., Comerón S., Salo H., Díaz-García S., Janz J., 2022, *A&A*, **659**, A153
- Reynolds R. J., 1971, PhD thesis, University of Wisconsin, Madison
- Reynolds R. J., 1985, *ApJ*, **294**, 256
- Reynolds R. J., 1989, *ApJ*, **345**, 811
- Reynolds R. J., Cox D. P., 1992, *ApJ*, **400**, L33
- Reynolds R. J., Roesler F. L., Scherb F., 1973, *ApJ*, **179**, 651
- Reynolds R. J., Haffner L. M., Tuftes S. L., 1999, *ApJ*, **525**, L21
- Reynolds R. J., Sterling N. C., Haffner L. M., 2001, *ApJ*, **558**, L101
- Rich J. A., Dopita M. A., Kewley L. J., Rupke D. S. N., 2010, *ApJ*, **721**, 505
- Rich J. A., Kewley L. J., Dopita M. A., 2011, *ApJ*, **734**, 87
- Rosa M., Richter O. G., 1988, *A&A*, **192**, 57
- Rosales-Ortega F. F., Arribas S., Colina L., 2012, *A&A*, **539**, A73
- Rossa J., Dettmar R. J., 2003a, *A&A*, **406**, 493
- Rossa J., Dettmar R. J., 2003b, *A&A*, **406**, 505
- Rossa J., Dettmar R.-J., Walterbos R. A. M., Norman C. A., 2004, *AJ*, **128**, 674
- Rossa J., Dettmar R. J., Walterbos R. A. M., Norman C. A., 2005, in Braun R., ed., *Astronomical Society of the Pacific Conference Series Vol. 331, Extra-Planar Gas*. p. 177
- Sánchez S. F., et al., 2012, *A&A*, **538**, A8
- Sánchez S. F., et al., 2016, *Rev. Mexicana Astron. Astrofis.*, **52**, 171
- Sardaneta M. M., Amram P., Rampazzo R., Rosado M., Sánchez-Cruces M., Fuentes-Carrera I., Ghosh S., 2024, *MNRAS*, **528**, 2145
- Sarkar K. C., Sternberg A., Gnat O., 2022, *ApJ*, **940**, 44
- Sato T., Martin C. L., Noeske K. G., Koo D. C., Lotz J. M., 2009, *ApJ*, **696**, 214
- Sembach K. R., Savage B. D., 1992, in *American Astronomical Society Meeting Abstracts #180*. p. 25.05
- Sembach K. R., Howk J. C., Ryans R. S. I., Keenan F. P., 2000, *ApJ*, **528**, 310
- Seon K.-I., 2009, *ApJ*, **703**, 1159
- Shapiro P. R., Benjamin R. A., 1991, *PASP*, **103**, 923
- Shapiro P. R., Field G. B., 1976, *ApJ*, **205**, 762
- Sharp R. G., Bland-Hawthorn J., 2010, *ApJ*, **711**, 818
- Shinn J.-H., Seon K.-I., 2015, *ApJ*, **815**, 133
- Simpson J. P., Colgan S. W. J., Cotera A. S., Erickson E. F., Hollenbach D. J., Kaufman M. J., Rubin R. H., 2007, *ApJ*, **670**, 1115
- Slavin J. D., Shull J. M., Begelman M. C., 1993, *ApJ*, **407**, 83
- Sokolowski J., 1993, in Cassinelli J. P., Churchwell E. B., eds, *Astronomical Society of the Pacific Conference Series Vol. 35, Massive Stars: Their Lives in the Interstellar Medium*. p. 540
- Sokolowski J., Bland-Hawthorn J., 1991, *PASP*, **103**, 911
- Soto K. T., Lilly S. J., Bacon R., Richard J., Conseil S., 2016, *MNRAS*, **458**, 3210
- Tacchella S., et al., 2022, *MNRAS*, **513**, 2904
- Tenorio-Tagle G., 1979, *A&A*, **71**, 59
- Tenorio-Tagle G., Bodenheimer P., 1988, *ARA&A*, **26**, 145
- Tüllmann R., Dettmar R. J., Soida M., Urbanik M., Rossa J., 2000, *A&A*, **364**, L36
- Tüllmann R., Pietsch W., Rossa J., Breitschwerdt D., Dettmar R. J., 2006, *A&A*, **448**, 43
- Veilleux S., Cecil G., Bland-Hawthorn J., 2005, *ARA&A*, **43**, 769
- Vorontsov-Vel'Yaminov B. A., Arkhipova V. P., 1968, *Trudy Gosudarstvennogo Astronomicheskogo Instituta*, **38**, 1
- Wang J., Heckman T. M., Lehnert M. D., 1997, *ApJ*, **491**, 114
- Weaver T. A., Zimmerman G. B., Woosley S. E., 1977, *Presupernova evolution of massive stars*
- Weber J. A., Pauldrach A. W. A., Hoffmann T. L., 2019a, *A&A*, **622**, A115
- Weber J. A., Pauldrach A. W. A., Hoffmann T. L., 2019b, *A&A*, **622**, A115
- Weilbacher P. M., et al., 2020, *A&A*, **641**, A28
- Werle A., Cid Fernandes R., Vale Asari N., Bruzual G., Charlot S., Gonzalez Delgado R., Herpich F. R., 2019, *MNRAS*, **483**, 2382
- Wiener J., Zweibel E. G., Oh S. P., 2013, *ApJ*, **767**, 87
- Wilson A. S., Tsvetanov Z. I., 1994, *AJ*, **107**, 1227
- Wood K., Mathis J. S., 2004, *MNRAS*, **353**, 1126
- Wood K., Haffner L. M., Reynolds R. J., Mathis J. S., Madsen G., 2005, *ApJ*, **633**, 295
- Zaragoza-Cardiel J., Fritz J., Aretxaga I., Mayya Y. D., Rosa-González D., Beckman J. E., Bruzual G., Charlot S., 2020, *MNRAS*, **499**, 1172
- Zurita A., Rozas M., Beckman J. E., 2000, *A&A*, **363**, 9
- de Vaucouleurs G., de Vaucouleurs A., Corwin Herold G. J., Buta R. J., Paturel G., Fouque P., 1991, *Third Reference Catalogue of Bright Galaxies*

Appendix A: PGC28308

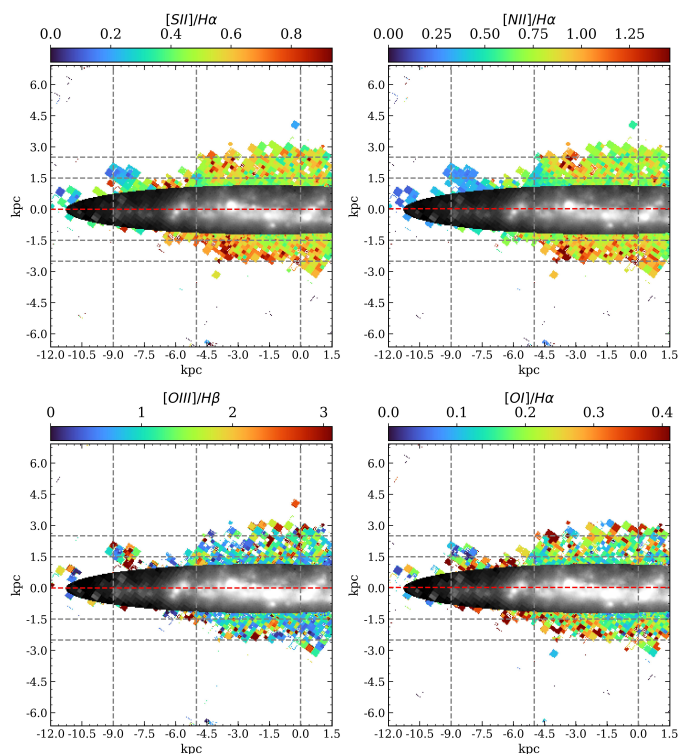


Fig. A.1: PGC28308 line ratio maps, similar to Figure 2. The grey dashed lines indicates the heights with respect to the midplane $z = \pm 1.5, \pm 2.5$ and major axis distances $MAD = -9, -5, 0$ kpc.

At a distance of 45.22 Mpc, PGC28308 is the most distant galaxy in the sample (Kashibadze 2008). Since all galaxies in the sample have the same total exposure time (except IC217; Com19), this results in lower S/N, a higher average bin size (175.4 pc), and a greater loss of information after performing the S/N and relative error cutout (see section 2).

These cutouts left us with data up to $|z| = 2.5$ kpc between $-4.5 \text{ kpc} \leq MAD \leq 1.5 \text{ kpc}$, and $|z| < 1.5$ kpc at $MAD < -4.5$ kpc for the $[S \text{ II}]/H\alpha$ and $[N \text{ II}]/H\alpha$ line ratio maps (Figure A.1).

With this data, we can observe that the trend of line ratios is consistent with what is found in the rest of the galaxies, reaching minimum values where the $\Sigma_{H\alpha}$ is maximum, and with the $[S \text{ II}]/H\alpha$ and $[N \text{ II}]/H\alpha$ ratios increasing in height, reaching values of 0.7 and 1.1 respectively (see Figure A.2). The $[O \text{ III}]/H\beta$ ratio remains approximately constant around 1.0 for $|z| > 0.7$ kpc and, for the $[O \text{ I}]/H\alpha$ ratio, the distribution remains flat at 0 for $z < -1$ kpc, probably due to the low S/N of the $[O \text{ I}]$ line, but reaches values of ~ 0.08 at $z > 0.7$ kpc. In all cases, the squares, triangles, and stars representing the height distributions at $MAD = 0, -3,$ and -9 kpc, respectively, follow a similar trend as the integrated distribution, which is also in line with what we observed in the rest of the galaxies. The radial dependence of the line ratios is not as clear as for the case of IC1553 by only considering Figure A.2. However, a clearer scenario can be seen in Figure A.3. Both $[S \text{ II}]/H\alpha$ and $[N \text{ II}]/H\alpha$ distributions consistently show higher ratios at $z = 2.5$ than at $z = 1.5$. Moreover, the differences between these distributions becomes more pronounced as the $\Sigma_{H\alpha}$ reaches higher values (at $MAD \sim -3$ kpc and $MAD \sim 0.5$ kpc). Examination of the MAD distributions also reveals the bidimensional structure of the eDIG, as the posi-

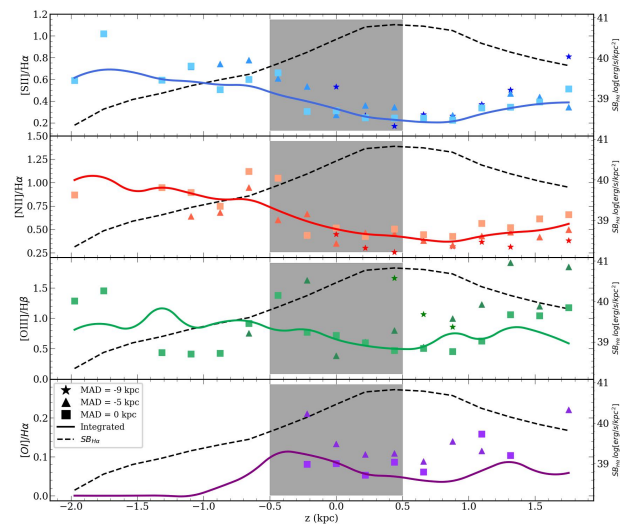


Fig. A.2: PGC28308 line ratio distributions of the with respect to the distance from the midplane. Similarly to Figure 3, for $MAD = -9$ (stars), -5 (triangles) and 0 (squares) kpc.

tions of relative maxima shift when the height increases in both $[S \text{ II}]/H\alpha$ and $[N \text{ II}]/H\alpha$ distributions.

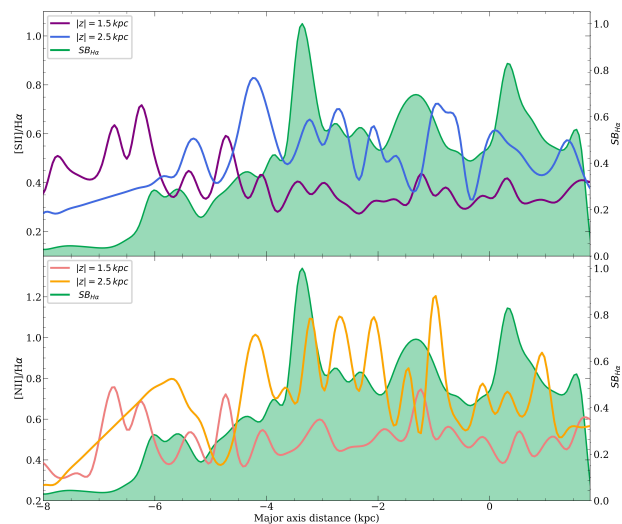


Fig. A.3: PGC28308 MAD distribution for $z = 1.5$ and 2.5 kpc.

As the sampling of this galaxy is lower due to the resolution and S/N cutouts, Figure A.5 does not show a dependence of the T_e with $|z|$ as clear as for IC1553. However, it is clear the dependence of the MAD with the ionisation ratio S^+/S . At $MAD = 0$ kpc (squares) $S^+/S \sim 0.3$, in contrast with $MAD = -5$ kpc (triangles), with $S^+/S \sim 0.5$. Although both MAD are within zones of the galactic plane exhibiting high $\Sigma_{H\alpha}$, Figure A.1 shows that the emission from H II regions is displaced relative to the line of sight. Specifically, the H II regions nearest to the -1.5 line at $MAD = 0$ kpc, indicating that the eDIG below the galactic plane at that MAD is highly ionised due to ongoing star formation. This ionisation leads to a reduction in the S^+/S ratio and consequently enhances the S^{++}/S ratio (Baluja et al. 1980; Haffner et al. 1999; Osterbrock & Ferland 2006). In general, the eDIG bins are located in the BPT diagram between both classical regimes of star formation and AGN (see Figure A.4). The hybrid models that best fit the data correspond to 50% of ionisation due

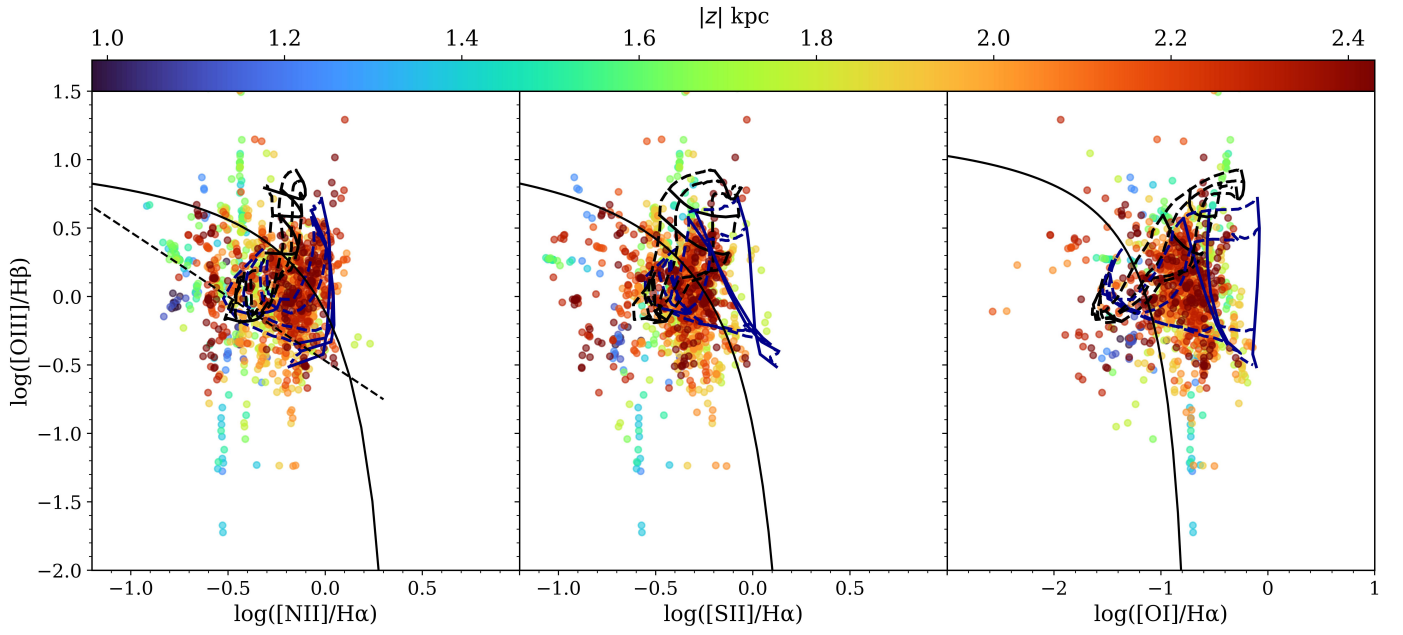


Fig. A.4: PGC28308 BPT with hybrid models, similar to Figure 7. 50% fast shocks and 50% star formation with $Z = Z_{\odot}$ and $q = 10^7$ cm/s.

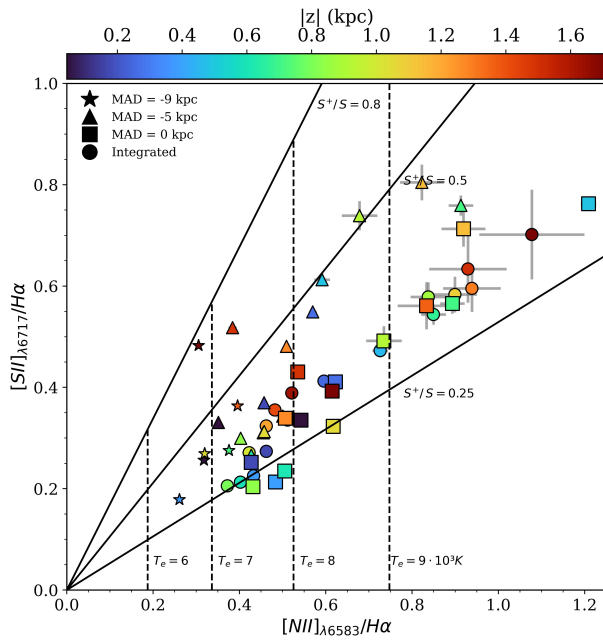


Fig. A.5: $[NII]_{\lambda 6583}/H\alpha$ vs. $[SII]_{\lambda 6717}/H\alpha$ for PGC28308. Similarly to Figure 5, for MAD = -9 (stars), -5 (triangles) and 0 (squares) kpc.

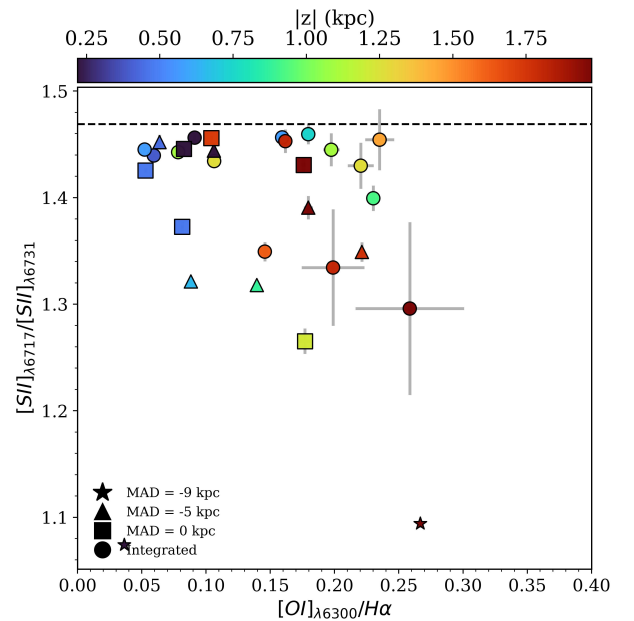


Fig. A.6: $[SII]_{\lambda 6717}/[SII]_{\lambda 6731}$ vs $[OI]/H\alpha$ for PGC28308. Similarly to Figure 8.

to fast shocks, and 50% star formation with $Z = Z_{\odot}$ and $q = 10^7$ cm/s.

Appendix B: PGC30591

As PGC28308, PGC30591 is a late-type spiral galaxy, although it is relatively closer in comparison (de Vaucouleurs et al. 1991). This results in a higher S/N and better data sampling after implementing the cutouts of 2, with bins reaching $|z|$ up to 2 kpc between $-1.5 \text{ kpc} < \text{MAD} < 3 \text{ kpc}$. From the line of sight, the distribution of H II seems homogeneous along the major axis, but with a brighter region between $1 \text{ kpc} < \text{MAD} < 2 \text{ kpc}$, near to the limit of $z = 0.5 \text{ kpc}$ (see Figure B.1). The influence of this region causes a clear decrease in the $[NII]/H\alpha$, $[SII]/H\alpha$ and

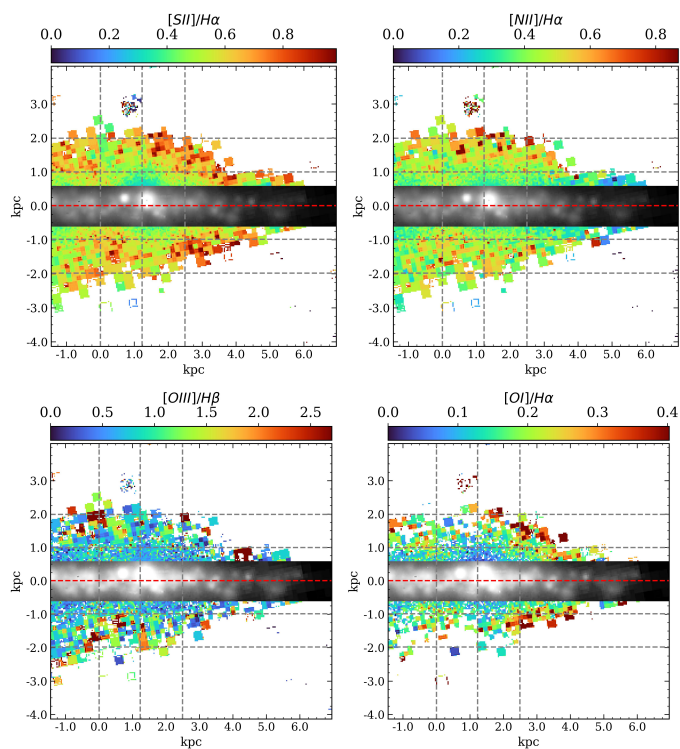


Fig. B.1: PGC30591 line ratio maps, similar to Figure 2. The grey dashed lines indicates the heights with respect the midplane $z = \pm 1, \pm 2$ and major axis distances $MAD = 0, 1.25, 2.5$ kpc.

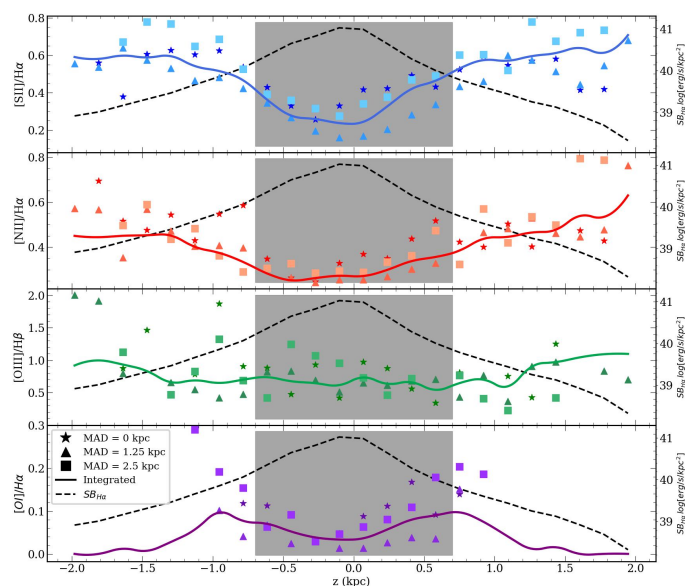


Fig. B.2: PGC30591 line ratio distributions of the with respect the distance from the midplane. Similarly to Figure 3, for $MAD = 0$ (stars), 1.25 (triangles) and 2.5 (squares) kpc.

$[O I]/H\alpha$ line ratios between $z = 0.5$ kpc and $z = 1.5$ kpc in comparison with the rest of the eDIG (see Figure B.1).

Figure B.2 shows the same anti-correlation than in the other cases; the line ratios reaching minimum values where the $\Sigma_{H\alpha}$ is maximum, and increasing in height. $[N II]/H\alpha$ and $[S II]/H\alpha$ remains approximately flat at $z < -1$ kpc, reaching values of 0.3 and 0.6, respectively, but continuing to increase beyond these values at $z > 1$ kpc. $[O I]/H\alpha$ also increases

up to 0.1 at $|z| = 1$ kpc and then decreases dramatically. The $[O III]/H\beta$ distribution remains flat around 0.6 for $|z| < 1$ kpc, and reach ~ 1 at $|z| > 1$ kpc. The distributions at $MAD = 0, 1.25$ and 2.5 kpc (stars, triangles and squares respectively) follow the same trend that the integrated distribution, as for the rest of the galaxies.

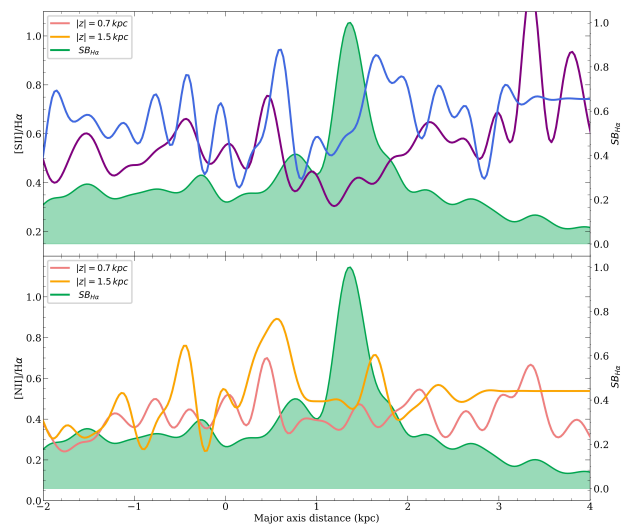


Fig. B.3: PGC30591 MAD distribution for $z = 0.7$ and 1.5 kpc.

Additionally, the distribution of triangles, where the most luminous star-forming regions are located in the plane, consistently exhibits lower line ratios compared to the other distributions. This aligns with what has been observed for IC1553 (see section 3). This can also be seen in the MAD distribution (Figure B.3). In addition to the typical increase in the value of the line ratios at higher heights observed in all galaxies of the sample, between $1 \text{ kpc} < MAD < 2 \text{ kpc}$, where the surface brightness of $\Sigma_{H\alpha}$ reaches its maximum values, both line ratios for both heights decrease.

Furthermore, the difference between the distributions for $z = 0.7$ kpc and 1.5 kpc becomes maximum for the $[S II]/H\alpha$ ratio (similarly to IC1553, with up to 0.5 dex). We can also observe a shift in the relative maxima of the $[N II]/H\alpha$ MAD distribution (more pronounced than for PGC28308) between $1 \text{ kpc} < MAD < 2 \text{ kpc}$: where the $\Sigma_{H\alpha}$ distribution reaches its maximum at $MAD \approx 0.4$ kpc, the $[N II]/H\alpha$ distribution at $z = 0.7$ kpc reaches its relative maximum (0.45) in that interval at $MAD \approx 0.55$ kpc, and for $z = 1.5$ kpc, the relative maximum (0.65) is reached at $MAD \approx 0.7$ kpc. This shift of ~ 0.15 kpc can also be observed in the absolute maximum at $MAD \approx 0.5$ kpc. Thus, this shift in the MAD distribution for different heights may be attributed to the spherical structure of ionisation between $z = 0.5$ kpc and $z = 1.5$ kpc, situated above the brighter star-forming region between $1 \text{ kpc} < MAD < 2 \text{ kpc}$ (see Figure B.1).

In Figure B.5, the T_e follows a dependency on $|z|$, increasing linearly with respect to the distance from the midplane and reaching values up to $9 \cdot 10^3$ K. This result is also consistent with the findings in IC1553 and other authors (Reynolds 1985; Madsen & Reynolds 2005). However, the ionisation fraction S^+/S does not seem to exhibit strong differences for different MADs, as all the points for S^+/S fall between approximately 0.35 and 0.8. Since the differences in the $H\alpha$ emission of the galactic plane at differences MADs is not that pronounced (not as IC1553 at least), we expect Figure B.5 to be more similar to PGC28308 (Figure A.5) than IC1553 (Figure 5), and S^+/S to be mixed at dif-

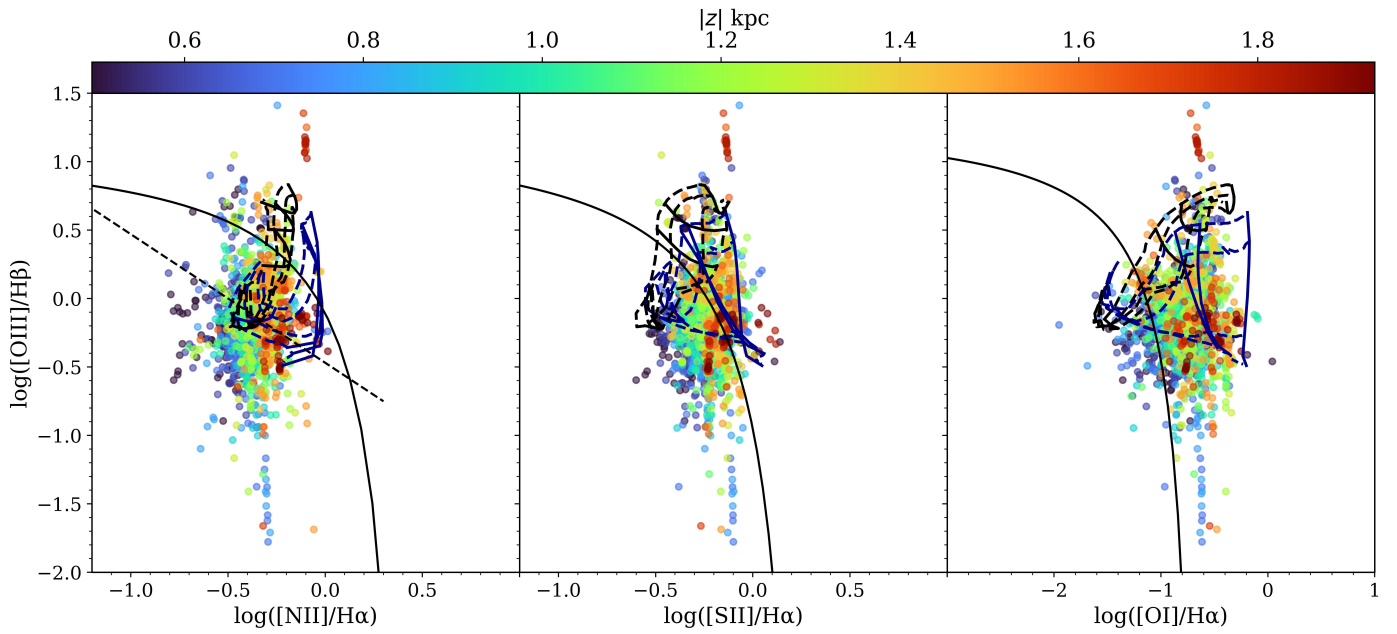


Fig. B.4: PGC30591 BPT with hybrid models, similar to Figure 7. 40% fast shocks and 60% star formation with $Z = Z_{\odot}$ and $q = 10^7$ cm/s.

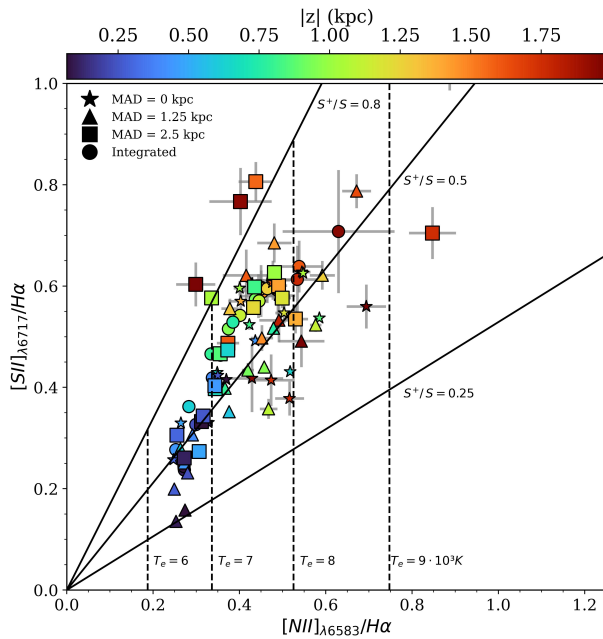


Fig. B.5: $[NII]_{\lambda 6583}/H\alpha$ vs. $[SII]_{\lambda 6717}/H\alpha$ for PGC30591. Similarly to Figure 5, for MAD = 0 (stars), 1.25 (triangles) and 2.5 (squares) kpc.

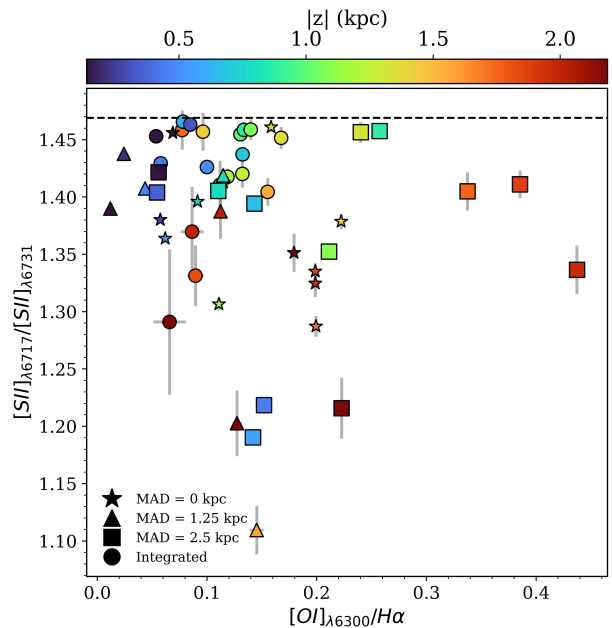


Fig. B.6: $[SII]_{\lambda 6717}/[SII]_{\lambda 6731}$ vs $[OI]_{\lambda 6300}/H\alpha$ for PGC30591. Similar to Figure 8.

ferent distances from the midplane. Similar results are expected for the BPT diagram (Figure B.4). The best fit hybrid models correspond to 40% of ionisation due to fast shocks, and 60% star formation with $Z = Z_{\odot}$ and $q = 10^7$ cm/s. In this case, the dependence on height is more evident, as there is not a strong mixture of different ionisation conditions, and the data sampling due to S/N is better than for PGC28308. The figure illustrates that the points nearest to the galactic plane tend to align closer to the classical star-forming regime of the BPT diagram, and vice versa.

Appendix C: ESO544-27

ESO544-27, along with ESO469-15, is the most edge-on galaxy in the sample, with $i = 90^\circ$. classified as an Sb galaxy (Mitronova et al. 2004), exhibits a more homogeneous emission from the galactic plane, mildly symmetric with respect to the centre of the galaxy, at MAD = 0 kpc. In consequence, the eDIG line maps exhibits the same symmetry (see figure Figure C.1), being evident the increase in the line ratios with respect to the distance from the midplane solely by examining the maps.

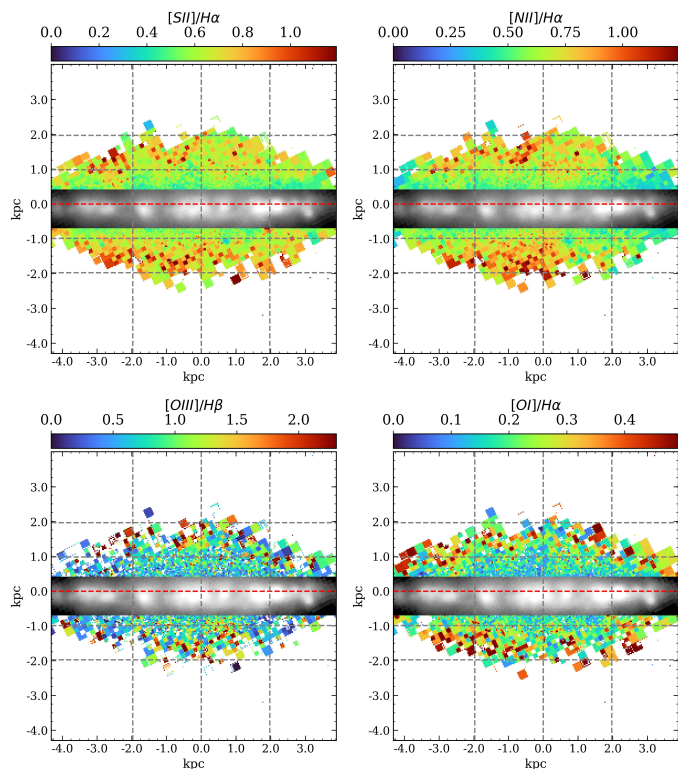


Fig. C.1: ESO544-27 line ratio maps, similar to Figure 2. The grey dashed lines indicates the heights with respect the midplane $z = \pm 1, \pm 2$ and major axis distances $MAD = -2, 0, 2$ kpc.

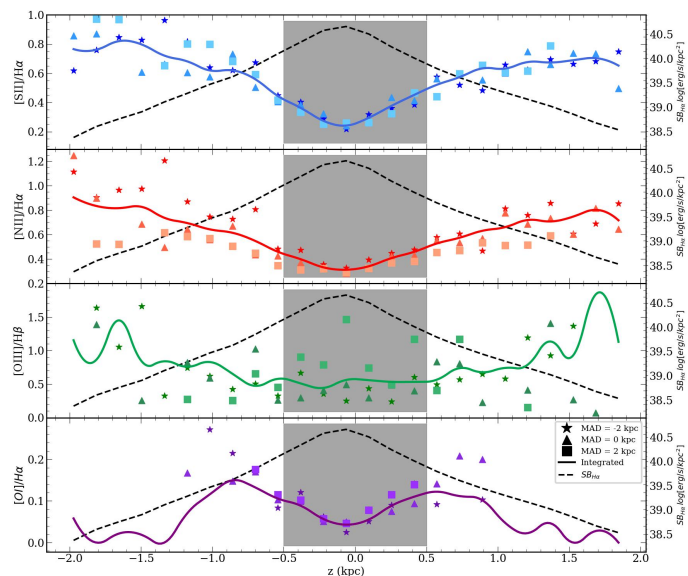


Fig. C.2: ESO544-27 line ratio distributions of the with respect the distance from the midplane. Similarly to Figure 3, for $MAD = -2$ (stars), 0 (triangles) and 2 (squares) kpc.

The height distributions of the line ratios (Figure C.2) show the same behaviour than in the rest of the galaxies. The line ratios reach minimum values where the $\Sigma_{H\alpha}$ is maximum, and increase in height, up to 0.8 for $[S II]/H\alpha$, 0.9 for $[N II]/H\alpha$ and 1.5 for $[O III]/H\beta$. $[O I]/H\alpha$ reaches ~ 0.1 at $|z| = 1$ kpc and then falls dramatically. The stars, triangles and squares distributions were strategically selected to be, respectively, in the mid-

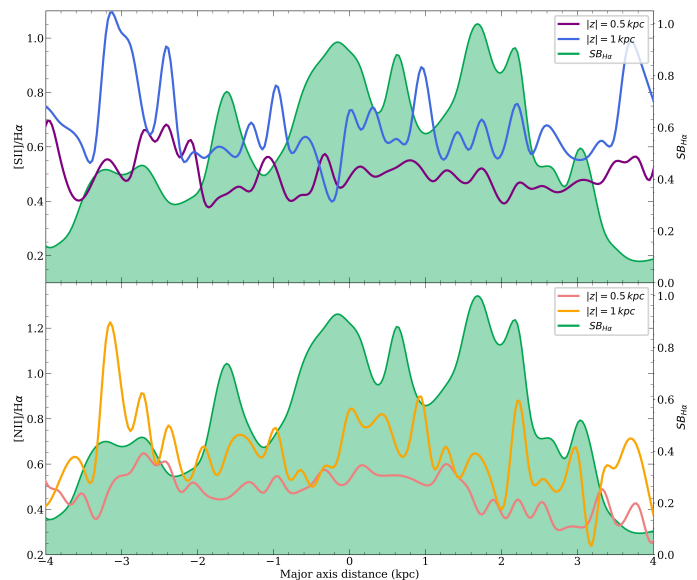


Fig. C.3: ESO544-27 MAD distribution for $z = 0.5$ and 1 kpc.

dle of two star-forming regions ($MAD = -2$ kpc), the centre of the galaxy ($MAD = 0$ kpc) and in the middle of a star-forming region ($MAD = 2$ kpc). All distributions are similar, but the stars at $MAD = -2$ kpc present lower $[N II]/H\alpha$, specially at higher distances from the midplane. In general, all points are mixed between them, showing no clear differences in the height distributions between different MADs. The MAD distribution (Figure C.3) shows precisely the homogeneity in the eDIG; the $[N II]/H\alpha$ and $[S II]/H\alpha$ distributions remains basically flat along the major axis at both heights, being more consistent the difference between the distributions at both heights. This strengthens the evidence regarding the direct effect of the galactic plane on the ionisation structure of the eDIG. Furthermore, within the ranges of $-4 \text{ kpc} < MAD < -2$ kpc and $3 \text{ kpc} < MAD < 4$ kpc, where the $\Sigma_{H\alpha}$ is lower, the disparities between the distributions at both heights are maximal for both $[N II]/H\alpha$ and $[S II]/H\alpha$ distributions. This consistency aligns with findings in other galaxies of the sample.

The homogeneity in the eDIG for this galaxy is also evident in figures C.5 and C.4. The T_e increases linearly with the distance from the midplane, up to $\sim 10^4$ K, and all the points remain close to the diagonal line corresponding to $S^+/S = 0.5$. Also, in the BPT, the hybrid models that best fit the data correspond to 50% of ionisation due to fast shocks, and 50% star formation with $Z = Z_\odot$ and $q = 10^7 \text{ cm/s}$. As for PGC30591, the dependence on height is more evident, as there is not a strong mixture of different ionisation conditions, with the points nearest to the galactic plane tending to align closer to the classical star-forming regime of the BPT diagram, and vice versa.

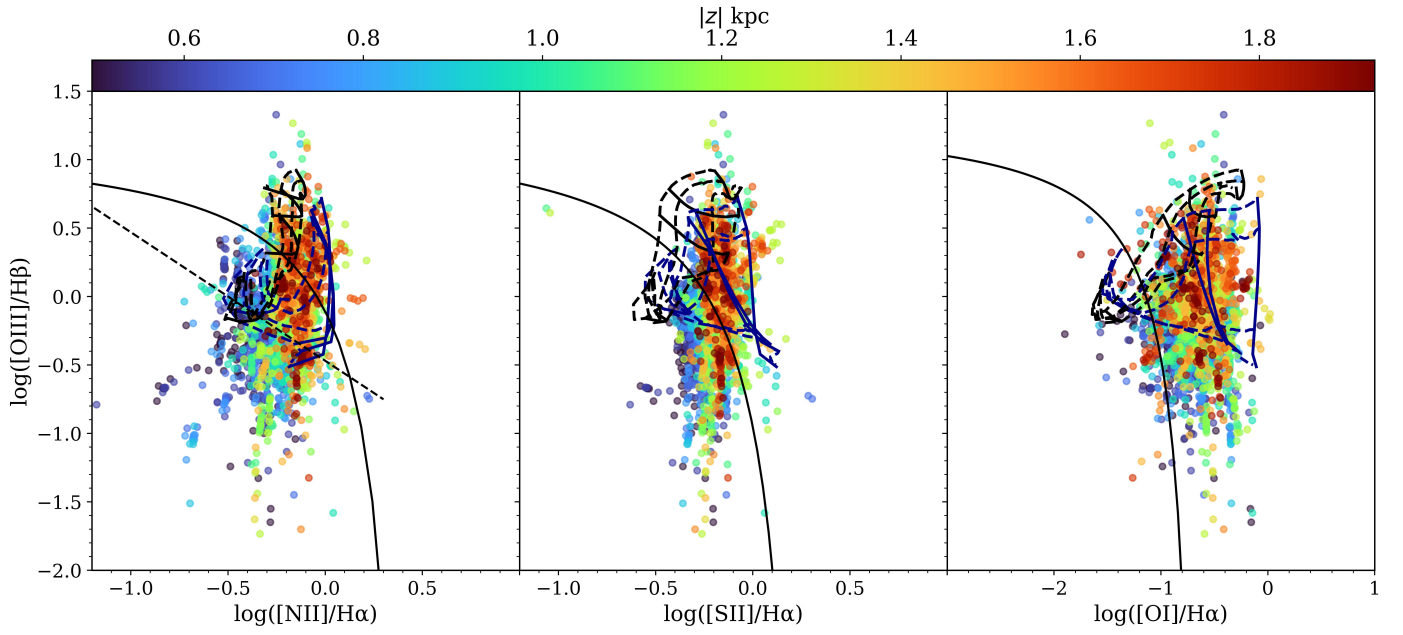


Fig. C.4: ESO544-27 BPT with hybrid models, similar to Figure 7. 50% fast shocks and 50% star formation with $Z = Z_{\odot}$ and $q = 10^7$ cm/s.

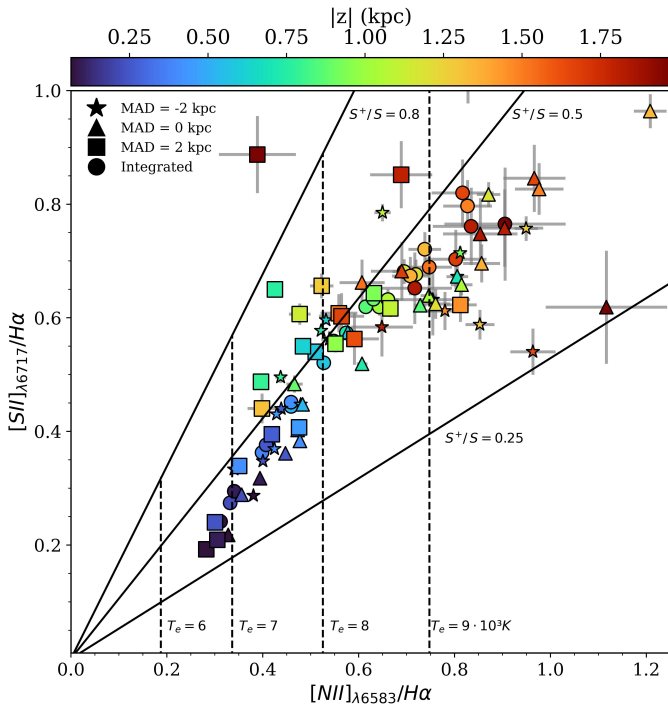


Fig. C.5: $[NII]_{\lambda 6583}/H\alpha$ vs. $[SII]_{\lambda 6717}/H\alpha$ for ESO544-27. Similarly to Figure 5, for MAD = -2 (stars), 0 (triangles) and 2 (squares) kpc.

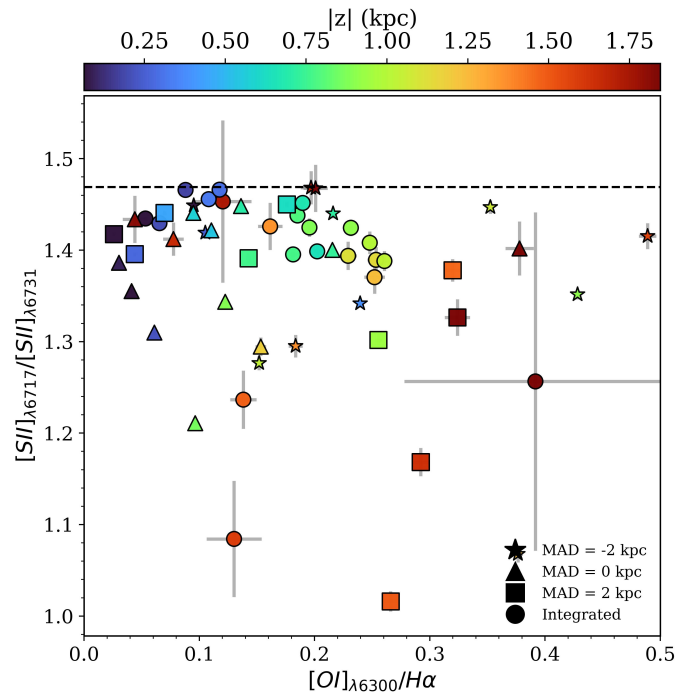


Fig. C.6: $[SII]_{\lambda 6717}/[SII]_{\lambda 6731}$ vs $[OI]_{\lambda 6300}/H\alpha$ for ESO544-27. Similarly to Figure 8.

Appendix D: ESO443-21

The late-type galaxy ESO443-21, along with the irregular galaxy IC1553, stands out as one of the most peculiar galaxies in the eBETIS sample. The excellent S/N of the data for this galaxy enables us to sample the extraplanar gas up to a distance of 4.5 kpc from the midplane. This sampling and high S/N ratio have enabled us to detect a broad knot-shape filamentous structure at a distance of 1.5 kpc, extending up to a height of 4.5 kpc within the range of $-1 \text{ kpc} < \text{MAD} < 2.5 \text{ kpc}$. This is evident not only in the $\text{H}\alpha$ map of Figure 1, but also when examining the emission line maps in Figure D.1, where the structure is clearly visible as a filament characterised by low $[\text{S II}]/\text{H}\alpha$ and $[\text{N II}]/\text{H}\alpha$ ratios.

The presence of this knot significantly influences the overall behaviour of the line ratio distributions and the ionisation structure of the eDIG. Figure D.2 shows that greater distances from the midplane, the $[\text{S II}]/\text{H}\alpha$ and $[\text{N II}]/\text{H}\alpha$ ratios deviate from the observed tendency to increase in other galaxies, and instead begin to decrease at $|z| \lesssim 2.5 \text{ kpc}$. Between $2 \text{ kpc} < z < 4 \text{ kpc}$, where the filament is located, the decrease is more gradual, with a slight increase in the ratios observed at $z \approx 3 \text{ kpc}$. The stars distribution at $\text{MAD} = 0 \text{ kpc}$ consistently falls below the other distributions, particularly between $2 \text{ kpc} < z < 4 \text{ kpc}$, exhibiting differences of up to 0.6 dex for the $[\text{S II}]/\text{H}\alpha$ ratio and 0.4 for the $[\text{N II}]/\text{H}\alpha$ ratio. This emphasises the significant impact of the filament on the ratios. In Figure D.3, the MAD distributions show the impact of the filament as well. The differences in the distributions between $z = 1.5 \text{ kpc}$ and $z = 3 \text{ kpc}$ for both line ratios are higher compared to the rest of the galaxies, mainly because of the larger difference in the selected heights. At $z = 1.5 \text{ kpc}$, both $[\text{S II}]/\text{H}\alpha$ and $[\text{N II}]/\text{H}\alpha$ ratios remain relatively flat. However, at $z = 3 \text{ kpc}$, the line ratios experience a significant decline at $\text{MAD} < 2 \text{ kpc}$, reaching levels typical of the eDIG close to H II regions found in other galaxies. This effect is particularly notable for $[\text{S II}]/\text{H}\alpha$, which drops from 0.9 to 0.2, reversing the trend of increasing line ratios with height.

In Figure D.4, the general trend again indicates an increase in electron temperature with height. However, for the circles rep-

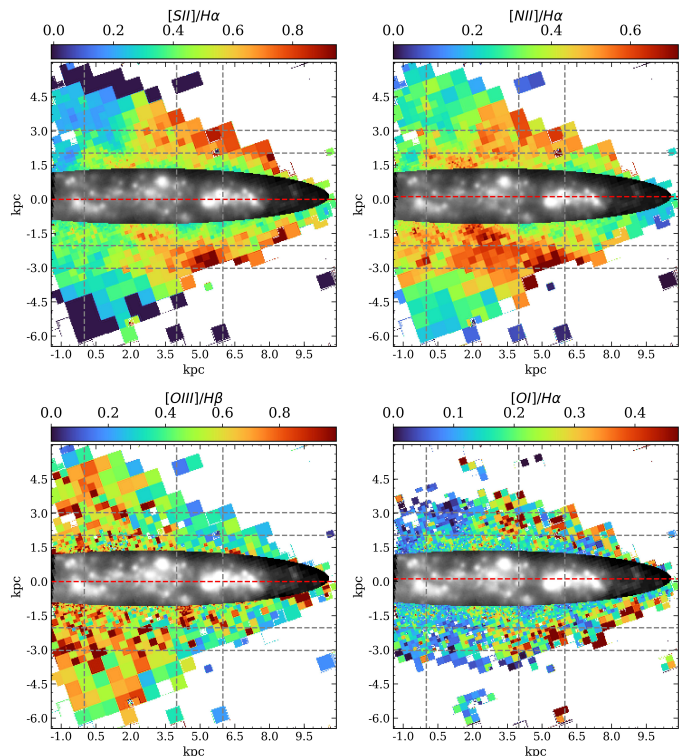


Fig. D.1: ESO443-21 line ratio maps, similar to Figure 2. The grey dashed lines indicate MAD = 0, 4, 6 kpc.

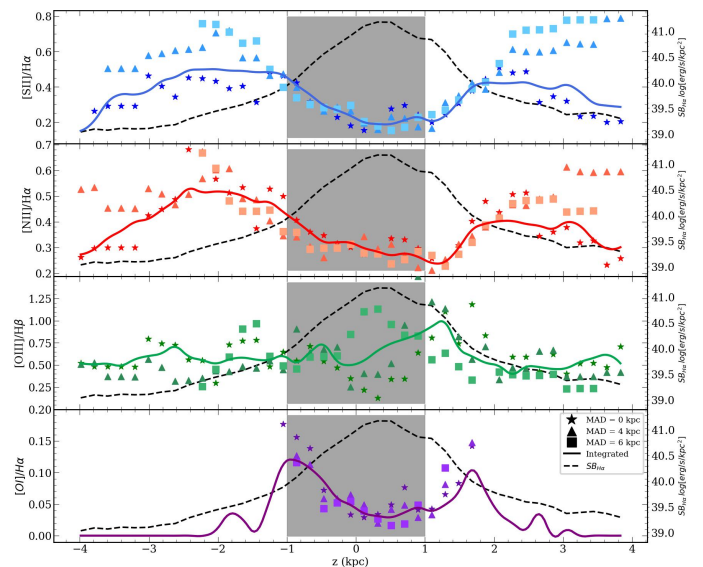
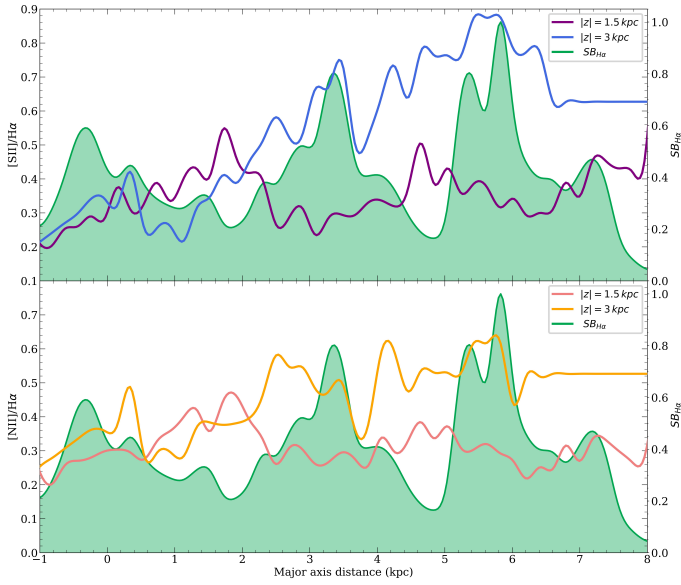
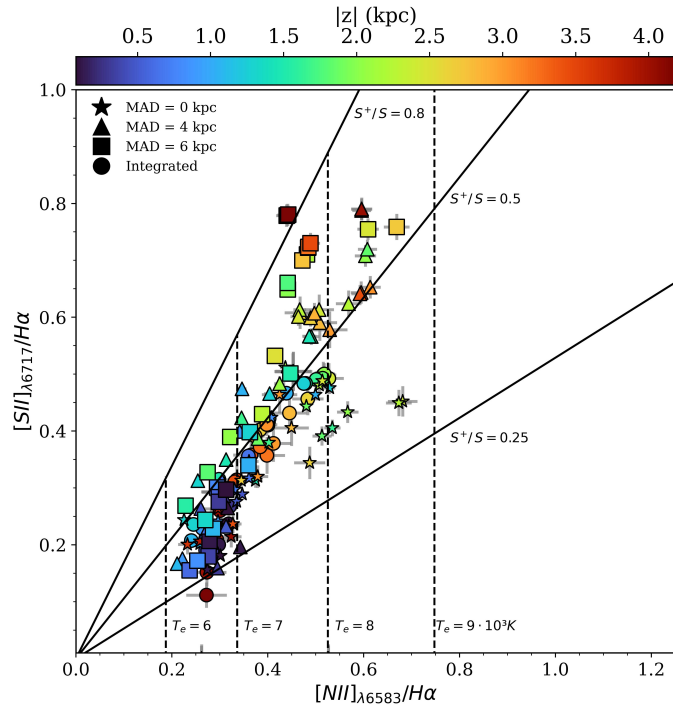


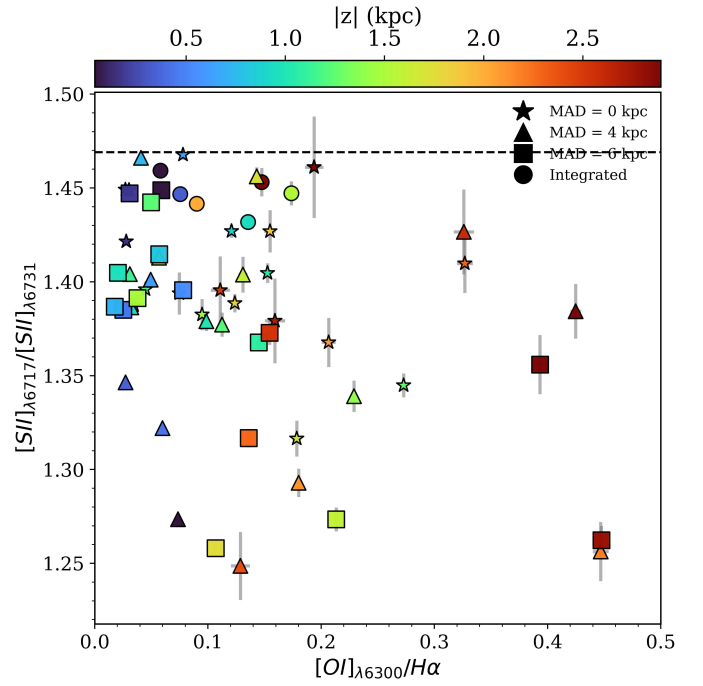
Fig. D.2: ESO443-21 line ratio distributions of the with respect to the distance from the midplane. Similarly to Figure 3, for MAD = 0 (stars), 4 (triangles) and 6 (squares) kpc.

resenting the integrated fluxes along the major axis, this trend disappears. The S^+/S fraction remains approximately constant at 0.5 but increases in height up to 0.8 for greater distances from the midplane. This finding is consistent with what we observed in other galaxies: a higher S^+/S ratio when the distance from the H II regions is greater, indicating an ionisation regime favouring collisions. Additionally, for the stars corresponding to $\text{MAD} = 0 \text{ kpc}$ and between $1.5 \text{ kpc} < z < 3.5 \text{ kpc}$ (where the knot is lo-


 Fig. D.3: ESO443-21 MAD distribution for $z = 1.5$ and 3 kpc.

 Fig. D.4: $[NII]_{\lambda 6583}/H\alpha$ vs. $[SII]_{\lambda 6717}/H\alpha$ for ESO443-21. Similarly to Figure 5, for MAD = 0 (stars), 4 (triangles) and 6 (squares) kpc.

cated), the S^+/S ratio drops to ~ 0.3 , suggesting a regime more similar to ionisation due to star formation.

This last figure suggests an asymmetry in the ionisation of the eDIG due to the filament, indicating different regimes when considering $z < 0$ or $z > 0$. To verify this, we present the BPT diagrams with the hybrid models separately for $z < 0$ and for $z > 0$. The best fit hybrid models for the points at $z > 0$ correspond to 20% of ionisation due to fast shocks, and 80% star formation with $Z = 2Z_{\odot}$ and $q = 10^7$ cm/s. For $z < 0$ correspond to 30% of ionisation due to fast shocks, and 70% star formation with the same parameters. The presence of the knot only affects an


 Fig. D.5: $[SII]_{\lambda 6717}/[SII]_{\lambda 6731}$ vs $[OI]_{\lambda 6300}/H\alpha$ for ESO443-21. Similar to Figure 8.

additional contribution of star formation to the overall ionisation mechanisms by up to 10%.

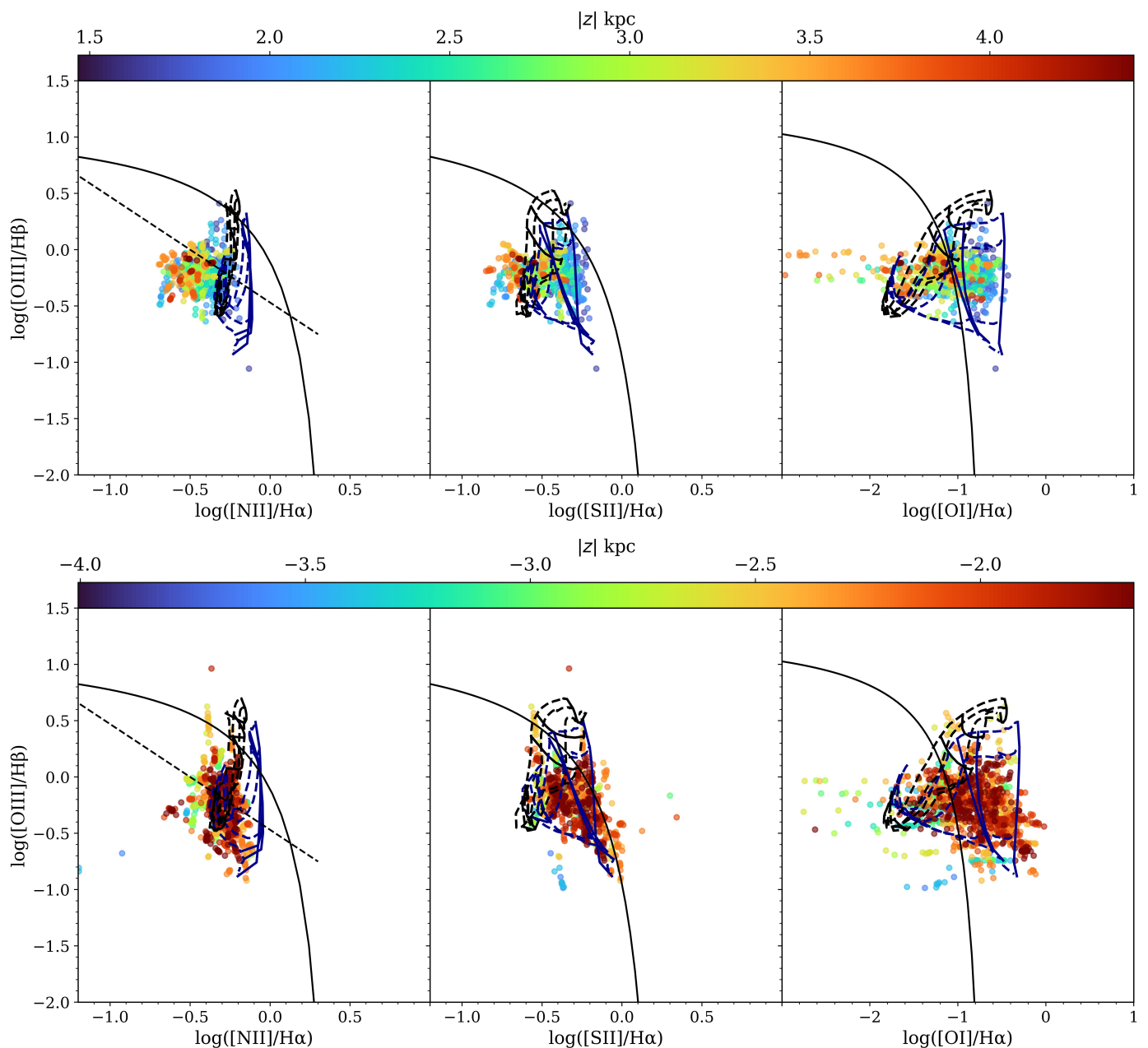


Fig. D.6: ESO443-21 BPT with hybrid models, similar to Figure 7. Up: BPT for bins at $z > 0$. Hybrid models correspond to 20% fast shocks and 80% star formation with $Z = Z_{\odot}$ and $q = 10^7$ cm/s. Down: BPT for bins at $z < 0$. Hybrid models correspond to 30% fast shocks and 70% star formation with $Z = 2Z_{\odot}$ and $q = 10^7$ cm/s.

Appendix E: ESO469-15

The galaxy ESO469-15 exhibits a noticeable presence of discrete extraplanar H II regions (also reported by other authors, e.g. Rautio et al. 2022). Before performing the analysis, we masked all the extraplanar H II regions using the PYTHON routine DAOSTARFINDER from the PHOTUTILS⁵ package. Figure E.1 shows the line maps after the H II regions removal. The line ratios near to the H II regions are even lower than those close to the bright galactic centre, being considerably low compared to the rest of the eDIG, specially at $z < 0$, where most of the extraplanar H II regions are located. The effect of the extraplanar H II regions is clear in the line distributions (Figure E.2).

⁵ DAOSTARFINDER documentation.

The trend of the integrated distribution changes continuously along the distance from the midplane, and squares distributions (at $MAD = 1.5$, where most of the extraplanar H II regions are located) present considerably lower line ratios in comparison with the rest of the distributions at $z < 0$, up to 0.6 for the $[S II]/H\alpha$ and $[N II]/H\alpha$ ratios. $[O III]/H\beta$ ratio shows a mixed tendency for every distribution, as for the rest of the galaxies. Finally, the $[O I]/H\alpha$ ratio shows lower values at $MAD = 0$ kpc and $z \approx 0$ kpc, since for at higher distances the S/N of the $[O I]$ line is not sufficient to sample those regions.

The MAD distributions in Figure E.3 reinforce what was observed in IC1553, and generally across the entire sample. The $\Sigma_{H\alpha}$ along the major axis of the galaxy is notably more prominent

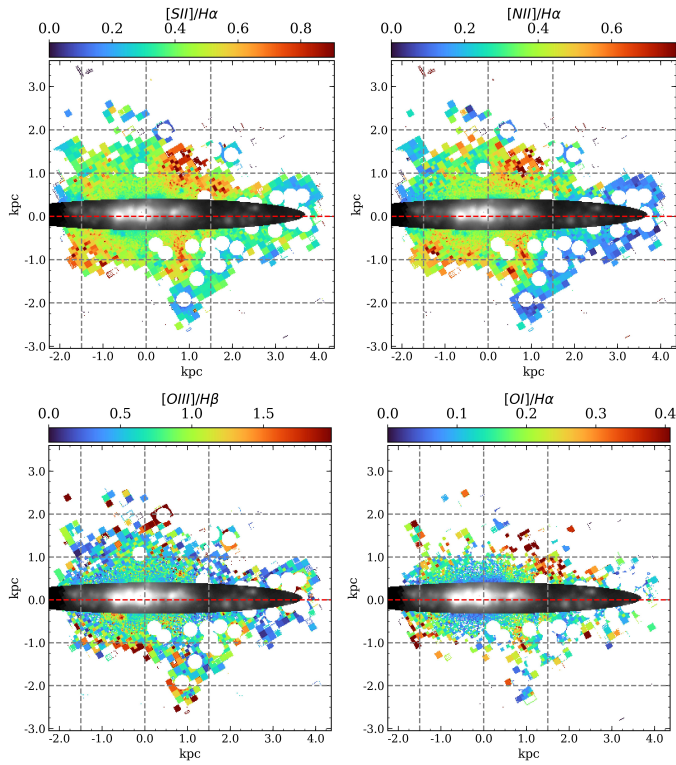


Fig. E.1: ESO469-15 line ratio maps, similar to Figure 2. The grey dashed lines indicates the heights with respect the midplane $z = \pm 1, \pm 2$ and major axis distances $MAD = -1.5, 0, 1.5$ kpc.

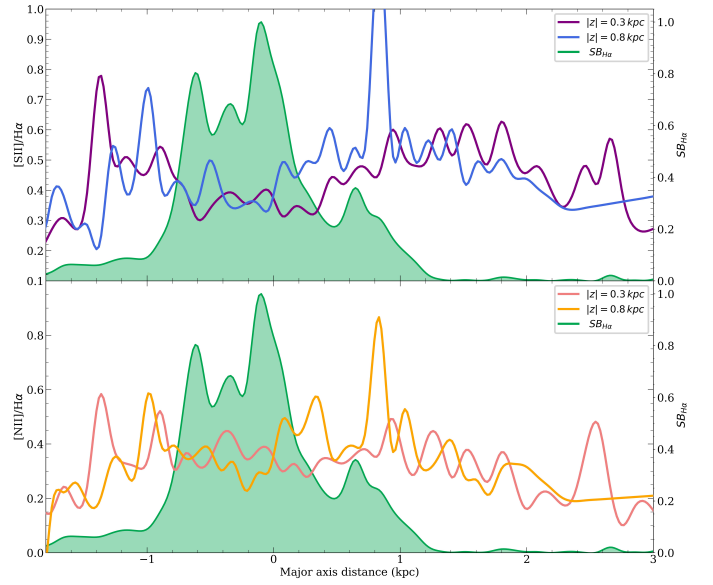


Fig. E.3: ESO469-15 MAD distribution for $z = 0.3$ and 0.8 kpc.

In addition to these results, the hybrid models in the BPT diagram for all the eDIG (Figure E.4) indicate only a 30% contribution of fast shocks in the ionisation mechanisms of the eDIG. This represents the lowest contribution in the sample when the data in the BPT diagram is not restricted by z or MAD.

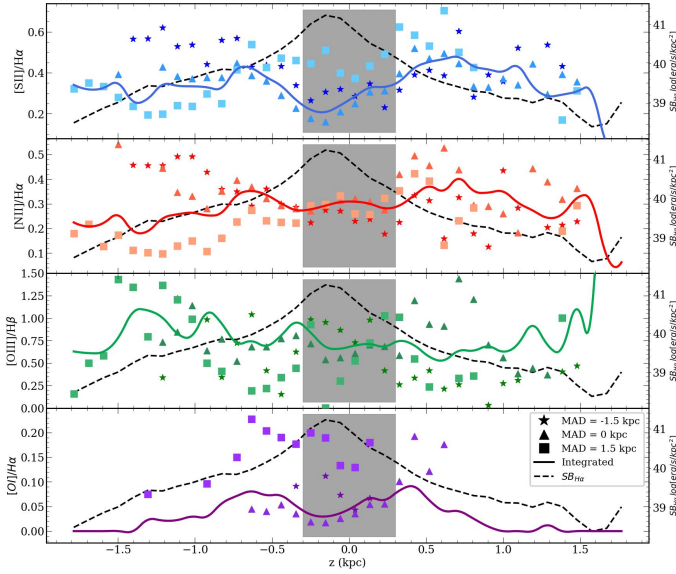


Fig. E.2: ESO469-15 line ratio distributions of the with respect the distance from the midplane. Similarly to Figure 3, for $MAD = -1.5$ (stars), 0 (triangles) and 1.5 (squares) kpc.

between $-1 \text{ kpc} < MAD < 1 \text{ kpc}$. Subsequently, the $[S \text{ II}]/H\alpha$ and $[N \text{ II}]/H\alpha$ ratios experience a sudden decrease at these MADs.

The T_e in the eDIG (E.5) is also influenced by the presence of extraplanar H II regions, being notably lower for all the eDIG compared to other galaxies, ranging only between 6 and $8 \cdot 10^3$ K.

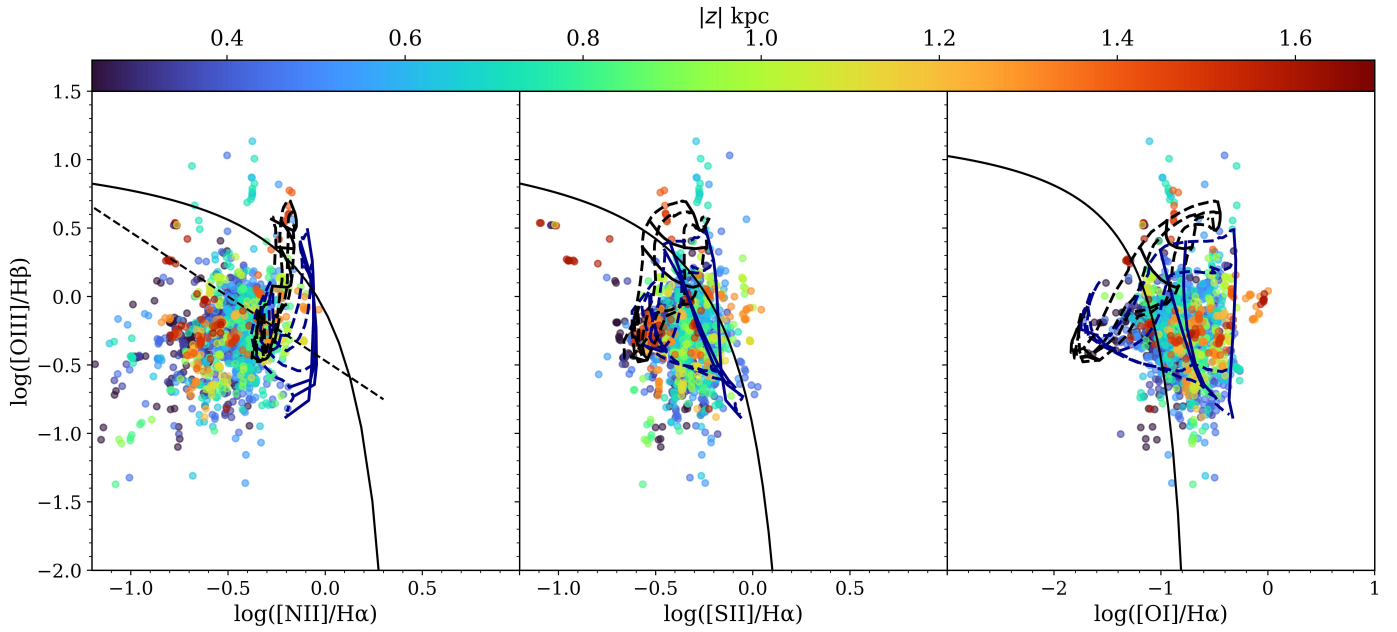


Fig. E.4: ESO469-15 BPT with hybrid models, similar to Figure 7. 30% fast shocks and 70% star formation with $Z = 2Z_{\odot}$ and $q = 10^7$ cm/s.

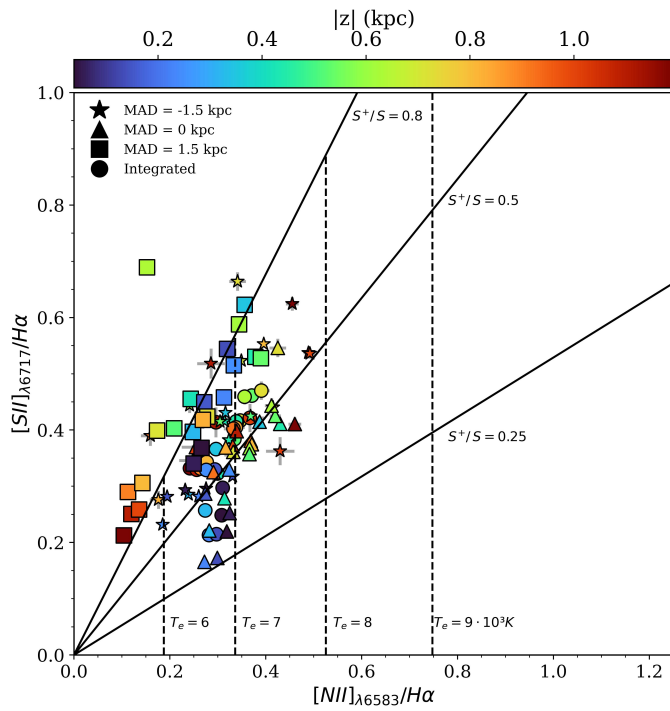


Fig. E.5: $[NII]_{\lambda 6583}/H\alpha$ vs. $[SII]_{\lambda 6717}/H\alpha$ for ESO469-15. Similarly to Figure 5, for MAD = -1.5 (stars), 0 (triangles) and 1.5 (squares) kpc.

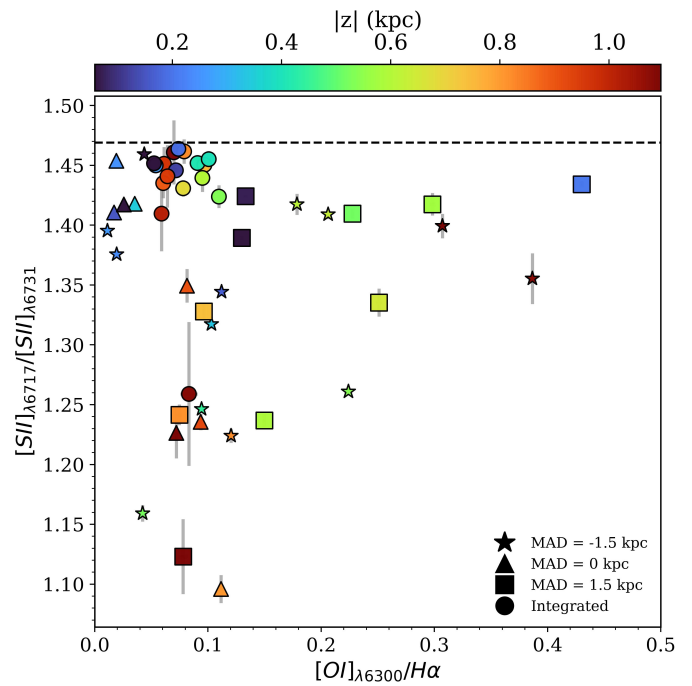


Fig. E.6: $[SII]_{\lambda 6717}/[SII]_{\lambda 6731}$ vs $[OI]_{\lambda 6300}/H\alpha$ for ESO469-15. Similarly to Figure 8.

Appendix F: ESO157-49

ESO157-49 is the only galaxy in the sample to have nearby neighbours (Kourkchi & Tully 2017). It was observed that its closest neighbour, the dwarf galaxy ESO157-48 located southwest of the galaxy, has influence on its kinematics, that can result in an asymmetry in the properties of the extraplanar ionised gas (Rautio et al. 2022). Figure F.1 shows precisely this asymmetry. ESO157-49 presents a more uniform emission from the galactic plane, similar to ESO544-27 but with a slightly brighter emission observed between $-1.5 \text{ kpc} \lesssim \text{MAD} \lesssim 3 \text{ kpc}$. However, the extraplanar ionised structure at $z > 0$ is clearly different from that at $z < 0$, being the structure of the eDIG at $z < 0$ apparently tilted and shifted compared to the eDIG at $z > 0$. The line ratios height distributions (F.2) show that at $z < 0$ the $[\text{N II}]/\text{H}\alpha$, $[\text{S II}]/\text{H}\alpha$ and $[\text{O I}]/\text{H}\alpha$ line ratios reach lower maximum values than at $z > 0$ (up to 0.2 on every ratio). Furthermore, at $\text{MAD} = 2.5 \text{ kpc}$, where the $\Sigma_{\text{H}\alpha}$ is higher, the $[\text{N II}]/\text{H}\alpha$ and $[\text{S II}]/\text{H}\alpha$ line ratios are consistently remain lower, as observed for the rest of the sample (also seen in the MAD distributions; Figure F.3).

The T_e (see Figure F.4) increases in height as usual, up to $\sim 9 \cdot 10^3 \text{ K}$, and the ionisation fraction S^+/S remains approximately constant at ~ 0.35 at the highest distances from the midplane ($z \simeq 2 \text{ kpc}$). In addition, at $\text{MAD} = 2.5 \text{ kpc}$, where the $\Sigma_{\text{H}\alpha}$ is higher (corresponding to squares in Figure F.4), the T_e remains below $\sim 8 \cdot 10^3 \text{ K}$.

Similar to ESO544-27, the significant uniformity in the emission from the galactic plane relative to the line of sight results in hybrid models that best fit the points on the BPT diagram (Figure F.6) corresponding to 50% ionisation due to fast shocks and 50% due to star formation. However, at $2 \text{ kpc} < \text{MAD} < 3 \text{ kpc}$, where the $\Sigma_{\text{H}\alpha}$ is higher, the contribution of fast shocks drops to 30%, and at $-0.5 \text{ kpc} < \text{MAD} < 0.5 \text{ kpc}$, the contribution is still 50% (see Figure F.7). Additionally, in both cases, the dependence of the ionisation regime on height is evident, with bins corresponding to higher z being further from the demarcation of Kewley et al. (2001).

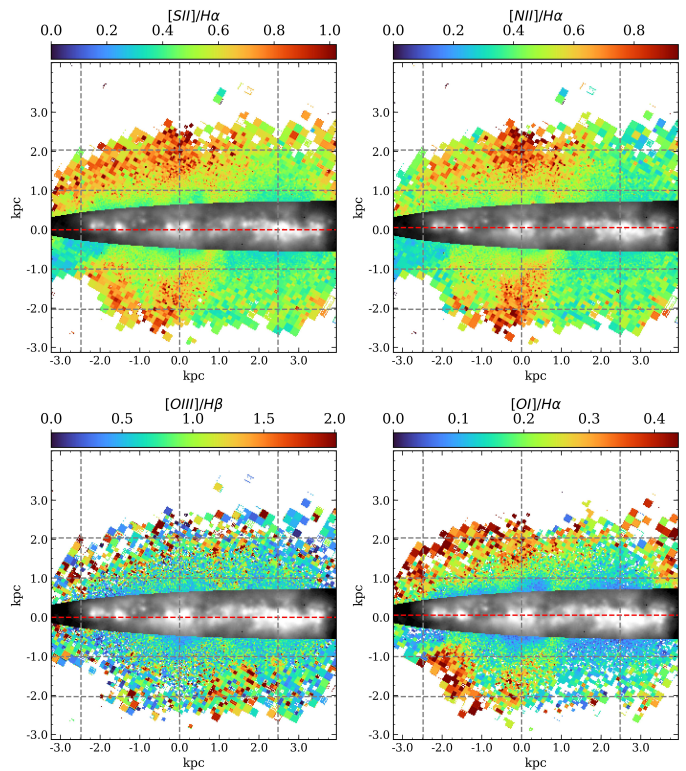


Fig. F.1: ESO157-49 line ratio maps, similar to Figure 2. The grey dashed lines indicates the heights with respect the midplane $z = \pm 1, \pm 2$ and major axis distances $\text{MAD} = -2.5, 0, 2.5 \text{ kpc}$.

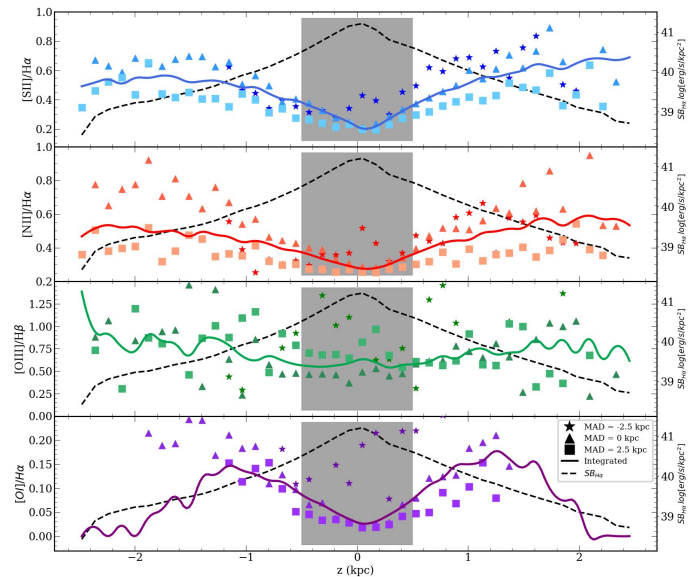


Fig. F.2: ESO157-49 line ratio distributions of the with respect the distance from the midplane. Similarly to Figure 3, for $\text{MAD} = -2.5$ (stars), 0 (triangles) and 2.5 (squares) kpc.

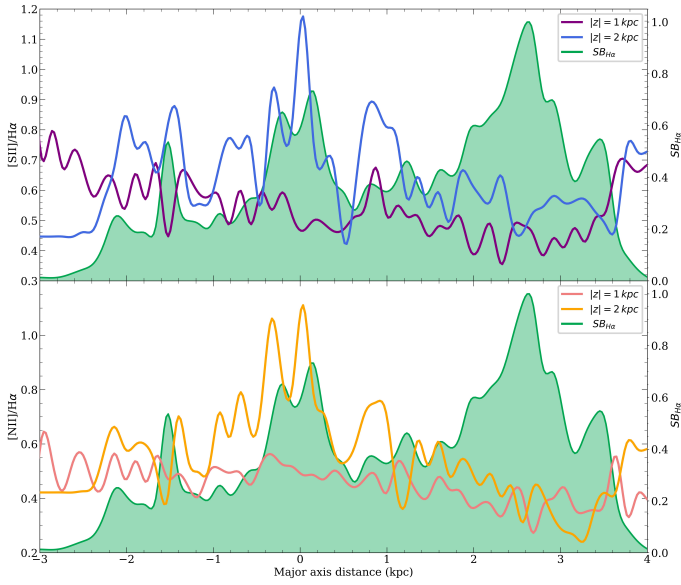


Fig. F.3: ESO157-49 MAD distribution for $z = 1$ and 2 kpc.

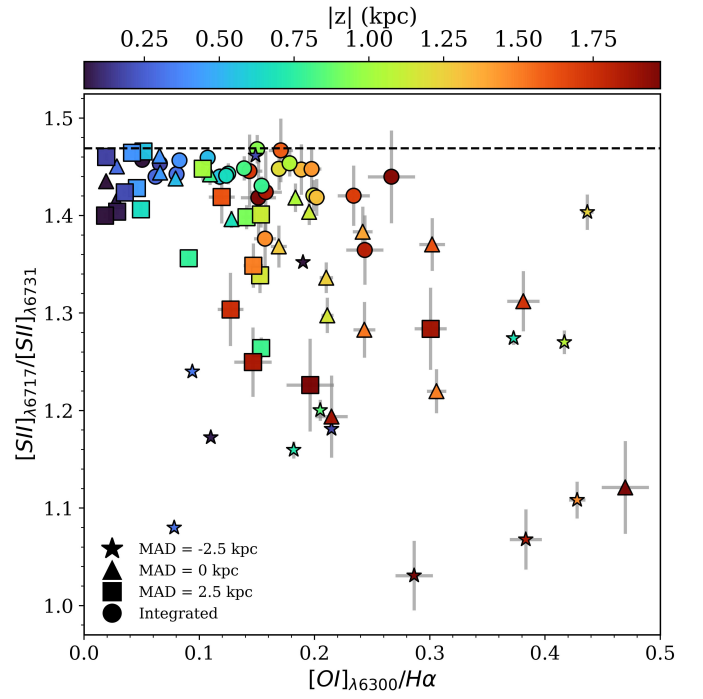


Fig. F.5: $[S II]_{\lambda 6717}/[S II]_{\lambda 6731}$ vs $[O I]_{\lambda 6300}/H\alpha$ for ESO157-49. Similarly to Figure 8.

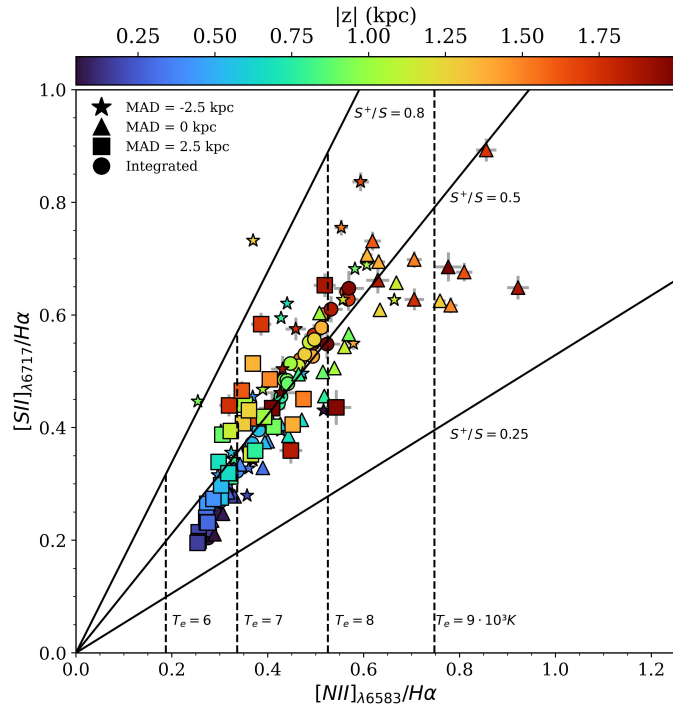


Fig. F.4: $[N II]_{\lambda 6583}/H\alpha$ vs. $[S II]_{\lambda 6717}/H\alpha$ for ESO157-49. Similarly to Figure 5, for MAD = -2.5 (stars), 0 (triangles) and 2.5 (squares) kpc.

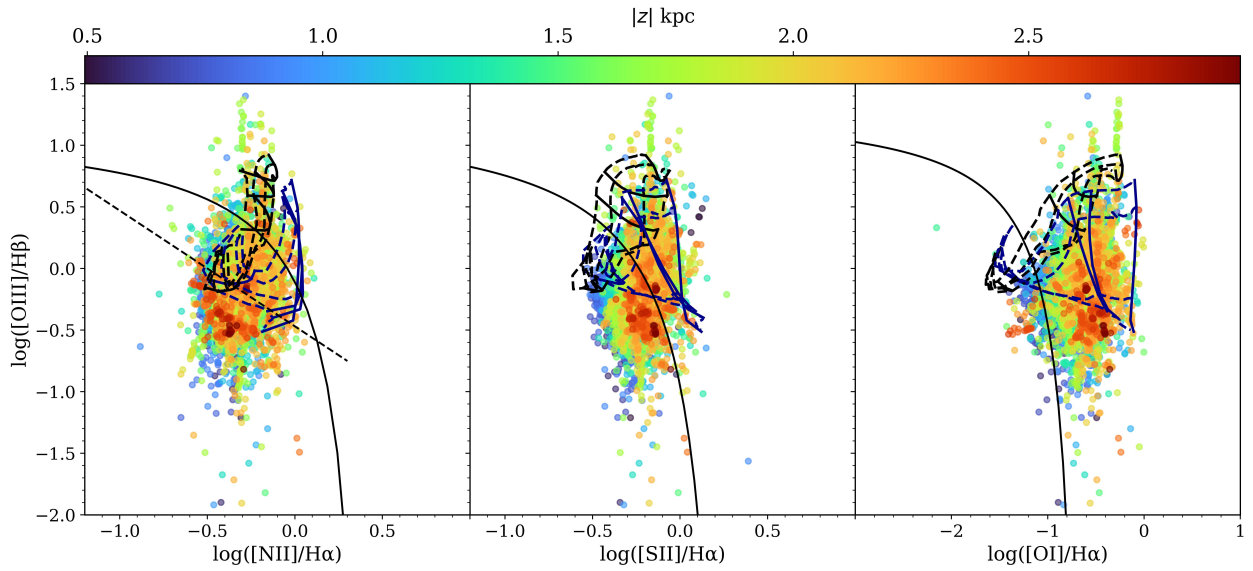


Fig. F.6: ESO157-49 BPT with hybrid models, similar to Figure 7. 50% fast shocks and 50% star formation with $Z = 2Z_{\odot}$ and $q = 10^7$ cm/s.

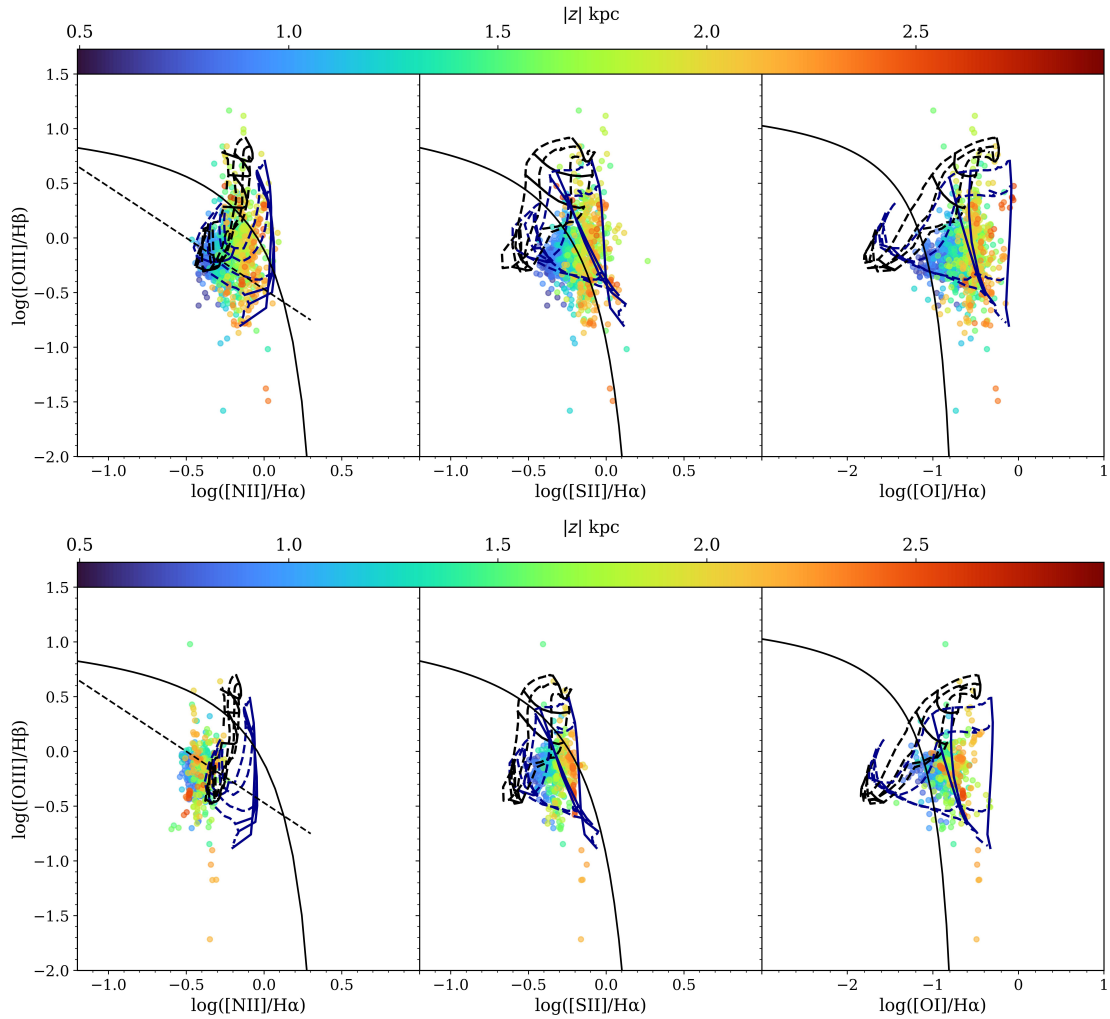


Fig. F.7: ESO157-49 BPT with hybrid models, similar to Figure 10. Up: BPT for bins between $-0.5 \text{ kpc} < \text{MAD} < 0.5 \text{ kpc}$. Hybrid models correspond to 50% fast shocks and 50% star formation with $Z = 2Z_{\odot}$ and $q = 10^7$ cm/s. Down: BPT for bins between $2.25 \text{ kpc} < \text{MAD} < 2.75 \text{ kpc}$. Hybrid models correspond to 30% fast shocks and 70% star formation with $Z = 2Z_{\odot}$ and $q = 10^7$ cm/s.

Appendix G: IC217

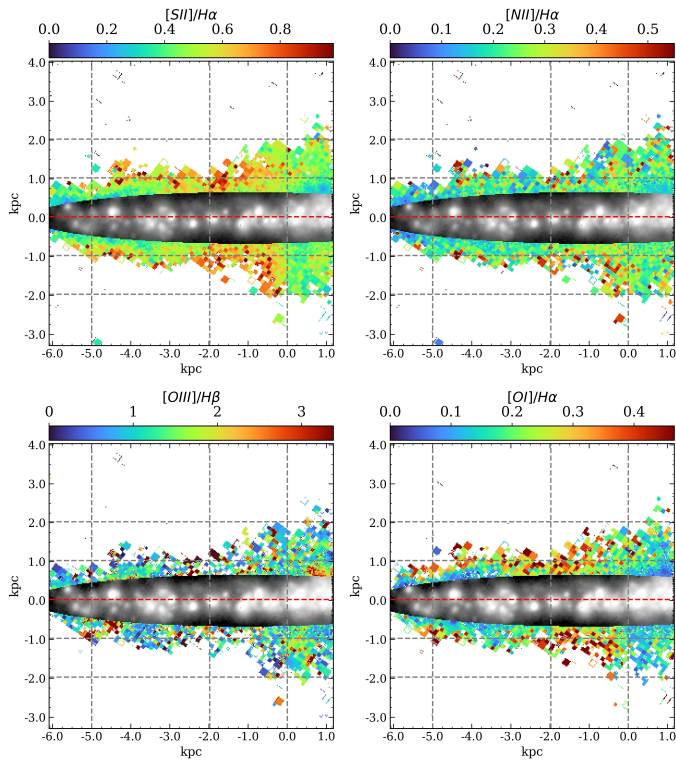


Fig. G.1: IC217 line ratio maps, similar to Figure 2. The grey dashed lines indicates the heights with respect the midplane $z = \pm 1, \pm 2$ and major axis distances MAD = -5, -2, 0 kpc.

IC217 has the lowest exposure time among the sample, only three exposures of 2624 seconds in contrast to the four exposures for the other galaxies. After excluding bins with $S/N < 2$ and relative errors exceeding 40%, this results in the least comprehensive data sampling among the galaxies in the sample. However, Figure G.1 illustrates the variations in ionisation regimes at different MADs observed in the other galaxies. Between $-3 \text{ kpc} < \text{MAD} < -1 \text{ kpc}$, where the concentration of H II regions with respect to the line of sight is lower, the line ratios in the eDIG exhibit higher values compared to the rest of the galaxy. Nevertheless, the level of data sampling is insufficient to conduct a more in-depth analysis of this galaxy. The line ratio distributions (Figure G.2) and the BPT (Figure G.3) a mixed regime between different MADs, along with a general eDIG ionisation consisting of a 50% contribution from fast shocks and 50% of star formation.

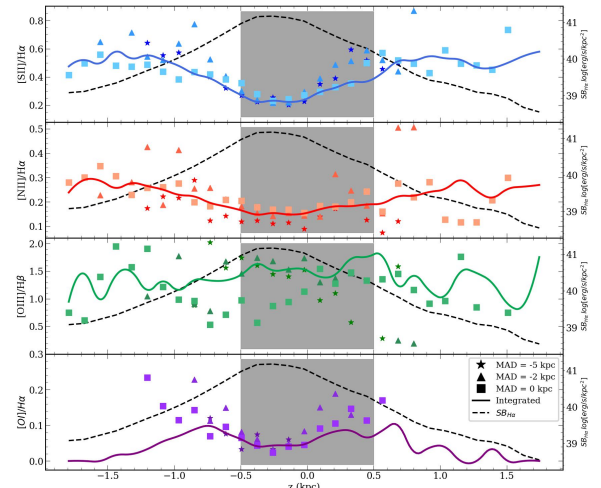


Fig. G.2: IC217 line ratio distributions of the with respect distance from the midplane. Similarly to Figure 3, for MAD = -5 (stars), -2 (triangles) and 0 (squares) kpc.

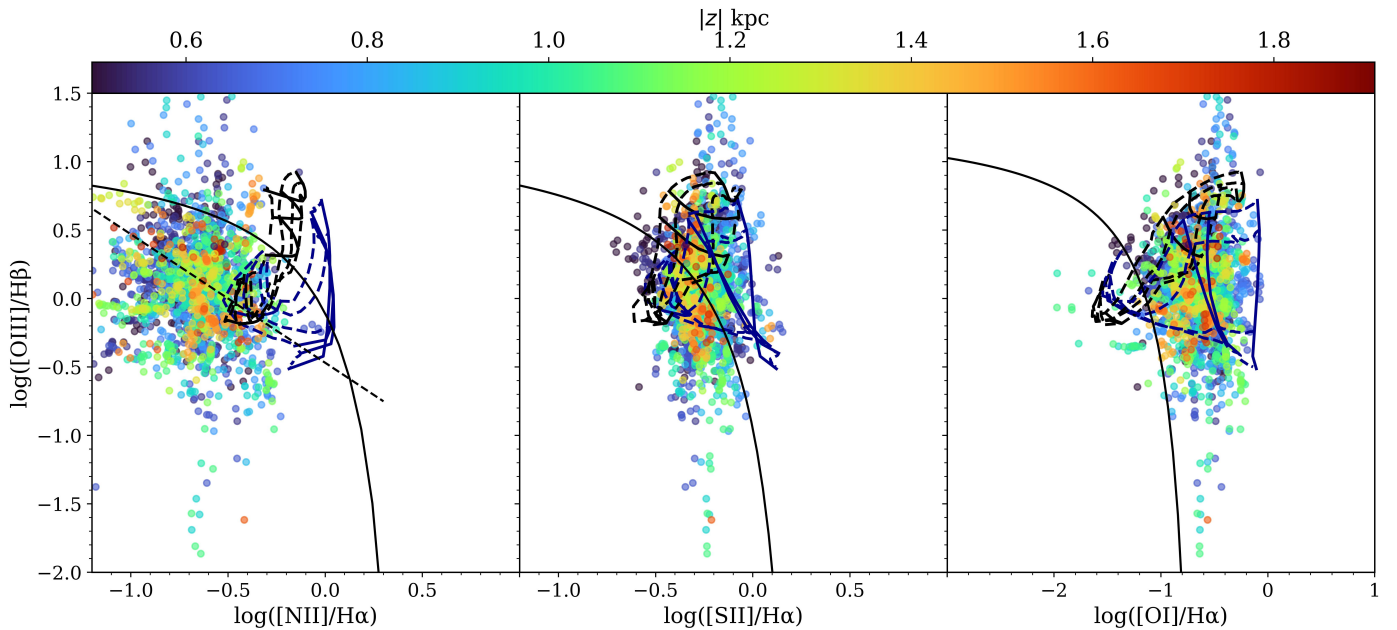


Fig. G.3: IC217 BPT with hybrid models, similar to Figure 7. 50% fast shocks and 50% star formation with $Z = Z_{\odot}$ and $q = 10^7$ cm/s.

Appendix H: IC1553

IC1553 is classified as an irregular galaxy (Vorontsov-Vel'Yaminov & Arkhipova 1968). Despite its inclination of 78.6° , the irregular morphology of the disk is evident due to the highly asymmetrical distribution of H II regions at $2 \text{ kpc} \lesssim \text{MAD} \lesssim 4 \text{ kpc}$ observed with respect the line of sight. For this reason, the differences in the ionisation conditions described in section 3 are more evident. The column of eDIG just above the H II regions exhibits a lower degree of ionisation for [N II] and [S II] compared to $H\alpha$ than in the column of eDIG where the emission from the H II regions is lower. In this latter scenario, the higher electron temperatures favour excitation due to collisions at a low-density regime (Osterbrock & Ferland 2006). This translates to a more collisionally-ionised eDIG compared to the column above the H II regions (with $f_{shock} = 0.4$ and 0.2 respectively). However, at $\text{MAD} \approx 0 \text{ kpc}$, the biconical structure observed in Figure 2 presents lower ionisation fraction ($S^+/S \approx 0.35$) than the rest of the eDIG, but with an increasing electron temperature in height, reaching the highest values ($\sim 9 \cdot 10^3 \text{ K}$) of all the eDIG. This is consistent with the presence of gas accretion in the galaxy found by Rautio et al. (2022) and Dirks et al. (2023).

The general behaviour of the [O III]/ $H\beta$ and [O I]/ $H\alpha$ ratios, as for [N II]/ $H\alpha$, [S II]/ $H\alpha$, is to increase with the height, also observed in previous studies (Rand 1998; Haffner et al. 2009b; Ho et al. 2016; Dirks et al. 2023). Nevertheless, in the BPT diagrams, there is no clear correlation between the location of the bins in the diagram and their distance with respect to the midplane. This lack of correlation is due to the two-dimensional dependence between the ionisation conditions and the galactic plane. For the [O I]/ $H\alpha$ ratios, the emission line map is similar to the [N II]/ $H\alpha$ and [S II]/ $H\alpha$ maps. As the [O I]/ $H\alpha$ ratio is related to the amount of H^0 relative to H^+ , lower values of this ratio in the DIG will imply a higher degree of ionisation of the neutral hydrogen (Rand 1998; Haffner et al. 2009b; BETIS I). As for the [N II]/ $H\alpha$ and [S II]/ $H\alpha$ ratios, this ratio is also lower

in the eDIG between $2 \text{ kpc} \lesssim \text{MAD} \lesssim 4 \text{ kpc}$ than between $-2 \text{ kpc} \lesssim \text{MAD} \lesssim 2 \text{ kpc}$.